Fortschritt-Berichte VDI

Reihe 9

Elektronik/Mikro-
und Nanotechnik

Dr.-Ing. Björn Jakob Müller,
Frankfurt am Main

Nr. 396

Improvement of $Cu(In,Ga)(S,Se)_2$ thin film Solar Cells with the help of Gallium and Sulfur Gradients

Acknowledgment

At this point I would like to thank everybody very much who has accompanied and supported me during my PhD time.

My special thanks goes to Prof. Dr. Herr and the company Robert Bosch GmbH for this very interesting topic. I have learned a lot about the section of solar cells, material science and semiconductor physics. I'm very grateful to Prof. Dr. Herr about his excellent support during my whole PhD time. In the seminar of the Institute of Micro- and Nanomaterials I was trained to give presentations and I additionally have learned a lot from the positive discussions during the seminar.

Additionally I would like to thank Prof. Dr. Walter for the friendly takeover of the second opinion of the thesis. Especially in the field of thin film solar cells, solar cell physics and SCAPS simulations he has given me a lot of valuable inputs.

On behalf of the Robert Bosch GmbH, I would like to thank my company supervisors Siggi and Veronika. Additionally I would like to thank my several direct and indirect superiors during this time Leonore Glanz, Carsten Herweg, Thomas Wagner, Mr. Schiller, Mr. Treutler and Mr. Rapp who have given me the best boundary conditions during the thesis. Furthermore I would like to thank all the colleagues from the departments of CR/ANA, CR/ARM, CR/ARC and CR/ARY. I also want to name the former colleagues from the BoschSolar CISTech GmbH, especially Frank Hergert, for the very helpful discussions about publication drafts and the progress of the thesis. For the proof-reading (language correction) I would like to thank Agnieszka as well as Emilia and Benjamin.

All my colleagues from the office and the lab (”Technikum”) supported me great and made the time enjoyable. Special thanks to Andreas, Anja, Armin, Arthur, Christiane, Dirk, Erhard, Frederik, Guido, Heiko, Helmut, Herbert, Huu Phuc, Ingo, Yvonne, Jochen, Julia, Juergen, Kathrin, Klaus, Lars, Lutz, Magret, Maira, Markus, Markus, Martin, Minh, Mr. Neidhardt, Mr. Schmidt, Mr. Schneider, Ms. Klose, Ney, Nicolas, Nils, Oliver, Patrick, Petra, Rainer, Sarah, Stefan, Stefan Stefan, Stephan, Silvan, Susanne, Thomas, Thomas, Tina, Ulrich, Valerie, Victoria, Ulrike, Uwe and Wladislaw (I hope that I have not forgotten anybody).

Thanks to the Bosch PhD program I had the possibility to learn more about the Bosch company and additionally I was able to spend some nice activities after the long working time.

The good discussions with the CIGS PhD team Christian, Rou Hua and Ulrich have helped a lot for the progress of the thesis and for the scientific as well as the private exchange.

Thanks for the support of my interns and master students Borirak, Bradley, Christian, Joel, Markus and Thomas in the lab, with evaluation topics and during the interpretation of data.

Many thanks to all of my friends in Gladenbach/Marburg, Gerlingen/Stuttgart and Tuebingen/Reutlingen who made the time beside the thesis so wonderful. At this point I want especially name Felix as a good friend who always had an open ear for me.

A lot thanks to my parents Sigrid and Ernst who have supported me during my whole school and study time. Furthermore they encouraged me again and again during the PhD time very often. My brother Alexander has supported me, especially in the hard times during the thesis for what I’m very thankful for. Thank you for being such good parents, a good brother and good friend.

Last but not least I would thank my girlfriend Ines Madeleine who has encouraged me during the stressful phase of the thesis.

Fortschritt-Berichte VDI

Reihe 9

Elektronik/Mikro- und Nanotechnik

Dr.-Ing. Björn Jakob Müller,
Frankfurt am Main

Nr. 396

Improvement of $Cu(In,Ga)(S,Se)_2$ thin film Solar Cells with the help of Gallium and Sulfur Gradients

Müller, Björn Jakob

Improvement of Cu(In,Ga)(S,Se)$_2$ thin film Solar Cells with the help of Gallium and Sulfur Gradients

Fortschr.-Ber. VDI Reihe 09 Nr. 396. Düsseldorf: VDI Verlag 2018.
202 Seiten, 101 Bilder, 22 Tabellen.
ISBN 978-3-18-339609-2, ISSN 0178-9422, € 71,00/VDI-Mitgliederpreis € 63,90.

Für die Dokumentation: Solarzelle, Dünnschichtsysteme, Phasenumwandlungen, step elemental layer Prozess, Gradient, Diffusion, Diffusionsbarriere, Chalkopyrite, Cu(In,Ga)(S,Se)$_2$, in-situ Analyse

Das Ziel der Arbeit besteht darin, optimierte Absorber für das Dünnschicht Solarzellensystem Cu(In,Ga)(S,Se)$_2$ mit Hilfe von industrienahen Prozessen herzustellen. Der industrienahe zweistufige Herstellungsprozess beinhaltet das Aufbringen von metallischen Vorläuferschichten (Kathoden zerstäubung & thermische Verdampfung) und die Bildung des Chalkopyrit Absorbers in Folge des thermischen Ausheizschrittes. Der gezielte Einbau von Konzentrationsgradienten bestehend aus Ga/In und Se/S wird werkstoffseitig am Absorber strukturell analysiert und für die elektronischen Eigenschaften der Solarzelle optimiert. Zur Justage des Ga/In Profils werden sowohl das optimierte Temperaturprofil als auch ein Überangebot an Chalkogenen verwendet. Für die Einstellung des Se/S Profils im Chalkopyrit dienen das Ausgangsverhältnis sowie ein nachträglicher S Einbau (Erweiterung auf einen drei-stufigen Prozess). Um den Rückkontakt der Solarzelle vor den aggressiven Chalkogenen während des Prozesses zu schützen, wurde eine Mo-N Diffusionsbarriere entwickelt.

Bibliographische Information der Deutschen Bibliothek
Die Deutsche Bibliothek verzeichnet diese Publikation in der Deutschen Nationalbibliographie; detaillierte bibliographische Daten sind im Internet unter www.dnb.de abrufbar.

Bibliographic information published by the Deutsche Bibliothek
(German National Library)
The Deutsche Bibliothek lists this publication in the Deutsche Nationalbibliographie (German National Bibliography); detailed bibliographic data is available via Internet at www.dnb.de.

Als Manuskript gedruckt. Printed in Germany.

ISSN 0178-9422

ISBN 978-3-18-339609-2

Inscription

To my parents
and to my brother.

Contents

Nomenclature

The following abbreviations, symbols and codes are used in the thesis:

a:	Lattice constant
$a(E)$**:**	Absorptance
Ag:	Silver
Al:	Aluminium
α**:**	Absorption coefficient
α_{eff}**:**	Effective absorption coefficient
AZO:	Al:ZnO
BSF:	Back surface field
β**:**	Linear E_g grading degree
c:	Concentration
c_L**:**	Speed of light
CB:	Conduction band
CBD:	Chemical bath deposition
CE:	Co-evaporation
CGI:	Cu/(Ga+In) concentration ratio
$CuGaS_2$:	Copper Gallium Disulfide
$CuGaSe_2$:	Copper Gallium Diselenide
χ**:**	Electron affinity
$Cu(In,Ga)Se_2$:	Copper Indium Gallium Diselenide
$Cu(In,Ga)(S,Se)_2$:	Copper Indium Gallium Disulfo Selenide
$CuInS_2$:	Copper Indium Disulfide
$CuInSe_2$:	Copper Indium Diselenide
Cu:	Copper
d_1**:**	Back grading distance
d_2**:**	Front grading distance

D**:**	Diffusion coefficient of a diluted system
d_c**:**	Critical distance
DC:	Direct current
Di:	Diode
d_{hkl}**:**	Lattice spacing distance
D_n**:**	Carrier diffusion coefficient
DOS:	Density of states
ξ**:**	Electric field
ξ_{grad}**:**	Electric field in graded absorber
$\mathbf{e^-}$**:**	Electron
EDX:	Energy dispersive X-ray spectroscopy
E_F**:**	Fermi energy
E_g**:**	Band gap
E_n**:**	One electron energy
EMPA:	Swiss Federal Laboratories for Materials Science and Technology
EQE:	External quantum efficiency
η**:**	Efficiency
Fe:	Iron
FF:	Fill factor
FWHM:	Full width at half maximum
g:	Carrier generation rate
G:	Generation current
Ga:	Gallium
GDOES:	Glow discharge optical emission spectrometry
GIXRD:	Grazing incidence X-ray diffraction
GGI:	Ga/(Ga+In) concentration ratio
G_h**:**	Hole generation current
G_n**:**	Electron generation current
$\mathbf{h^+}$**:**	Hole
$\hat{H}^{1e}_{eff}$**:**	Effective one electron Hamiltonian
HTG:	High temperature glass
$h\nu$**:**	Photon energy
$\hbar\Omega$**:**	Phonon energy
I:	Intensity
IF:	Interface recombination
I_{mp}**:**	Current at maximum power point
In:	Indium
IQE:	Internal quantum efficiency

I-V:	Current-voltage
IXRD:	In-situ X-ray diffraction
i-ZnO:	Intrinsic ZnO
J:	Current density
J_0:	Reverse saturation current density
J_{bb}:	Photo current density, produced by black body radiation
JCPDS:	Joint Committee on Powder Diffraction Standards
J_{dark}:	Dark current density
J_{atom}:	Material flux
J_{ph}:	Photo current density, occurs according to absorbed photons
J_{rec}:	Recombination current density
J_{sc}:	Short-circuit current density
J_{sc}^{grad}:	Short-circuit current density calculated by analytical approach
J_{sc}^{SCAPS}:	Short-circuit current density calculated by SCAPS simulations

J_{tot}:	Total current density
K:	Pottasium
k_B:	Boltzmann constant
k_e:	Extinction coefficient
$\vec{k}$:	Scattering vector
L_α:	Absorption length
L_n:	Electron diffusion length
L_p:	Hole diffusion length
M:	Diffusion coefficient
mc-Si:	Multicrystalline silicon
MoN:	Molybdenum nitride
MoS$_2$:	Molybdenum disulfide
MoSe$_2$:	Molybdenum diselenide
MoSSe$_2$:	Molybdenum disulfoselenide
$\overline{n}$:	Complex refractive index
n_r:	Refractive index
Na:	Sodium
N_A:	Acceptor density
∇:	Gradient
N_C:	DOS in the CB
N_D:	Donor density
n_{id}:	Diode ideality factor
NREL:	National Renewable Energy Laboratory

N_V:	DOS in the VB
n-ZnO:	n-doped ZnO
Δn:	Excess charge carrier density (electrons)
ODC:	Ordered defect compound
PL:	Photoluminescence
P_{mp}:	Maximum electrical power
P_{opt}:	Power of incoming photons
Ψ:	Electrostatic potential
p-Si:	Polycrystalline silicon
PV:	Photovoltaics
ϕ_{sun}:	Photon flux from the sun
$\phi(V,E)$:	Emitted photon flux, depending on voltage and energy
Δp:	Excess charge carrier density (holes)
Q:	Material quantity
QNR:	Quasi neutral region
R:	Recombination current
ρ:	Charge distribution
R_h:	Hole recombination rate
R_n:	Electron recombination rate
R_p:	Parallel resistance
R_s:	Series resistance
RTP:	Rapid thermal processing
S/metal:	S/(Cu+Ga+In) concentration ratio
S:	Sulfur
SCAPS:	Solar Cell Capacitance Simulator
SCR:	Space charge region
Se/metal:	Se/(Cu+Ga+In) concentration ratio
Se:	Selenium
SEL:	Stacked elemental layer
SEM:	Scanning electron microscopy
SFG:	Standard float glass
SIMS:	Secondary ion mass spectroscopy
SQ:	Shockley-Queisser
SRH:	Shockley-Read-Hall
SSSe:	S/(S+Se) concentration ratio
T:	Temperature
Te:	Tellurium
T_S:	Sulfurization temperature

T_{Se}:	Selenization temperature
μ_n:	Electron mobility
μ_p:	Hole mobility
VB:	Valence band
V_D:	Built-in potential
v_e:	Recombination velocity for electrons
V_{eff}:	Effective potential
v_h:	Recombination velocity for holes
V_{mp}:	Voltage at maximum power point
V_{oc}:	Open-circuit voltage
ϕ_n:	One electron wave function
W_p:	Watt peak
XRD:	X-ray diffraction
XRF:	X-ray fluorescence
Zn:	Zinc
ZnS:	Zinc blende
ZSW:	Centre for Solar Energy and Hydrogen Research Baden-Wuerttemberg

Abstract

The aim of this work is to optimize the absorber for $Cu(In,Ga)(S,Se)_2$ thin film photovoltaic cells in order to get a higher efficiency of the energy conversion in the framework of a well-established industrial process. In general the industrial process belongs to the family of two-step processes which consist of sputtering and evaporating a stack of elemental layers and subsequent annealing in order to form the chalcopyrite structure of the absorber. The two-step process stays in competition with the more flexible co-evaporation process, which up to now has delivered the best laboratory cells reaching efficiencies up to 22.6%. The motivation for the two-step process may also be derived from the achievement of the best module conversion efficiencies of almost 18%. The Shockley-Queisser limit of single junction solar cells is around 33%. The difference of 11% to the best laboratory cells can be explained by optical reflection and internal recombination losses (Auger and Shockley-Read-Hall) and is mostly reflected in open-circuit voltage losses. In order to achieve higher open-circuit voltages, conduction band V-profiles are introduced in order to reduce space-charge region and interface (buffer) recombination as well as back contact recombination. Band gap grading is most easily achieved in the co-evaporation process. Due to the fact that the stacked elemental layer process is driven by interdiffusion of elements and compounds the precise control of these V-profiles is a challenge and alternative ways to control the band gap profile need to be found. To adapt the electronic band structure to the back electrode and the transparent window via a buffer layer, a certain gradient of Ga and S in the absorber is needed. In this work,

optimized temperature profiles, optimal chalcogen amounts and a modified back contact have been identified as possible parameters for improvement of solar cell performance. In the field of band gap grading in $Cu(In,Ga)Se_2$ thin films a method was found to control the Ga/(Ga+In) profiles by the process temperature and the Se amount. This allows to optimize band gap profiles in the p-n junction solar cell with respect to more efficient charge carrier collection. With the help of numerical SCAPS simulations the optimized parameters of back and front surface grading properties can be calculated for the application in optimal process conditions. For the adjustment of S/(S+Se) profiles in $Cu(In,Ga)(S,Se)_2$ thin films, defined concentration gradients were established by applying chalcogens with a specific ratio before the annealing process. The conventional two-step process was furthermore modified by separating the annealing step into a pure selenization and a sulfurization phase in order to better adjust the S/(S+Se) profile. A large parameter field makes a detailed study of post sulfur diffusion processes possible. However, to adjust the chalcogen profile in the thin film it was found that the most important parameters are the sulfurization temperature and the sulfurization time in step two. Furthermore, a Mo-N layer was introduced as a novel barrier layer against chalcogen diffusion to the Mo back contact. A self-limited $MoSe_2$ layer growth on top of the Mo-N barrier layer with a defined thickness has been found, which does not hinder charge carrier collection at the back contact and additionally ensures a quasi-ohmic contact.

CHAPTER 1

Introduction

The worldwide demand for energy in the coming decade will increase due to the developing countries, economical development and population growth. Therefore there is a need for alternative energy sources, besides the limited amount of fossil energy sources, like photovoltaics with a nearly unlimited source (sun). The process which converts sunlight into electricity is based on the photovoltaic effect, which was first described by Becquerel in 1839 [1–4]. Photovoltaic (PV) technologies can be divided into three different fields which are wafer-based silicon, thin-film technologies and new PV concepts/applications like organic solar cells [5]. Up to now single crystal (c-Si) and multi-crystalline silicon (mc-Si) have dominated the market by approximately 90% and the rest has been covered by the thin film solar cells like amorphous Si (a-Si), $Cu(In,Ga)(S,Se)_2$ (CIGSSe), CdTe/CdS or polycrystalline Si (p-Si) [2, 5, 6]. Organic and nanostructured solar cells stand for the new PV concepts, which until now have not appeared in the production market [5].

1.1 Motivation

In terms of cost per performance, thin film technologies are considered to be a very good alternative to standard Si solar cells. A cost reduction of approximately 30% is possible [5]. The ratio of cell cost vs. the power at maximum power point ($\$/W_p$) is used to compare the different PV technologies. The Bosch research activities in the field of PV identify efficiency (η) and size of production line as the major cost influencing parameters. A lot of research focuses on how to transfer the laboratory cell efficiencies into production. Historically the chalcopyrite thin films started with the ternary $CuInSe_2$ (CISe) compound, which has later been extended by Ga to form a quaternary alloy $Cu(In,Ga)Se_2$ (CIGSe), thereby improving the band gap (E_g) matching to the solar spectrum. In the stacked elemental layer (SEL) process Ga agglomerates at the back contact and therefore a good E_g match is only possible with additional near-surface S incorporation, which leads to CIGSSe. Due to the fact that CIGSSe has a high absorption coefficient (α), only 2 μm thick layers are needed for absorption of the incident sun light, which reduces the material consumption. The technologies which are needed to produce CIGSSe on a large scale include standard sputtering and evaporation techniques enabling an easy scale-up to large areas. Additionally, the η record explosion towards 22.6% [7] in the year 2014-2016 [8], mainly driven by the Centre for Solar Energy and Hydrogen Research Baden-Wuerttemberg (ZSW), Swiss Federal Laboratories for Materials Science and Technology (EMPA) and Solar Frontier still shows room for improvement in the material system and makes the predicted practical limit of 28% [9] appear to be within reach. The material system CIGSSe consists of the group I element Cu, group III elements Ga/In and the group VI elements S/Se. An appropriate mixture of these elements forms an ideal chalcopyrite absorber, which is the basic element of the CIGSSe solar cell. According to the Shockley-Queisser (SQ) limit for p-n junction solar cells the band gap energy E_g is a main factor determining the solar cell efficiency [10]. It is possible to improve the charge carrier collection efficiency by controlling the E_g profile of the absorber in changing the profiles of the Ga/(Ga+In) (GGI) or S/(S+Se) (SSSe) ratios along the depth of the cell.

1.2 Outline of the thesis

This dissertation is structured into five chapters and starts with the description of CIGSSe physical properties and their concentration dependence (see chapter 2). The relevant phase diagram and the fundamental SEL process are shortly introduced. Furthermore, CIGSSe device physics and analytical treatments based on the Shockley-Queisser (SQ) model without or with concentration gradients are introduced, and device modeling with the help of 1D numerical Solar Cell Capacitance Simulator (SCAPS) are explained. In chapter 3, experimental procedures used in deposition and characterization of thin films and complete solar cells are introduced. The SEL process is discussed in more detail here, since improvement of the process is the main goal of this thesis. The most important characterization techniques like Raman scattering, photoluminescence spectroscopy (PL), X-ray diffraction (XRD), and scanning electron microscopy (SEM) are shortly introduced, as well as current-voltage (I-V) and quantum efficiency (QE) measurements. In chapter 4 an intensive analysis of CIGSe phase formation is presented using ex- and in-situ characterization techniques. A functional layer, based on Mo-N, is introduced as a chalcogen diffusion barrier at the back contact in order to prevent back contact corrosion. The Ga profile in the absorber can be indirectly modified in a systematic way either by variation of the Se amount or by variation of the temperature profile during the annealing procedure, which provides new ways to approach the desired E_g profile. The S profile can be controlled by a newly introduced three step process which includes a S post-treatment. The resulting films are analyzed by in-situ analysis to better understand the underlying diffusion processes. At the end of each part small summaries are given. A general summary and discussion (see chapter 5) concludes the thesis and possible directions for future work in the field of graded E_g CIGSSe solar cells are proposed. Parts of the thesis have already been published in the following journal articles [11–15]. Additionally, the original document of the PhD thesis has already been published online at the server of the University of Ulm [16]. In the current document (for the VDI as publisher) the acknowledgment and the sequence of the introducing chapters have been slightly modified.

CHAPTER 2

Fundamentals of chalcopyrite solar cell devices

This chapter introduces the fundamentals of CIGSSe thin films and solar cells. Material-specific topics like crystal and band structure, phase formation and solar cell properties are discussed. Additionally, a short introduction into diffusion processes in solid states and CIGSSe thin films is presented.

2.1 Basic material properties

The basic element of the thin film solar cell is the CIGSSe absorber [17,18]. CIGSSe solar cells belong to the family of hetero structure (p-n junction of different materials) solar cells [19] based on polycrystalline thin films [2,17,18,20–23]. A pentanary material system like CIGSSe has some challenging material science aspects, which have to be controlled for achieving highest material quality. In the following the principles of alloying, formation of secondary phases and the correlation of Ga/(Ga+In) and S/(S+Se) ratios with band structure will be presented.

2.1.1 Crystal and band structure of chalcopyrites

In general, a crystal consists of equal atom groups which are arranged in well-ordered periodic structures. The smallest repeating structure in a crystal is called a unit cell which has the dimension of a lattice constant a in the case of cubic systems [17,24,25]. Many important optoelectronic semiconductors have a zincblende (ZnS) lattice structure [26]. A modification of the ZnS structure at the anion and cation sublattice sites leads to the structure of CIGSe and related compounds of the $A^{I}B^{III}C_2^{VI}$ semiconductor group [(Cu,Ag)(In,Ga,Al,Fe)(S,Se,Te)$_2$] crystallizing in a tetragonal chalcopyrite structure (see figure 2.1 (a)) [18,27]. In this case the cation lattice of II-VI materials like ZnS (cation=Zn) is alternatively replaced by Cu and In atoms. Every anion (Se) is tetrahedrally surrounded by four cations (Cu and In), and every cation is surrounded by four anions [17]. These tetrahedra can be described by clusters of $A_n^{I}B_{4-n}^{III}$(n=1-4), which are arranged around a C^{VI} or (S,Se) atom. The variation of the I-VI and III-VI bond strength due to chemical differences is reflected in the tetragonal distortion factor c/2a and the anion displacement parameter [18,23]. One important crystal orientation in the CIGSSe system is the [112] direction [28,29]. Either cations or anions are located in these (112) planes [30,31].

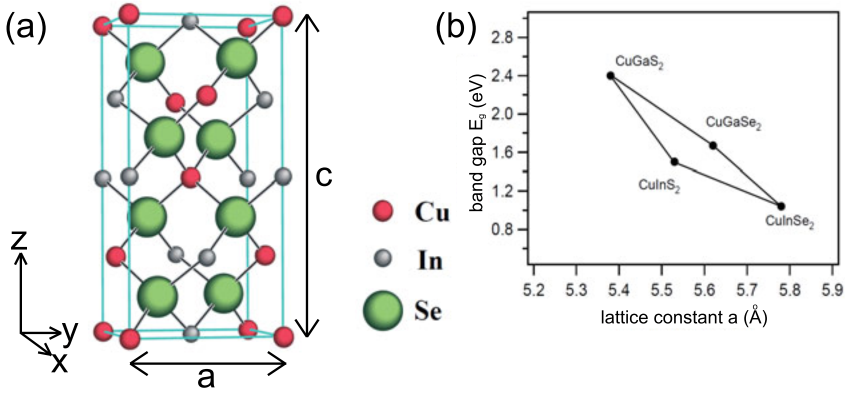

Figure 2.1: (a): The crystal structure of the ternary CISe is the basis of all chalcopyrites (reproduced from [32] with permission of the Institute of Surface Science at the TU Darmstadt). The cation sublattice is filled with Cu and In and the anion sublattice with Se. (b): The band gap E_g is shown as a function of the lattice constant a of CIGSSe by alloying either S on the anion or Ga on the cation sublattice (reproduced from [32] with permission of the Institute of Surface Science at the TU Darmstadt).

The optoelectronic properties of a semiconductor material can be understood best by the concept of energy bands [24]. In general, electrons

(e^-) have discrete energy levels in atoms according to Bohr's model and quantum mechanics. In a solid state many atoms are arranged together, which leads to overlapping wave functions of the allowed e^- states, which in consequence results in the formation of the energy bands. In order to describe the e^- in a solid state a complex Hamilton operator is introduced. The Hamilton considers the kinetic energy of the e^-s, the kinetic energy of the nuclei, the nucleus-nucleus interactions as well as the e^--e^- interactions and the interaction between nuclei and e^- [26]. The system is furthermore simplified in order to categorize all e^- into valence e^- and core e^-. The core e^- together with the nuclei form the ionic cores. With the help of the Born-Oppenheimer approximation the system is decoupled and the e^-s can be described independently, under the approximation that the ionic cores stay in their equilibrium position. The many body problem is simplified into the one e^- or mean-field approximation, where all e^- feel the same effective potential $V_{eff}(\vec{r})$, which is caused by the other e^- [26]. Now it is possible to solve the many body problem in solid states approximately by just solving the one e^- Schrödinger equation (see equation 2.1) for the effective one e^- Hamilton $\hat{H}^{1e}_{eff}$, one e^- wave functions $\phi_n(\vec{r})$ and one e^- energies E_n.

$$\hat{H}^{1e}_{eff}\phi_n(\vec{r}) = \left(\frac{p^2}{2m} + V_{eff}(\vec{r})\right)\phi_n(\vec{r}) = E_n\phi_n(\vec{r}) \tag{2.1}$$

$V_{eff}(\vec{r})$ has to fulfill the lattice periodicity and, according to the Bloch-Theorem, the solutions for the wave functions are Bloch functions [24], which are expressed by the product of plane waves with a lattice periodic function [26]. As a result the energy states of semiconductors are separated into valence band (VB), conduction band (CB) and a forbidden zone, the band gap with a width E_g, in between. Semiconductors are categorized into direct and indirect band gap semiconductors, which refers to the optoelectronic process of creating e^--hole (h^+) pairs by absorption of photons ($h\nu$) and vice versa. In the band diagram the absorption and emission processes are described in the energy vs. momentum plot where e^-, h^+, photons ($h\nu$), phonons ($\hbar\Omega$) and their interactions are visualized. In the case of direct semiconductors the CB minimum is located above the VB maximum in an $E(k)$ diagram, where k is the e^- wave vector. For indirect semiconductors, the CB minimum lies at a different k value than the VB maximum (see figure 2.2). For optical absorption indirect semiconductors need an exchange phonon ($\hbar\Omega$) in order to create e^-/h^+ pairs.

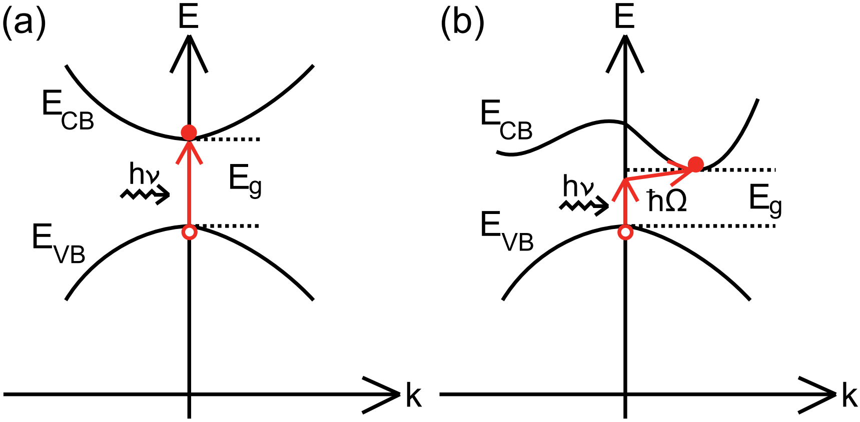

Figure 2.2: Schematic band diagram of direct and indirect semiconductors schematically showing the process of optical absorption. The CB minimum is directly above the VB maximum for direct semiconductors in (a) whereas the CB minimum is placed at another wave vector k for indirect semiconductors in (b). An exchange phonon ($\hbar\Omega$) is needed in the absorption process for indirect semiconductors.

The macroscopic processes of absorption, emission and conductance in semiconductor systems have to be described on a microscopic level with the occupation of e^- energy states [26]. Intrinsic conduction in semiconductors can be understood as the excitation of an e^- from the VB to the CB with the simultaneous creation of a h^+ in the VB. The e^--phonon-interaction is responsible for the macroscopic phenomenon of the electric resistivity [33]. CIGSSe is a direct semiconductor with a very high coefficient of optical absorption (representative $\alpha(\lambda)$ are given later in figure 2.5 (b)) around 10^5 cm^{-1} [17] and therefore almost all incident photons are absorbed within the absorption length $L_\alpha = \frac{1}{\alpha} \leq 1$ μm [30]. In the alloys CIGSe and CuIn(S,Se)$_2$ (CISSe) In and Se atoms are partly substituted by Ga and S atoms which improves the optoelectronic properties. The lattice parameter

a of CISe is reduced due to the smaller covalent radius of Ga and S, which causes an increase in E_g of the system CIGSSe [30]. The E_g varies (see figure 2.1 (b)) with material composition in the range from 1.04 eV (CISe) to 2.4 eV (CGS) [34, 35], which allows for an optimized match to the solar spectrum.

2.1.2 Ternary chalcopyrites

With the help of the Gibbs triangle, the alloy formation for the different elements A^{I} (Cu), B^{II} (In) and C^{VI} (Se) can be described. The phase triangle is intersected by different composition-temperature planes, which are defined by fixed composition ratios $A^{I}_{2}C^{VI}$ to $B^{III}_{2}C^{VI}_{3}$ and $A^{I}C^{VI}$ to $B^{III}C^{VI}$ for example (see figure 2.3 (a)). Using composition-temperature plane (quasi binary tie line) between the two binary selenides Cu_2Se and In_2Se_3 (see figure 2.3 (b)), the phase formation as a function of Cu contents is exemplified [18, 22, 23]. The intermediate phases are the α-phase (CISe), β-phase ($CuIn_3Se_5$), δ-phase (high temperature phase) and Cu_2Se (metallic phase). The existence range for the α-phase, which is the desired one, is located at a Cu amount between 24 and 24.5 at.% (see figure 2.3 (b)). At the growth temperature used in most of processes (approximately 550 °C) this composition leads to a single phase material. However, during cooling down to room temperature it tends to undergo phase separation [28]. The replacement of In by Ga, and additional Na doping, widens the existence range of the α-phase [17, 22, 23]. For the quaternary CIGSe or pentanary CIGSSe the phase diagram is not fully known due to its complexity, which makes it necessary to reduce the problem of the Gibbs triangle to CISe and the simplified quasi binary tie line. Some of the basic ideas introduced for the ternary compound will also be used for further discussion of the graded quaternary CIGSe (see chapter 4.1) and pentanary CIGSSe (see chapter 4.2).

2.1.3 Diffusion processes in thin film systems

The SEL process (in detail see chapter 3) consists of an annealing procedure, where the diffusion of atoms plays an important role for the crystal

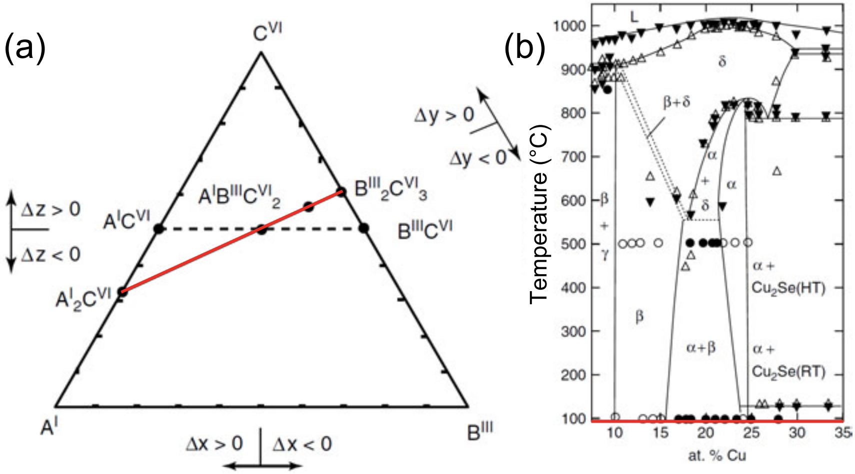

Figure 2.3: (a): Thermodynamic Gibbs triangle for the phase formation in the ternary system Cu-In-Se. In red the quasi binary tie line for $A_2^IC^{VI}$-$B_2^{III}C_3^{VI}$ is highlighted (reproduced from [18] with permission of WILEY-VCH Publishing). (b): The quasi-binary phase diagram of Cu-In-Se for Cu_2Se and In_2Se_3. The most important phases formed during the Cu-In-Se (reproduced from [36–38] with permission of Carl Hanser Verlag GmbH) are indicated by α, β, γ and δ.

formation. In general, the process of diffusion or atomic migration is described by the transport laws. In terms of thermodynamics it is always a non-equilibrium, irreversible process [39]. The presence of a gradient in the chemical potential $\frac{\partial \mu}{\partial x}$ leads to a particle flux J'_{atom} with its direction down the gradient, which is summarized in Fick's first law (without any external forces, see equations 2.2 and 2.4). In the case of diluted systems (e.g. solutions) the concentration gradient $\frac{\partial c}{\partial x}$ is used to describe the J_{atom} (see equations 2.3 and 2.5). Here, D or $\underline{D}$ represents the constant diffusion coefficient of a diluted system (otherwise M or $\underline{M}$). The approximation of a diluted system is also used in the thesis for simplicity's sake to describe the diffusion processes.

$$\text{in 1D: } J'_{atom} = -M\frac{\partial \mu}{\partial x} \tag{2.2}$$

$$\text{in 1D, diluted: } J_{atom} = -D\frac{\partial c}{\partial x} \tag{2.3}$$

$$\text{in 3D: } \mathcal{J}'_{atom} = -\underline{M}\nabla\mu \tag{2.4}$$

$$\text{in 3D, diluted: } \mathcal{J}_{atom} = -\underline{D}\nabla c \tag{2.5}$$

In some systems also an additional force can disturb the free diffusion of particles leading to a drift flux or mass flow $< v > c$ with an average velocity $< v >$ resulting in a more general equation of Fick's first law (with external forces, see equation 2.6) [40]. In the following, the focus will lie on planar diffusion fronts, which can be discussed in 1D (important for chapter 4.2.3).

$$J_{atom} = \underbrace{-D\frac{\partial c}{\partial x}}_{diffusion\ flux} + \underbrace{< v > c}_{drift\ flux/mass\ flow} \tag{2.6}$$

The steady-state regime is just relevant for a limited amount of systems (e.g. permeation of gas through a foil). In general diffusion is time dependent [39]. The combination of Fick's first law with continuity equation is needed, leading to Fick's second equation (see equation 2.7) [40]. Here, the drift term is not considered, and the solution is a time dependent concentration or depth profile $c(x,t)$.

$$\underbrace{\frac{\partial J_{atom}}{\partial x} = -\frac{\partial c}{\partial t'}}_{continuity\ equation} \underbrace{\rightarrow}_{Fick's\ first\ law} \frac{\partial c}{\partial t} = D\frac{\partial^2 c}{\partial x^2} \quad in\ 1D \tag{2.7}$$

Interdiffusion in thin films deposited on bulk material is described by sandwich or surface geometry [39]. The initial condition for the concentration is set as $c(x,t = 0) = Q\delta(x)$, with Q being the amount of deposited material and the Dirac delta function. For all times t, one can find the concentration by integrating over the variables from 0 to $+\infty$ (surface) and $-\infty$ to $+\infty$ (sandwich) respectively [39], which results in a Gaussian curve (see equation 2.8 and 2.9). In this description $\frac{x}{2\sqrt{Dt}}$ is the width and $\overline{x} = \sqrt{2Dt}$ the mean penetration depth into the thin film. D can be determined by plotting $\ln(c)$ vs. x^2 and extracting D out of the slope.

$$\int\limits_{0}^{+\infty} c dx = Q \rightarrow c(x{,}t) = \frac{Q}{2\sqrt{\pi Dt}} \exp\left(-\frac{x^2}{4Dt}\right) \tag{2.8}$$

$$\int\limits_{-\infty}^{+\infty} c dx = Q \rightarrow c(x{,}t) = \frac{Q}{\sqrt{\pi Dt}} \exp\left(-\frac{x^2}{4Dt}\right) \tag{2.9}$$

In the field of CIGSe thin film formation the interdiffusion of Ga into CISe or In into CGSe is relevant (see chapters 4.1.2 and 4.1.4). Due to the fact that the system is based on the interdiffusion of Ga into CISe and In into CGSe the estimated D values are mean values of D_{CISe}^{Ga} and D_{CGSe}^{In}, respectively. In equation 2.10 the concentration profile $c(x{,}t)$ (here: used for the Ga/(Ga+In) ratio) can be determined by using the complementary Gaussian error function $1 - erf\left[\frac{x}{2\sqrt{Dt}}\right] = erfc\left[\frac{x}{2\sqrt{Dt}}\right]$. In the case of CIGSSe thin films the diffusion of S into CIGSe is relevant (see chapter 4.2.3).

$$\frac{c(x{,}t) - c_1}{c_2 - c_1} = \frac{1}{2} erfc\left[\frac{x}{2\sqrt{Dt}}\right] \rightarrow c(x{,}t) = (c_2 - c_1) \cdot \frac{1}{2} erfc\left[\frac{x}{2\sqrt{Dt}}\right] + c_1 \tag{2.10}$$

In equation 2.10, c_2 and c_1 are the maximum and minimum concentration respectively in the diffusion area. In the initial state the shape of $c(x{,}t = 0)$ looks like a step function at the origin $x = 0$ ($c = c_1$ for $x < 0$ and $c = c_2$ for $x > 0$) and for $t > 0$ the curve becomes smeared out (see figure 2.4). For simplicity's sake, the values of $erfc[x]$ are taken from [39], where the output is calculated for $0 < x < 5$.

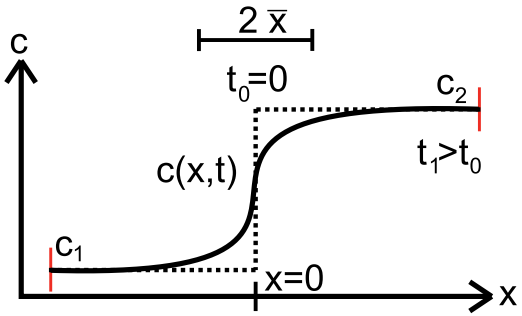

Figure 2.4: Schematic concentration profile of interdiffusion in a thin film with two regions of concentrations c_1 and c_2, respectively. A planar diffusion process starts after $t = t_1 > t_0 = 0$, which modifies the concentration profile from a step function towards a smeared out profile with a transition width $2\overline{x}$, $\overline{x} = 2\sqrt{Dt}$.

2.2 Chalcopyrite solar cell properties

In the following subchapter the fundamental physics of single junction solar cells are introduced by means of the diode law. To estimate the maximal possible η the SQ limit is used in the radiative recombination limit in order to figure out the dependency on the E_g. The basic concepts of E_g gradings are shown as a way to improve the optoelectronic properties. An analytical as well as a semi-numerical approach is used to simulate the performance parameters for different linear graded absorbers.

2.2.1 Physics of single junction solar cells

Solar cells convert the energy of incoming photons to create $\mathrm{e}^-/\mathrm{h}^+$ pairs. A solar cell in an ordinary setup consists of four basic parts like the substrate, the back contact, the absorber and the front contact (see figure 2.5 (a)). The substrate serves as a morphological smooth and clean surface for the latter solar cell device (from an industrial perspective, an important requirement for the substrate is low price). The major function of the front and back contact is the efficient charge carrier collection. The absorber is the centerpiece of the device because it is responsible for the process of photon absorption (see figure 2.5 (b)). The efficient separation of charge carriers occur at the p-n (hetero)junction. The SQ model assumes that all photons with the energy E_{ph} greater than the E_g of the absorber material are absorbed [10]. The excess energy $(E_{ph} - E_g)$ is dissipated by phonons and will heat the material. Another important issue in solar cell physics is the problem how to prevent $\mathrm{e}^-/\mathrm{h}^+$ pairs to recombine [24]. This task is fulfilled by the internal electric field generated by the p-n heterojunction [41]. The current transport across a p-n junction is described by drift and diffusion currents, which counterbalance each other in thermal equilibrium [24,41,42]. The drift current at the contact area of the p and n semiconductor originates from the electric field in the space charge region (SCR) of the junction, while the diffusion current is driven by the concentration gradient of charge carriers across the junction [41]. Furthermore, the diffusion current is influenced by the size of the built-in potential (V_D). In CIGSSe solar cells the p-n heterojunction consists of the p-doped CIGSSe absorber and the n-doped window layer. With the help of the Shockley equation [24, 41] for an ideal diode one can describe the I-V characteristics of the solar cell in the dark [42] (see equation 2.11). The junction properties are mainly described by the material dependent saturation current density (J_0), whose relation to the minority currents is shown in equation 2.12.

$$J(V) = J_0 \left[\exp\left(\frac{qV}{n_{id} k_B T} \right) - 1 \right] \tag{2.11}$$

$$J_0 = \left(\frac{qD_p}{L_p} p_n + \frac{qD_n}{L_n} n_p \right) = (J_n^{drift} + J_p^{drift}) \tag{2.12}$$

The minority carrier concentrations are p_n (h^+ in n region) and n_p (e^- in p region), the diffusivities D_n and D_p and the diffusion length $L_x = \frac{1}{\sqrt{D_x t_x}}$ where t_x displays the minority carrier lifetime ($x = n$,p) [24]. The diode ideality factor n_{id} defines the recombination mechanism dominating the photovoltaic device and q is the elementary charge. $n_{id} = 1$ stands either for an ideal SQ case with only radiative recombinations or it also identifies that recombination processes can only occur in the quasi neutral region (QNR). QNR describes the region of the p-n junction (at the edges) with the constraint of a vanishing electric field and therefore the minority charge carriers only move by diffusion. The value $n_{id}=2$ signifies that the recombination process within the SCR dominates [17].

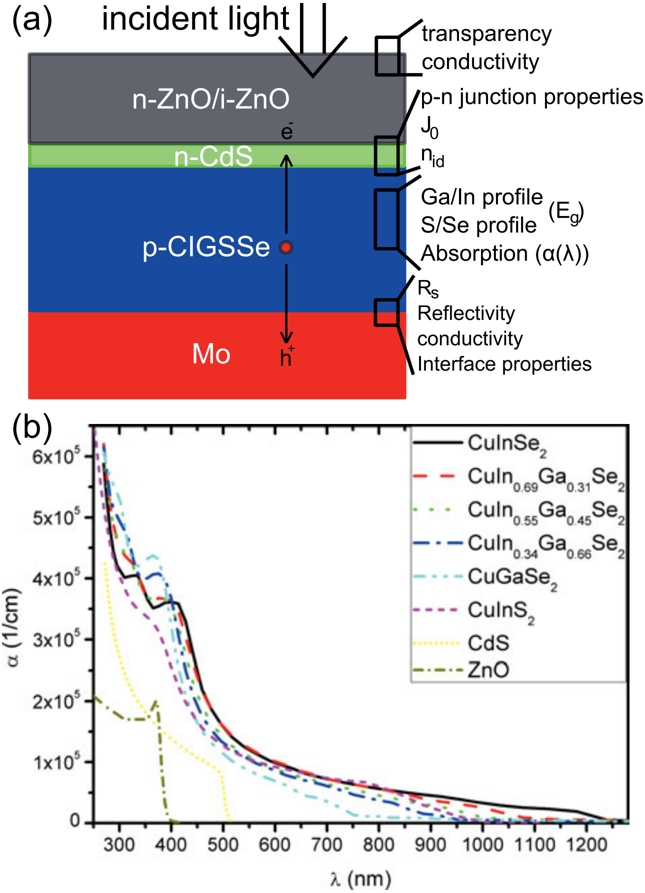

Figure 2.5: (a): Schematic overview of a CIGSSe thin film solar cell consisting of a Mo back contact, a p-CIGSSe absorber layer, a n-CdS buffer layer and a ZnO window. The incident photons are absorbed in CIGSe and e^-/h^+ pairs are generated due to the electric field induced by the p-n heterojunction. Afterwards the charge carriers are collected by the front and back contact. (b): Corresponding absorption profiles of the CIGSSe thin film solar cell materials with different CIGSSe E_gs related to varying Ga/In and S/Se ratios. Additionally the absorption profiles of CdS and ZnO is included.

It is a well known fact about solar cells that the total current strongly depends on the minority current densities J_n^{drift} and J_p^{drift} [42]. Under illumination, excess minority charge carriers are generated, which creates a non-equilibrium situation [43]. This makes an extension of the diode equation 2.11 by the photo current density term J_{ph} (see equation 2.13) necessary.

$$J(V) = \overbrace{\underbrace{J_0 \left[\exp\left(\frac{qV}{n_{id}k_BT}\right) - 1\right]}_{dark-diode} - J_{ph}}^{illuminated-diode} \tag{2.13}$$

To fully characterize a solar cell, several important parameters like the short-circuit current density (J_{sc}), the open-circuit voltage (V_{oc}), the fill factor (FF), the η and maximum power (P_{mp}) at maximum power point (mp) are needed (see figure 2.6). For the case of a short-circuit ($V = 0$) the solar cell delivers J_{sc}, which is equal to J_{ph} [43] (according to equation 2.14).

$$J(V = 0) = J_{sc} = J_{ph} \tag{2.14}$$

This leads to a strong correlation between the E_g of the absorber material and the J_{sc} of the solar cell. If the E_g increases less incident photons E_{ph} will be absorbed and contribute to the generation of charge carriers because the energy is not sufficient for the absorption process (see figure 2.7 (a)). The V_{oc} (see equation 2.15) is determined when no current is obtained from a solar cell (see figure 2.6) so that the total current is equal to zero [24,43].

$$J(V = V_{oc}) = 0 \tag{2.15}$$

The efficiency (η) of a solar cell device is described by the relation of maximum generated electrical power (P_{mp}) at mp to the optical power (P_{opt}) of incoming photons. The P_{mp} can be visualized by the rectangle of the maximum area in the $I-V$ curve, which is stretched by mp (x=V_{mp}/y=I_{mp}). The FF (see equation 2.16) describes the squareness of the $I - V$ curve (see figure 2.6) and is an important measure of the device quality [24].

$$FF = \frac{J_{mp} \cdot V_{mp}}{J_{sc} \cdot V_{oc}} \tag{2.16}$$

The efficiency η (see equation 2.17) of the solar cell can be evaluated with the help of the key parameters J_{sc}, V_{oc} and FF [18].

$$\eta = \frac{J_{mp} \cdot V_{mp}}{P_{opt}} = \frac{J_{sc} \cdot V_{oc} \cdot FF}{P_{opt}} \tag{2.17}$$

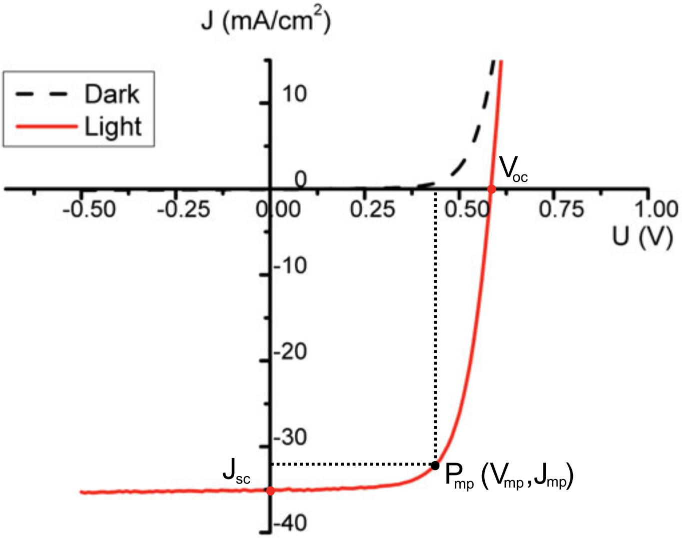

Figure 2.6: The schematic $I - V$ curve of a solar cell in the dark and under illumination condition with the characteristic parameters J_{sc}, V_{oc}, J_{mp}, V_{mp} and P_{mp}.

2.2.2 Ideal solar cell

In the SQ model the solar cell is described as a perfect absorber, which ensures the direct transfer of incoming photons (photon flux ϕ_{sun}) into J_{sc} [44]. Every photon is assumed to create one e^-/h^+ pair, the carriers are collected perfectly afterwards and the only allowed recombination processes are radiative. The band gap energy E_g displays the minimal photon energy above which the photon is absorbed, and the absorptance $a(E)$ is assumed to become 1 for values $E \geq E_g$ [45]. The J_{sc} under illumination is expressed through the photon flux from the sun ϕ_{sun} by integrating over the energy from E_g to ∞ (see equation 2.18).

$$J_{sc}(E_g) = q \int_{0}^{\infty} a(E)\phi_{sun}(E)dE = q \int_{E_g}^{\infty} \phi_{sun}(E)dE \tag{2.18}$$

Within the thermodynamic equilibrium and the principle of detailed balance [44], the photon fluxes which go inside a solar cell are equal to the photon fluxes going outside. In this approach the solar can be described by a perfect black body radiator. The emission properties of the solar cell are described by the black body radiation and the voltage dependency of the emission is approximated with an ideal diode under applied bias voltage V. The emitted photon flux ϕ (see equation 2.19) is described by a combination of Würfel's generalized Planck's law [46] together with Kirchhoff's law [44,45]:

$$\phi(V,E) = \frac{2\pi E^2}{h^3 c_L^2} \frac{1}{\exp((E - qV)/k_B T) - 1} \tag{2.19}$$

For small voltages ($E - qV >> k_B T$), the complex $\phi(V,E)$ term can be decoupled into black body radiation and a voltage dependent part (see equation 2.20):

$$\phi(V,E) \approx \underbrace{\frac{2\pi E^2}{h^3 c_L^2} \exp\left(\frac{-E}{k_B T}\right)}_{black\ body\ radiation} \quad \underbrace{\exp\left(\frac{qV}{k_B T}\right)}_{voltage\ dependent\ part} \tag{2.20}$$

The only process which is allowed to emit radiation in a SQ solar cell is radiative recombination of charge carriers, which results in a recombination current density J_{rec} (see equation 2.21):

$$J_{rec} = q \int_{0}^{\infty} a(E)\phi(V,E)dE = q \int_{E_g}^{\infty} \frac{2\pi E^2}{h^3 c_L^2} \exp\left(\frac{-E}{k_B T}\right) \exp\left(\frac{qV}{k_B T}\right) dE \tag{2.21}$$

Under thermodynamic equilibrium ($V = 0$) the total current density J must be zero: $J = 0 = J_{rec}(V = 0) - J_{bb}$. Here J_{bb} represents the photocurrent produced by black body radiation of the solar cell. This equation describes the fact that the photocurrent density in thermodynamic equilibrium (caused by black body radiation) is equal to the recombination current density under thermodynamic equilibrium (principle of detailed balance) [44]. J_{bb} only consists of a black body radiation part and has no voltage dependencies (see equation 2.22) [44].

$$J_{bb} = q \int_{0}^{\infty} \phi(V = 0,E) dE = q \int_{E_g}^{\infty} \frac{2\pi E^2}{h^3 c_L^2} \exp\left(\frac{-E}{k_B T}\right) dE \tag{2.22}$$

When the equilibrium is disturbed by an applied bias voltage V in the dark, the total dark current density is equal to $J_{dark} = J_{rec} - J_{bb} \neq 0$ (see equation 2.23) [44]. The prefactor J_0 in diode equation can be summarized as $J_0 = q \int_0^\infty a(E) \frac{2\pi E^2}{h^3 c_L^2} \exp\left(\frac{-E}{k_B T}\right) dE$, which leads to the well known diode law configuration in the dark (see equation 2.23).

$$J_{dark} = q \int_{0}^{\infty} \left(\phi(V,E) - \phi(V = 0,E)\right) dE = J_0 \left(\exp\left(\frac{qV}{k_B T}\right) - 1\right) \tag{2.23}$$

Under illumination the total J is extended by J_{ph}, which leads to (see equation 2.24):

$$J_{tot} = J_{dark} - J_{ph} \tag{2.24}$$

The V_{oc} (see equation 2.25) can be found for the condition J_{tot}=0 (along the procedure according to equation 2.15).

$$V_{oc}(E_g) = \frac{k_B T}{q} \ln\left(\frac{J_{sc}}{J_0} + 1\right) \tag{2.25}$$

The efficiency η is calculated by dividing V and J by the maximum of the product of V and J the optical power P_{opt} of incoming photons, per area and time (see equation 2.26):

$$\eta(E_g) = \frac{max(-JV)}{P_{opt}} = \frac{J_{mp}V_{mp}}{P_{opt}} \tag{2.26}$$

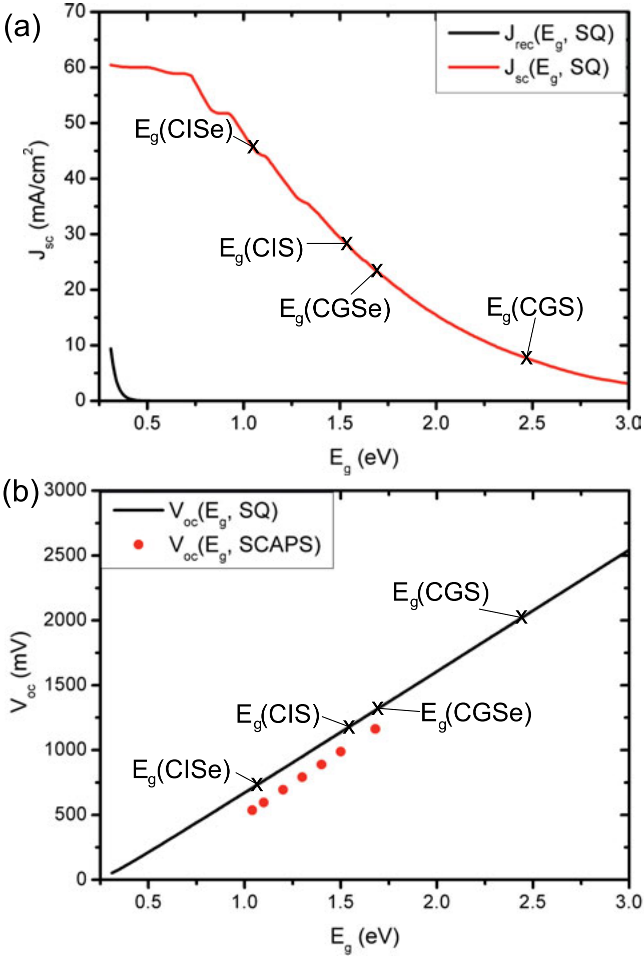

Figure 2.7: (a): According to the SQ limit the J_{sc} vs. E_g trend is shown. The J_{sc} decreases with E_g caused by absorption losses in the solar cell. The J_{sc} values of the individual ternary chalcopyrite materials CISe, CIS, CGSe and CGS are visualized. (b): In the case of the V_{oc} vs. E_g a linear increasing trend is determined.

In figure 2.7 (a) the calculated J_{sc}, in figure 2.7 (b) V_{oc} and in figure 2.8 (a) η vs. E_g are shown. The J_{sc} decreases with E_g (red line). In the case of

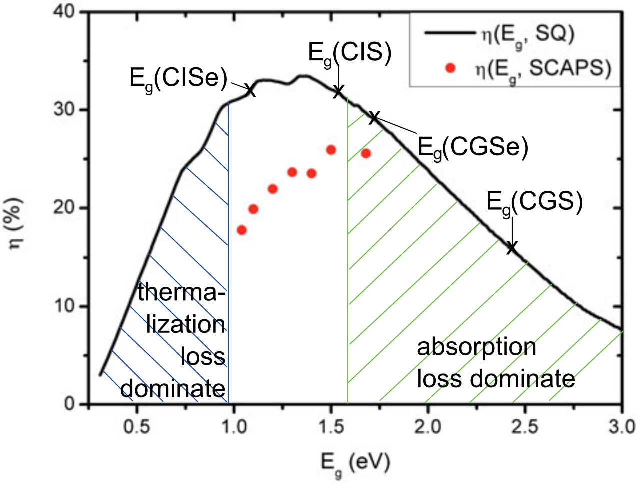

Figure 2.8: The η vs. E_g trend can be separated into two regions, for low E_g thermalization and for high E_g absorption losses dominate.

V_{oc} a linear increase with E_g is observed (black line). The η trend vs. E_g in figure 2.8 can be separated into a thermalization loss dominated ($E_g \leq 1$ eV) and an absorption loss dominated ($E_g \geq 1.6$ eV) region. The global maximal η of 33% is achieved for a solar cell material with $E_g = 1.35$ eV (also reported in [10]) under an AM1.5 spectrum. A second local maximum is located at 32.8% for 1.15 eV which is next to E_g of Si. The region of high η values extends from 1 to 1.45 eV. This can easily be achieved for CISSe and CIGSe by tuning the E_g with the help of different SSSe and GGI ratios respectively [47,48].

2.2.3 Real solar cells

In real solar cells additional loss mechanisms reduce the performance of the solar cell device. The different loss mechanisms [49] are divided into optical and collection losses affecting the QE and reducing the J_{ph} (see figure 2.9). The non-radiative recombinations include Auger and Shockley-Read-Hall (SRH) recombination. The Auger recombination process is a three particle interaction where an e^- and a h^+ recombine and the excess energy is transferred to an e$^-$ in the CB. Afterwards, the e$^-$ thermalizes to the CB edge by transferring the energy into heat. The SRH recombination describes the recombinations via trap states within the E_g region, where the energy is transferred to phonons. SRH recombinations lead to an increasing J_0, which reduces the V_{oc} and FF. In [9] for example the maximum, theoretical η of 28% is predicted for chalcopyrite solar cells, which is 5% lower than the SQ limit of 33%.

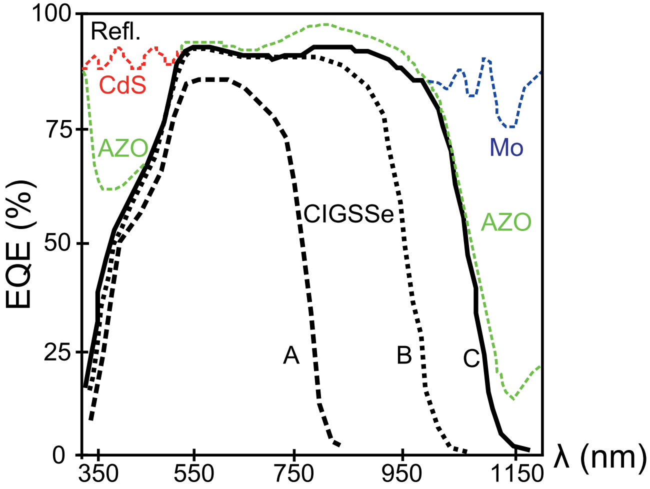

Figure 2.9: The schematic EQE shows the possible loss mechanism in a CIGSSe solar cell with different optoelectronic properties and E_g values (A $\propto$ 1.06 eV dashed, B $\propto$ 1.15 eV dotted and C $\propto$ 1.5 eV lined). For example reflection losses at the ZnO window layer, absorption losses in the CdS buffer and interface recombinations at the Mo back contact interface can occur. The dashed lines for Al:ZnO (AZO), CdS and Mo symbolize the maximal possible EQE without these losses. "The difference of the EQE towards the ideal 1" is also related to reflection losses (Refl.) at the solar cell surface. An increasing absorber E_g (C → A) results in a shifting band edge to lower values.

The inhomogeneities of the polycrystalline absorber lead to a further increase of J_0. There is still a large difference between the predicted maximum η of 28% and the current world record of η=22.6% by the ZSW [7], which still show the room for improvement but also the challenges considering the long time scale of chalcogenide research.

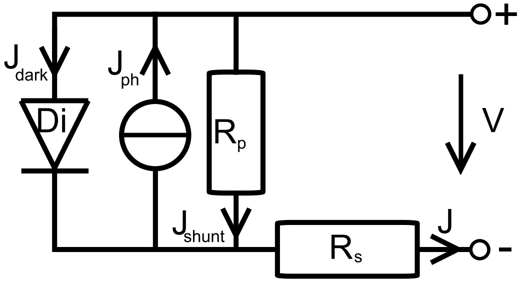

Figure 2.10: Schematic overview of the one diode model for solar cells with the current density J, the photo current density J_{ph}, the dark current density J_{dark}, the series resistance R_s, the shunt resistance R_p, the Diode Di and the voltage V.

It is very helpful to describe a solar cell in the equivalent circuit by the one diode or two diode model. For chalcopyrite solar cells the one diode model is a common description of the device structure [50]. In figure 2.10 the one diode model consists of a diode (J_{dark}), a series resistance (R_s), a parallel resistance (R_p) and the J_{ph} as the electric source [51]. The diode (Di) represents the p-n heterojunction of ZnO/CdS/CIGSSe and is characterized by n_{id} and J_0. Resistive effects in the h^+ and e^- transport result in contact resistance of the front and back contact as well as intrinsic sheet resistance of the semiconductors, which is summarized in R_s (series-connected to Di). R_p (parallel-connected to Di) describes parasitic current paths in the circuit [50], which are summarized in the parasitic current density J_{shunt}. The equivalent J-V equation 2.27 in dc mode can be divided into a dark-, shunt- and illuminated-part. Additionally, the real diode terms are included by the shunt-part and in the dark-part by the term $-R_sJ(V)$ in equation 2.28.

$$J(V) = J_{dark}(V) + J_{shunt}(V) - J_{ph} \tag{2.27}$$

$$J(V) = \underbrace{J_0\left[\exp\left(\frac{q(V - R_sJ(V))}{n_{id}k_BT}\right) - 1\right]}_{dark-part} + \underbrace{\frac{V - R_sJ(V)}{R_p}}_{shunt-part} - J_{ph} \tag{2.28}$$

]

2.2.4 Band gap grading in CIGSSe solar cells

One way to improve the optoelectronic properties of a solar cell is by introducing concentration gradients in the absorber in order to enhance the collection efficiency and to reduce recombination processes [52–57]. The influence of concentration gradients on the band diagram is shown for back and front surface grading in figure 2.11. In [58] it has been demonstrated that Ga and S have different impacts on the band diagram of the CIGSSe system described by the width of the SCR ($x_n + x_p$) and the build-in voltage (V_D). The addition of Ga leads to an increasing E_{CB} minimum position and S addition decreases mostly the E_{VB} maximum position [58] with reference to the Fermi energy E_F. Back surface grading is performed by increasing the Ga amount in the absorber towards the back contact (case 1). The E_{CB} shifts to higher energies with respect to E_F. The minority charge carriers (e^-) are pushed back into the p-n junction through the back surface grading which reduces recombination at the back contact. Front surface grading can be performed either by increasing the E_{CB} with respect to E_F by an increasing Ga amount (case 2) or by decreasing the E_{VB} with respect to E_F by increasing S amount (case 3). In both concepts (case 2 and 3) the E_g is increased according to the relationship of E_g with the Ga/(Ga+In) and S/(S+Se) ratios (see again figure 2.1 from the beginning of the chapter). An increased E_g at the p-n heterojunction can reduce the recombination of charge carriers and leads additionally to a better band adjustment.

In order to assess more quantitatively the influence of E_g grading, one can calculate the improvements with the help of an analytical approach (according to the procedure in [52, 52, 53, 59]) which is based on the analysis of a device structure with a linear concentration gradient in the absorber towards the back contact. With the SCAPS numerical simulation approach (according to procedure in [60–62]), one can flexibly calculate the changes for linear front and back surface graded absorber structures (appropriate absorption input data are needed). In the following sections, the basic concepts of the numerical and analytical approach will be introduced.

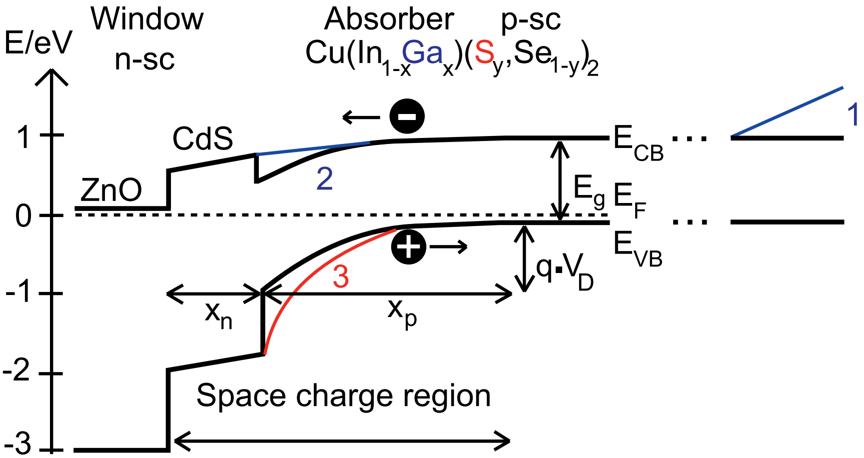

Figure 2.11: Schematic band structure of CIGSSe with the window layer based on n-ZnO and n-CdS as well as the absorber layer based on p-CIGSSe. The possible ways to introduce gradients in the CB and VB are shown for an increasing Ga amount next to the back contact (case 1) or next to p-n heterojunction (case 2), and for an increasing S amount next to the heterojunction (case 3).

SCAPS numerical simulation approach

With the SCAPS numerical simulation approach it is possible to calculate the performance of real solar cells based on realistic input parameters. One input parameter is the absorption profile of the absorber structure. In the case of CIGSSe absorbers used here there are absorption coefficients [63] available for certain material compositions (GGI=0, 0.31, 0.45, 0.66, 1 and SSSe=0, 1). In order to perform electrical simulations on thin film solar cells five fundamental semiconductor equations have to be solved [24, 64]. The derivation for the SCAPS simulations, especially for solar cells in idealized 1D structures (basis of the SCAPS calculation) is shown in the appendix A.1.

In [56, 61, 65, 66] examples for modeling of E_g grading are performed with different thin film solar cell simulation tools. In this work, different concentration gradients are introduced in the absorber next to the back and front contact to perform linear variations in the band diagram. The other

Table 2.1: Input parameters for the SCAPS simulation model with three individual CIGSSe absorber layers, which is used in the thesis. The back and front contact surface recombination/thermal velocity for e$^-$ and h$^+$ have the same values $v_e = v_h = 1E7$ cm/s.

Input	**Layer 1**	**Layer 2**	**Layer 3**	**CdS**	**i-ZnO**
ε	10	10	10	10	10
χ (eV)	4.5	4.5	variable	4.45	4.55
E_g (eV)	variable	variable	variable	2.45	3.4
μ_n ($\frac{cm^2}{Vs}$)	400	400	400	50	50
μ_p ($\frac{cm^2}{Vs}$)	20	20	20	20	20
N_C ($\frac{1}{cm^3}$)	2E18	2E18	2E18	2E18	4E18
N_V ($\frac{1}{cm^3}$)	2E18	2E18	2E18	1.5E18	9E18
N_A ($\frac{1}{cm^3}$)	7E15	7E15	7E15	0	0
N_D ($\frac{1}{cm^3}$)	0	0	0	1E15	5E17
v_e ($\frac{cm}{s}$)	1E7	1E7	1E7	1E7	1E7
v_h ($\frac{cm}{s}$)	1E7	1E7	1E7	1E7	1E7

layers are kept constant, like the CdS buffer with 50 nm and the i-ZnO/n-ZnO front contact with 1000 nm. For a detailed analysis of different back and front surface grading properties the CIGSSe absorber is separated into the three pieces CIGSSe 1, CIGSSe 2 and CIGSSe 3 with a total thickness of 1.5 μm (see figure 2.12). The basic material-specific input parameters based on [56, 66] are summarized in table 2.1. N_C and N_V characterize the density of states (DOS) in the CB and VB respectively; the N_A and N_D represent the acceptor and donor densities. The recombination/thermal velocities for the back and front contact are v_e and v_h. The dielectric constant ε=10 is equal for all the films. The χ is the same for the CIGSSe layers 1 and 2 (=4.5 eV). For layer 3 (front layer) χ can vary with S amount within the model. μ_n=400 cm$^2/s$ and μ_p=20 cm$^2/s$ represent the e$^-$ and h$^+$ mobility, which have the same values for all the three CIGSSe layers. In figure 2.12 an overview about the basic parameters is given, where the linear CB grading at the back surface is performed with a Ga/In concentration gradient and a variable grading distance $d1$ and/or $d2$. The front surface grading can either be achieved by different Ga/In ratios which increase the E$_{CB}$ or different S/Se ratios decrease the E$_{VB}$. For a decreasing E$_{VB}$ also the χ is changed, which has to be considered in the calculations.

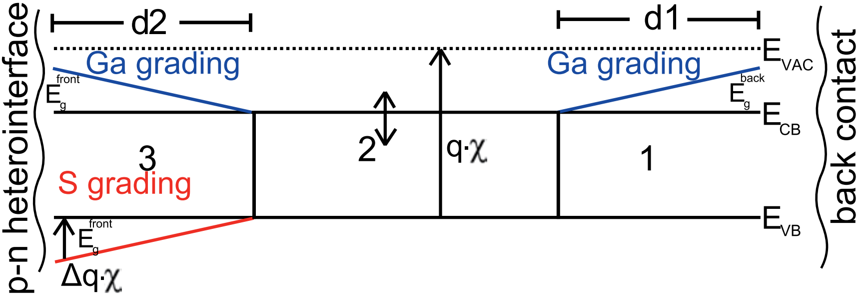

Figure 2.12: E_g model of the CIGSSe thin film used in this work with linear back and front surface grading. The absorber is divided into three regions symbolized by the numbers 1, 2 and 3. In the case of Ga grading the χ stays constant but for S front grading χ is increased by $\Delta\chi$.

In the following subchapters, a number of calculations for different linear back and front surface graded CIGSSe are presented. In these calculations, the back and front surface $E_g^{front/back}$ and the width of the grading region ($d1$ and $d2$) are varied (see figure 2.12).

Analytical E_g gradient simulation approach

Another way to identify the influence of concentration gradients in the absorber material on the solar cell performance is the analytical simulation approach as given by [52, 53]. In this approach the E_g is linearly varied from an E_g^{min} value towards an E_g^{max} value across the absorber layer thickness. In order to compare these values to SQ calculations the E_g^{min} is kept constant. The analytical approach is based on the concept to introduce an effective absorption coefficient α_{eff} to describe the photon absorption of linear graded absorbers [52, 53]. A linear increasing E_g leads to a linear decreasing photocurrent. The absorbed photons result in a carrier generation rate g (see equation 2.29), which can be expressed by the absorption coefficient α and the photon flux density ϕ. Altogether g is equal to the photon absorption rate $\alpha\phi$ [52].

$$g = -\frac{d\phi}{dx} = \alpha\phi = \alpha\phi_0 \exp(-\alpha x) \tag{2.29}$$

The advantage of the analytical approach lies in the ability to estimate the cell performance for different geometries with the input parameter of the E_g values, according to the procedure in [52]. However, some simplifying concepts for calculating J_{sc} and V_{oc} need to be introduced. The derivation of the current density of the cell with a graded absorber J_{grad} based on an effective absorption coefficient α_{eff} defined for different energy sections is shown in the appendix A.2.

In table 2.2 a summary of the E_gs of the most important solar cell materials Si, GaAs, $\mathrm{CuIn_{0.75}Ga_{0.25}Se_2}$, CISe, CGSe and CGS (different x=Ga/(Ga+In) and y=S/(S+Se) ratios) is shown with the corresponding calculated J_{sc} values according to SQ (J_{sc}^{SQ}), the analytical E_g gradient model (J_{sc}^{grad}) and via SCAPS simulations (J_{sc}^{SCAPS}). Under short-circuit conditions ($J = J_{sc}^{grad}$), J_{sc}^{grad} is calculated with the defined α_{eff} values for different E_g^{max} ($\mathrm{E}_g^{min} = 1.1$ eV stays constant) values reaching from 1.1 eV to 2.4 eV (see figure 2.13 (a), black line). In comparison also the values for non-graded absorbers according to the SQ model (which was already calculated before) for constant $E_g = E_g^{max} = E_g^{min}$ (see figure 2.13 (a), red line) are shown. In figure 2.13 (b) the schematic E_g profile is shown for a graded absorber with E_g^{max}, E_g^{min} which defines the grading of the absorber. Additionally, the absorber thickness d and the critical distance d_c, which characterizes the absorptance, are visualized.

In order to estimate the effect of the grading on the V_{oc} of the solar cell one has to introduce the term of internal electric field ξ_{grad} induced by the grading [52]. In the case of E_g variations an additional force similar to an electric field (drift force) acts on the e^-. The e^- current density J_n (see equation 2.30) depends on the electric potential variations (dψ/dx), carrier diffusion coefficient (D_n), electron concentration ($n(x)$), μ_n and χ [52].

$$J_n = \underbrace{-q\mu_n n\left(\frac{d\psi}{dx} + \frac{1}{q}\frac{d\chi}{dx}\right)}_{drift} + \underbrace{qD_n\frac{dn}{dx}}_{diffusion} \tag{2.30}$$

In ideal solar cells the dominant current transport mechanism is carrier injection at the (hetero)junction and diffusion as a consequence of the carrier concentration gradient at each side of the junction [24,67]. However,

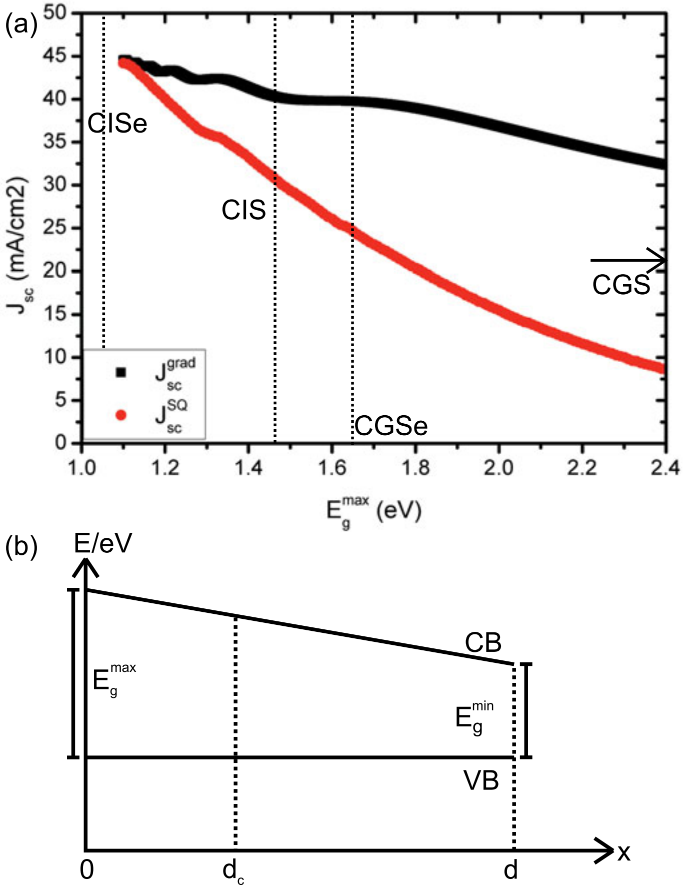

Figure 2.13: (a): Calculated J_{sc} values for a linear graded E_g (black thick line), and according to the SQ model for constant E_g (red thick line). (b): The schematic E_g profile of a linear graded absorber with a variable E_g^{max} ranging from 1.1-2.4 eV and a fixed E_g^{min} = 1.1 eV. d describes the total thickness of the absorber and d_c the critical distance.

Table 2.2: Overview of the different J_{sc} values for a linear graded E_g ($E_g^{min} = 1.1$ eV for all structures and the corresponding E_g values are equal to E_g^{max}) and the ideal SQ E$_g$ ($E_g^{max} = E_g^{min} = E_g$) of different absorbers. The attractive solar cell materials Si and GaAs are also included in the calculations.

Material	E_g **(eV)**	J_{sc}^{grad} **(mA/cm^2)**	J_{sc}^{SQ} **(mA/cm^2)**
Si (indirect E$_g$)	1.1	44.48	44.18
$CuIn_{0.7}Ga_{0.3}Se_2$	1.2	43.22	40.07
GaAs	1.42	40.96	32.39
CIS	1.52	39.9	28.76
CGSe	1.68	39.66	23.69
CGS	2.4	32.32	8.58

in real solar cells recombination via traps at the junction interface or Shockley-Read-Hall (SRH) recombination at deep levels within the SCR play an important role, which limits the V_{oc} [67]. All kinds of recombination strongly influence the diode characteristics of a thin film solar cell. There is a correlation between V_{oc} and E$_g$ (see equation 2.25), which can be extended for graded E_g solar cells with a J_{sc}^{grad}. In [67] an approximation of the J_0^{grad} for graded E_g structures is found, which in a thin film solar cell is dominated by deep level recombination in the SCR [67] (see equation 2.31).

$$J_0^{grad} \approx J_0^{min} \left(\frac{2k_BT}{\Delta E_g}\right) \left[1 - \exp\left(-\frac{\Delta E_g}{2k_BT}\right)\right], \; \Delta E_g = E_g^{max} - E_g^{min} \tag{2.31}$$

In this case $\Delta\Psi_g = \Delta E_g/e$ displays the potential change induced by E_g grading. The J_0^{min} is the dark saturation current density for a material with $E_g = E_g^{min}$ [67]. The dark characteristics along J_0^{grad} are used for estimating the V_{oc}^{grad} values according to the correlation 2.25 (see table 2.3). J_{sc}^{grad} is already known from previous calculations (see table 2.2). In figure 2.14 the $\Delta V_{oc} = V_{oc}^{grad} - V_{oc}^{constant}$ trend is shown to visualize the improvements due to a linear graded absorber. In this case $V_{oc}^{constant}$ is the V_{oc} value of a solar cell with a non-graded absorber and a constant $E_g = E_g^{min} = 1.1$ eV. Figure 2.14 can be interpreted in a way that the difference/improvement of V_{oc} of a solar cell with an absorber E_g=1.1 eV towards a solar cell with a linear graded $E_g^{max} \rightarrow E^{min}$=1.1 eV is visualized.

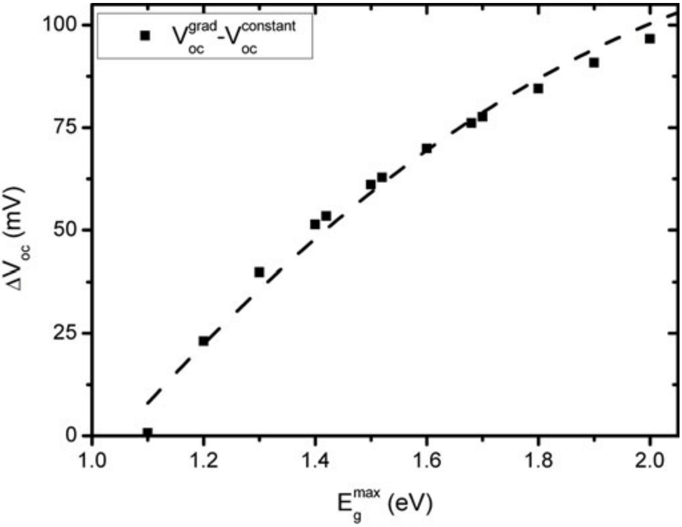

Figure 2.14: Improvement of V_{oc} ($\Delta V_{oc} = V_{oc}^{grad} - V_{oc}^{constant}$) due to a linear graded absorber shown for different E_g^{max} values.

It has become quite clear that a graded absorber in a CIGSSe solar cell can achieve higher J_{sc} values in comparison to absorbers with constant E_g

Table 2.3: Overview of the different V_{oc} values for a linear graded E_g (E_g^{min}=1.1 eV for all structures and the corresponding E_g values are equal to E_g^{max}), the ideal SQ with a constant E_g ($E_g^{max} = E_g^{min} = E_g$) and the SCAPS simulated E_g profiles of a CIGSSe absorber. The calculations are also performed for the attractive solar cell material Si and GaAs for comparison.

Material	E_g **(eV)**	V_{oc}^{SQ} **(mV)**	V_{oc}^{SCAPS} **(mV)**
Si (indirect E_g)	1.1	768.9	596
$CuIn_{0.7}Ga_{0.3}Se_2$	1.2	862.4	631.4
GaAs	1.42	1069.4	660.4
CIS	1.52	1163.3	-
CGSe	1.68	1314	676.7
CGS	2.4	1993.2	-

due to reduced absorption losses. Furthermore, it was shown that the V_{oc} value in the device can be optimized with the help of graded absorbers.

Comparison of the two models:

By comparing the J_{sc}^{grad} with the J^{SQ} values from the analytical model (see figure 2.13 (a)), it becomes clear that a graded absorber increases the absorption in the solar device. For increasing E_g^{max} there is an increasing difference between J_{sc}^{SQ} and J_{sc}^{grad} values (see figure 2.13 (a)). In general, the SCAPS and the analytical model show similar trends of J_{sc} improvements with graded absorbers. These results may serve as a motivation for further investigations of graded absorber structures and the characteristics like the shape of the concentration gradient.

CHAPTER 3

Experimental procedure

The following subchapters introduce the SEL deposition process, which belongs to the family of two-step processes, as well as the co-evaporation process. Additionally, a brief introduction into the relevant tools for structural and electronic analysis of CIGSSe thin films and solar cells is given.

3.1 Deposition process for chalcopyrite solar cells

A 3 mm thick commercially available standard float glass (SFG) is used as substrate and Na delivery during chalcopyrite formation. For some special experiments with high temperature processes, where the Ga/In interdiffusion is investigated, also 2 mm thick high temperature glass (HTG) from Schott is used. By means of magnetron sputtering, 500 nm Mo back contact is deposited above the glass. The Mo back contact consists of a 100 nm seed layer which is sputtered at a higher pressure ($p \approx 10^{-3}$ mbar) and a 400 nm highly conductive layer which is sputtered at a lower pressure ($p \approx 10^{-4}$ mbar). For some experiments, a modified Mo back contact is grown in order to prevent the fast $MoSe_2$ growth in the rapid thermal processing (RTP). The absorber layer is grown along the prominent deposition route of the SEL process [68–70], which stands in competition to the co-evaporation (CE) process [71–73]. The p-n junction is completed by a 50 nm CdS buffer via chemical bath deposition (CBD) and the window layer is added in the form of a 50 nm i-ZnO via radio frequency (RF) sputtering plus 400 nm Al:ZnO (AZO) via direct current (DC) sputtering. Additionally, a Ni/Al grid is deposited on the AZO via electron beam deposition, to achieve a better current distribution.

3.1.1 Co-evaporation (CE) process

CE generally describes a process where the chalcopyrite formation takes place directly during the element deposition on the hot substrate. There are different process configurations like the single layer, the two- and three-stage CE process. In the single layer CE process, the four elements Cu, In, Ga and Se are evaporated on the substrate with different element fluxes simultaneously. A Cu-rich growth period during the process leads to a recrystallization of the thin film, which is realized in the two- and three-stage CE process by varying the metal fluxes. The chalcogen flux is always overstoichiometric (certain chalcogen excess is needed) by a typical ratio Se/metal ≥ 5. The two-stage CE process [23, 74] is structured in a first Cu-rich growth phase, which is followed by a second stage with lower Cu rate leading to an overall Cu-poor composition at high growth temperatures. The three-stage CE process [23, 75] involves additional degrees of freedom, and is structured in a first In+Ga+Se deposition step at 300 °C. Then Cu+Se is deposited at temperatures ≥ 500 °C until the film becomes Cu-rich leading to the desired recrystallization of the grains. Finally, In+Ga+Se is deposited to ensure an overall Cu-poor film. Referring to the phase diagram (see figure 2.3 (b)), the growing thin film passes through the Cu_2Se - $(In,Ga)_2Se_3$ quasi-binary tie line, starting in the left regime (stage 1), where the $(In,Ga)_2Se_3$ layer is formed. In stage 2 Cu is introduced and the film composition changes from left to right according to the phase diagram (see figure 2.3), whereby initially the very Cu-poor compounds $Cu(In,Ga)_3Se_5$ and $Cu(In,Ga)_5Se_8$ are formed. When a Cu amount of 24.5 at.% is reached the CIGSe film becomes single phase. For Cu/(Ga+In) (CGI) ≥ 1 the secondary phase CuSe is formed because the excess Cu precipitates in this secondary phase. During the process steps, an elaborated in-situ analysis like mass spectrometry is needed to guarantee the optimal GGI and CGI ratios. Afterwards, the growing film passes again towards the overall Cu-poor regime by increasing the III/Cu metal flux ratios, which is necessary for good solar cell performance. With the three-stage CE process, the most efficient CIGSe solar cells were processed but the complexity of the process makes the transfer to the production line more challenging.

3.1.2 Stacked elemental layer (SEL) process

By separating the deposition from the crystal formation, which is the basis of the two-step or sequential process, an easy up-scaling towards production line can be performed [76–80]. At first, a stack of precursor layers is deposited on the substrate which can consist of elemental metal layers, alloys or compounds. In this work, metal layers are sputtered from a CuGa alloy and an In elemental target by means of DC sputtering ($p \approx 10^{-3}$ mbar), which is followed by Se as well as S evaporation with two separate Knudsen cells. The base pressure in the evaporation chamber is approximately 10^{-5} mbar during Se evaporation and for S evaporation approximately 10^{-4} mbar. The Se/In/CuGa or S/Se/In/CuGa layer stacks are then subsequently annealed at temperatures around 550 °C in a N_2-Se/S atmosphere in a closed chamber [81]. The GGI and CGI ratios are controlled by the metal layer thickness ratio. During the process, the chalcogens are always supplied in excess. In the following, the reaction scenarios are described in more detail for the absorber materials CISe, CIGSe and CIGSSe because the SEL process is the key element of the thesis. Furthermore the evaporation of Se, S and their combination is shortly discussed.

CISe: The phase formation reaction during the SEL process [82–84] starts from the deposited metallic precursor layer (see figure 3.1, first box at the top), which is transferred to $Cu_{11}In_9$ at temperatures around 150 °C (also discussed in chapter 4.1.1). At the interface, a controlled growth reaction of the intermetallics with Se is performed. The process is dominated by the dissolving Cu which leads to the binary selenide $CuSe_2$ and free In [83]. Furthermore, the free In reacts with Se to the binary selenide In_4Se_3, which creates InSe over a nucleation reaction process (see figure 3.1, third box).

During the In selenide formation, the existing Se is consumed so that the transformation $CuSe_2 \rightarrow CuSe \rightarrow Cu_{2-x}Se$ (see figure 3.1, fourth box) occurs over peritectic decays [83]. Finally, the CISe formation proceeds (see figure 3.1, fifth box) over the reaction path InSe with CuSe and InSe with $Cu_{2-x}Se$ in the temperature regime around 340-550 °C (discussed in chapter 4.1.1) [82, 83].

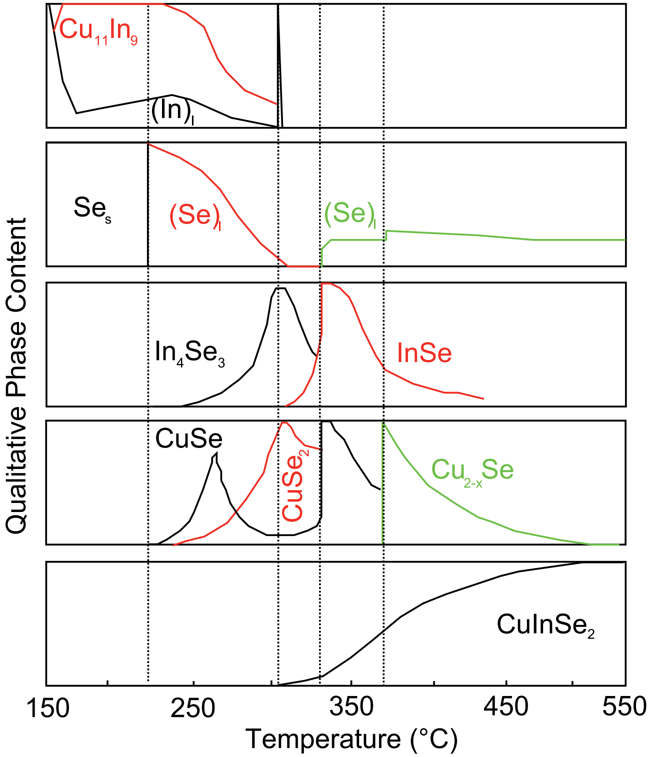

Figure 3.1: Phase formation of the CISe during the temperature dependent SEL process. The different phase amounts are qualitatively shown for the temperature regime in between 150-550 °C (according to [82]). The SEL reacts to intermetallics towards the binary selenides, finally reaching the ternary CISe compound.

<u>CIGSe</u>: The quaternary precursor CuGa-In-Se [85] forms at first Cu_9Ga_4 and $Cu_{11}(In,Ga)_9$ as a result of intermetallic reactions. The $Cu_{11}(In,Ga)_9$ is consumed by Se, whereby Cu_9Ga_4 is enriched on the substrate side. This metallic phase is selenized and $Cu(Ga)Se_2$ is formed which decomposes into

the binary selenides GaSe and CuSe. After the transformation of CuSe into $Cu_{2-x}Se$ the CGSe crystal starts to grow, from the reaction kinetic point of view slower then the CISe crystals. Finally, the mixed crystal phase CIGSe is formed in the temperature regime from around 430-550 °C [85], mainly driven by Ga/In interdiffusion reactions.

CIGSSe: In [86], a detailed description of the complex pentanary phase formation is given, where the growth process is divided into three different S/(S+Se) (SSSe) sections like a Se- (SSSe=0-0.1), intermediate- (SSSe=0.2-0.25) and S-like (SSSe=0.3-1) CIGSSe growth path. The chalcogen substitution of Se through S within the Cu(S,Se) and the Cu dealloying from the $Cu_9(Ga,In)_4$ phase are decreased with a reduced S/(S+Se) ratio [86]. There are two chalcopyrite growth paths for the cations In and Ga, namely In-rich and Ga-rich CIGSSe, which undergo a similar growth process. The Ga/In interdiffusion is furthermore kinetically inhibited with increasing SSSe ratio [86]. The interface properties towards the back contact also change with respect to a reduced $Mo(S,Se)_2$ formation with increasing SSSe ratio [86].

Se: Se condensates in the amorphous phase (a-Se) on the metallic precursor layer and crystallizes in the hexagonal modification (h-Se) until the In melting point (roughly around 156 °C) is reached. Until then, there has not been any reactions between chalcogens and the metals. However, at the melting point of crystalline Se around 220 °C the Se melt reaction process between Se and the already formed intermetallic compounds is initiated [87].

Se together with S: The thin film consists of a-Se(S), a-S_xSe_y or c-S(Se) and the intermetallics. At 110 °C, the crystallization of S_xSe_y and Se(S) takes place. The ratio of S/Se in the evaporated S_xSe_y layer strongly depends on the S content before annealing. Additionally, the melting temperature of the S_xSe_y layer decreases with S amount [86].

3.2 Characterization methods

The morphologies of the thin films are observed via scanning electron microscopy (SEM) in cross sections. To quantitatively analyze the different crystal phases, X-ray diffraction (XRD) investigations in Bragg Brentano geometry ($\theta - 2\theta$ geometry) are done. For a better insight into phase formation in-situ XRD (IXRD) investigations during crystal growth are performed. In order to study surface properties, Raman spectrocopy is used. The spectral photoluminescence (PL) analysis is performed to investigate the optoelectronic properties. For depth resolved concentration analysis, glow discharge optical emission spectroscopy (GDOES) and secondary ion mass spectroscopy (SIMS) are performed. To characterize the electronic properties of the device, current voltage (I-V) and external quantum efficiency (EQE) measurements are conducted.

3.2.1 Optical and structural characterization techniques

The interaction of radiation and matter plays an important role in material characterization, leading to a variety of analyzing tools. The incident light interacts with the matter and is either reflected or transmitted. These processes are described by the macroscopic phenomena of light refraction and reflection. In the material also some microscopic phenomena can take place like luminescence after the absorption of the incident light or the incident light can also be scattered elastically and inelastically.

(a) Optical

Photoluminescence spectroscopy

In general luminescence describes the non-thermal emission of light. In this case the solid state is disturbed from its thermal equilibrium state to the excited state, which leads to the emission of light afterwards in order to reach the equilibrium state again [88]. The disturbance can occur through different forms of excitations like an external voltage (electroluminescence), an incident e^- beam (cathodoluminescence), and by the excitation through absorbed photons (photoluminescence, PL) [21]. PL in a semiconductor material describes the process of excitation/creation of e^-/h^+ pairs by absorption of photons, and the subsequent radiative recombination process. The basic transitions are divided into interband transition, transition involving chemical impurities and intraband transitions [24]. For lower temperatures excitonic and acceptor-donor transition are preferred. With increasing temperature, the probability for free-bound and band-to-band transitions increases due to the fact that photoexcited charge carriers are thermalized inside the bands [21]. Not all transitions inside a semiconductor are radiative, for example the non-radiative Auger process [24]. The PL efficiency is estimated by the ratio of radiative to non-radiative transitions and is related to the amount of defects [21]. For CIGSSe, the dominant PL transition strongly depends on the CGI, GGI and SSSe ratios. For composition graded CIGSSe material, the interpretation of PL spectra is very difficult due to their complexity and the lack of models [89]. Additionally, it is possible to obtain the value of the GGI and SSSe ratio respectively for the material inside the exciting photon penetration depth from the PL peak position [89]. However, when both elements Ga and S are present in the region of interest, it is hard to distinguish which element causes the E_g shift when introduced (dominant process characterized: interband transition). For calculating the penetration depth, one has to take into account the α of the material at the excitation wavelength (λ) of the PL laser excitation source. The current experimental setup consists of a laser source with an excitation wavelength of λ=830 nm working at room temperature, the incident laser beam is tilted against the surface normal.

Raman spectroscopy

Raman spectroscopy is an optical method which is based on inelastic scattering processes of photons with vibrational excitations in the material. The position and the line shape of the Raman lines depend on the chemical composition and crystalline quality. The combination of a Raman spectrometer with an optical microscope leads to a high spatial resolution roughly around 1 μm [21,90]. Light scattering is in general a photon-matter interaction. The process of Rayleigh scattering (elastically scattered light) describes a mechanism in which the scattered light has the same frequency as the incident light. Inelastic scattering is divided into Brillouin and Raman scattering, referring to inelastic scattering of light through acoustic phonons and optical phonons respectively. An incident photon with the energy $\hbar\omega_I$ excites the electron system and an e^-/h^+ pair is created. The resulting e^- interacts with a phonon and leads to the emission (Stokes process) and absorption (Anti-Stokes process) of one phonon respectively with the energy $\hbar\omega_0$. The e^-/h^+ pair is scattered into the transition state. Afterwards the recombination of an e^-/h^+ pair under the emission of a scattered photon with the frequency ω_s is performed. For all scattering processes, the laws of energy and momentum conservation are valid (see equation 3.1 and 3.2). For this case "+" stands for the Anti-Stokes and "-" for the Stokes process respectively. $\vec{k}_s$, $\vec{k}_I$ and $\vec{q}$ are the wave vectors of the scattered photon, incident photon and Stokes or Anti-Stokes phonon.

$$\hbar\omega_s = \hbar\omega_I \pm \hbar\omega_0 \text{ law of energy conservation} \tag{3.1}$$

$$\hbar\vec{k}_s = \hbar\vec{k}_I \pm \hbar\vec{q} \text{ law of momentum conservation} \tag{3.2}$$

In this work a conventional Raman setup has been used which consists of a laser source, focusing and collection optics and a wave length dispersive spectrometer. The penetration depth of the frequency doubled Nd:YAG laser with 532 nm emission wavelength (WITEK Raman microscope in back-scattering geometry) is roughly about 100 nm inside the CIGSSe absorber [90]. The dominating vibration in $\mathrm{Cu}^{I}(\mathrm{In,Ga})^{III}\mathrm{Se}_2^{VI}$ chalcopyrite compounds is called A1 mode originating from the Se^{VI} atom movement, while the Cu^{I} and $(\mathrm{In,Ga})^{III}$ atoms remain in their positions [91–94]. For pure CISe absorbers the A1 mode is located in the range of 173-174 cm^{-1}, for CGSe at around 184 cm^{-1}, for CIS at 290 cm^{-1} and for CGS at 310 cm^{-1} at 300 K. For CIGSe absorbers with a GGI ratio of 0.3 the A1 mode shifts to values around 176-178 cm^{-1} [95]. The frequency of the A1 mode shifts up linearly with the Ga amount and therefore the A1 mode position can serve as an indicator for the GGI ratio inside the CIGSe surface [95]. When S is present in the CIGSSe material, the A1 mode intensity of CISe and CIS is very sensitive on the SSSe ratio. With increasing SSSe ratio, the A1 mode of CISe shifts up linearly and the A1 mode of CIS remains on its position, which is described as the two mode behavior. Additionally, the width of the A1 mode (FWHM) of Cu-poor absorbers is enlarged due to an increased defect density and an inferior crystal quality. In the case of CIGSe, the intensity of the A1 mode has a maximum next to the stoichiometric point because there is the smallest amount of chemical disorder in the crystal system [90]. An E mode is located at 210 cm^{-1}, which is associated with the vibration of anions and cations which can move together in phase or antiphase inside the crystal lattice [96]. The B1 mode characterizes the vibration along the bond directions Cu-Se, Ga-Se and In-Se [91]. The elemental Se mode is found at 239 cm^{-1}, which disappears above the Se melting temperature [97]. For Cu-poor absorbers with CGI ≤ 0.8, a shoulder mode becomes visible at 150 cm^{-1}, which is attributed to the ordered defect compound (ODC) phase $Cu(In,Ga)_3Se_5$. For Cu-rich absorbers with CGI ≥ 1, a mode at 260 cm^{-1} appears (CuSe A1 mode), which indicates CuSe segregation on top of the CIGSe absorber.

(b) Structural

X-ray diffraction

X-ray diffraction is a powerful tool for observing the crystal structure of polycrystalline thin films and gives informations about the phase formation properties of CIGSSe and back contact. In this work, different methods like powder diffraction, grazing-incidence XRD (GIXRD) and IXRD are used to analyze bulk, depth resolved and time-dependent characteristics of the CIGSSe absorber.

Most important CIGSSe reflections: The three strongest reflections in the chalcopyrite structure are the 112, the overlapping 220/204 and 312/116. The alloying of the material has similar effects on the individual reflection positions (Vegard's law) and may also cause asymmetric broadening of the reflection profile in case of gradients. The lattice constants of CISe, CGSe, CIS and CGS are well known from several publications [29, 98]. Vegard's law predicts a linear relationship between material composition and lattice constant. With the help of different GGI and SSSe ratios a large variety of lattice constants a and c can be achieved (see equation 3.3 and 3.4), which also strongly influences the optoelectronic properties.

$$a(x,y) = a_{CuInSe_2} + a_{GGI} \cdot x + a_{SSSe} \cdot y + a_{nonlin} \cdot x \cdot y \tag{3.3}$$

$$c(x,y) = c_{CuInSe_2} + c_{GGI} \cdot x + c_{SSSe} \cdot y + c_{nonlin} \cdot x \cdot y \tag{3.4}$$

The lattice constants of the unit cell for different x=GGI and y=SSSe ratios are $a(x,y)$ (in plane) and $c(x,y)$ (out of plane), and they contain the lattice constants a_{GGI}, a_{SSSe} and the non-linear term a_{nonlin}.

Powder diffraction in $\theta - 2\theta$ geometry: Monochromatic X-ray radiation is directed towards a polycrystalline material under the angle θ and the diffracted beam is collected by a detector system. The condition for constructive interference is described in Bragg's law (see equation 3.5). In this context n describes the order of diffraction, λ the wavelength of X-ray radiation, θ the angle between the incident X-ray beam and the lattice planes where constructive interference results. d_{hkl} is the distance between neighboring/consecutive lattice planes with Miller indices (hkl) [26].

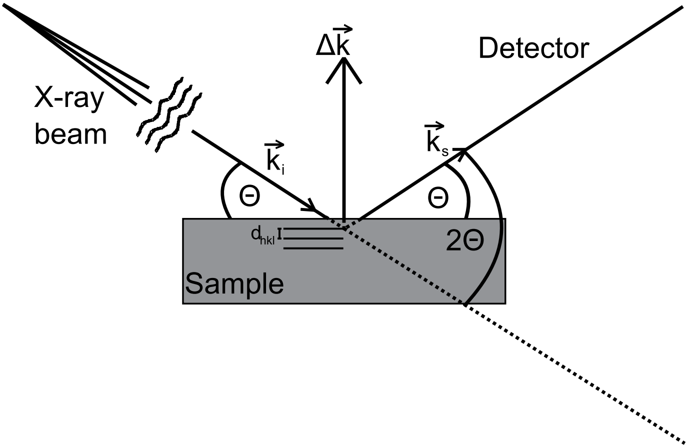

Figure 3.2: Fundamental Bragg Brentano geometry for thin film analysis with a perpendicular scattering vector $\vec{k}$ to the substrate surface for all θ angles. The incident X-ray beam is directed on the thin film material under the angle θ and the diffracted beam is collected by a detector.

$$n\lambda = 2d_{hkl}sin(\theta) \tag{3.5}$$

It is characteristic for Bragg Brentano geometry that the scattering vector $\Delta\vec{k} = \vec{k}_s - \vec{k}_I$ is always perpendicular to the lattice planes of the crystal for different angles θ. $\vec{k}_s$ and $\vec{k}_I$ represent the incident and scattered vector. The hkl describes the Miller indices of the corresponding lattice plane. For a further description of the diffracted wave front, also the atom arrangement in the unit cell has to be taken into account. In the kinematic approximation multiple scattering is neglected [26], which results in the relationship between diffracted intensity I and the square of the absolute value of the structure factor F_{hkl} (see equation 3.6).

$$I \propto |F_{hkl}|^2, \ F_{hkl} = \sum_{n=0}^{N} f_n \exp(2\pi i \cdot [hx_n + ky_n + lz_n]) \tag{3.6}$$

F_{hkl} is the fourier transformation of the e$^-$ density and N displays the number of non-equivalent atomic positions in the unit cell. x_n, y_n, z_n represent the relative scaled atomic coordinates in the unit cell. f_n denotes the atomic scattering factor, which considers the distribution of the e$^-$ density of the atoms [21]. The measurements are performed by a Bruker D8 Advance DaVinci-Cu in the angle range from $2\theta = 10\,^\circ - 85\,^\circ$, where all the interesting CIGSSe reflections are located.

Grazing incidence XRD: To ensure a higher path length l of X-rays into the thin film material as well as being more surface sensitive an asymmetric XRD scan (GIXRD) with a fixed angle of incidence α is needed. In this geometry, $\Delta\vec{k}$ changes its direction during the measurement. The traveled path length l represents the distance traveled by the X-ray through the material. Furthermore l is strongly depending on α, which makes a qualitative and non-destructive depth profiling measurement possible. The intensity of the incoming X-ray beam I_0 is attenuated by the Lambert Beer law with the material-specific attenuation coefficient μ (see equation 3.7) [21].

$$I(l) = I_0 \cdot \exp(-\mu \cdot l) \tag{3.7}$$

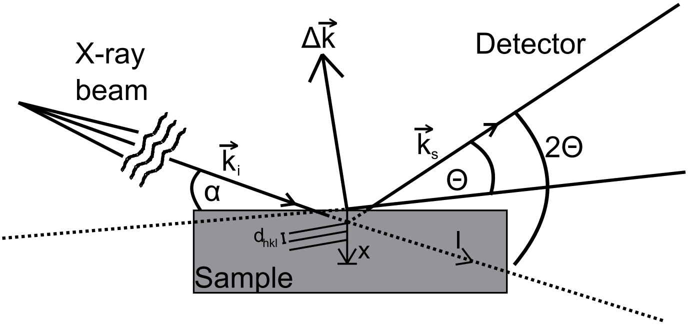

Figure 3.3: The grazing incidence (GI) geometry makes it possible to characterize the thin film over a depth determined by setting the incident angle α of the incident X-ray beam, which influences l and x respectively. In contrast to the Bragg Brentano geometry, $\Delta\vec{k}$ changes its orientation with θ.

During the interaction between X-rays and material only the e^- act as scattering centers and therefore μ depends on the density of e^-. In consequence it depends on the specific element and its atom density [29]. Furthermore the material and radiation dependent μ can be expressed by the mass absorption coefficient μ/ρ, which is only a characteristic value for the element itself leading to the extended Lambert Beer law (see equation 3.8).

$$I(l) = I_0 \cdot \exp(-(\mu/\rho)\rho \cdot l) \tag{3.8}$$

For a given incident angle α there are specific reflection angles 2θ according to equation 3.5 which lead to the traveled path length l inside the material. For a symmetric $\theta - 2\theta$ scan, l can be calculated by $x/l = sin(\theta)$ and for an asymmetric GIXRD both angle positions α and 2θ have to be considered by $l = x\left(\frac{1}{sin(\alpha)} + \frac{1}{sin(2\theta-\alpha)}\right)$ [21]. The penetration depth x along the surface normal can be extracted by using equation 3.9 for the symmetric and equation 3.10 for the asymmetric GIXRD, which takes into account the trigonometrical relationship between l and x as well as the extended Lambert Beer law (see equation 3.8).

$$x = -\frac{sin(\theta)}{\left(\frac{\mu}{\rho}\right)\rho} \ln\left(\frac{I(l)}{I(0)}\right), \; I(l)/I(0) = 1/16 \tag{3.9}$$

$$x = -\frac{1}{\frac{1}{sin(\alpha)} + \frac{1}{sin(2\theta-\alpha)}} \cdot \frac{1}{\left(\frac{\mu}{\rho}\right)\rho} \ln\left(\frac{I(l)}{I(0)}\right), \; I(l)/I(0) = 1/16 \tag{3.10}$$

The three characteristic reflection angles are used as input parameters for 2θ values in order to calculate the penetration depth x when $I(l)$ decreases by a factor of 1/16. The fixed $2\theta_{112} = 26.95\,°$, $2\theta_{220/204} = 44.73\,°$ and $2\theta_{312/116} = 52.95\,°$ values are especially used in order to calculate penetration depth for typically used α values in this thesis in the table 3.1.

In-situ XRD (IXRD) investigations: With the help of IXRD, time and temperature resolved measurements are possible, which gives an insight into the thin film growth mechanism and deeper understanding of diffusion processes in the context of Ga/In and S post-treatments. Nevertheless, a setup with a well defined and temperature-stable reaction chamber is required. X-rays can pass through the reaction chamber due to X-ray transparent polyamide windows and the scattered radiation should be collected by position-sensitive detectors, which ensures fast detection. The detector system consists of 3 individual semiconductor line detectors collecting a 2θ angle range of 12 ° per detector. This makes the analysis

Table 3.1: Penetration depth of X-ray beams into the thin film material, which decreased in intensity $I(l)$ to a factor of 1/16 depending on different incident angles α. The calculated x are performed for all the main reflections 112, 220/204 and 312/116.

α (°)	$2\theta_{112} = 26.95\,°$ x (μ**m**)	$2\theta_{220/204} = 44.73\,°$ x (μ**m**)	$2\theta_{312/116} = 52.95\,°$ (x (μ**m**))
0.2	0.13	0.13	0.13
0.4	0.27	0.27	0.27
0.7	0.46	0.47	0.47
1	0.65	0.66	0.66
2	1.26	1.29	1.3
12	5.53	6.23	6.4

of a wide angle regime possible and allows direct tracking of the thin film properties during growth.

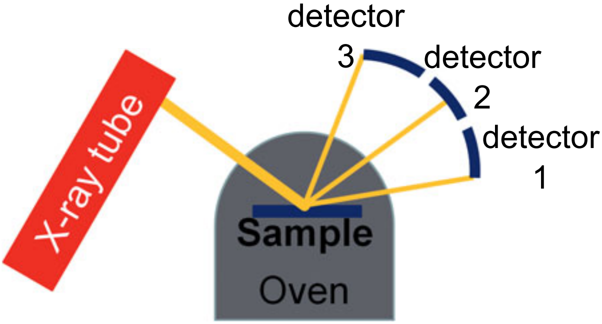

Figure 3.4: Schematic setup of the IXRD with three position sensitive detectors and an oven with X-ray transparent windows. The oven allows fast annealing ramps of up to 200 °C/min and a homogeneous temperature profile due to an arrangement of radiative heaters.

The software for IXRD data extraction is based on a peak identifier, analyzer and overview tool. The peak overview tool is very helpful for fast process and phase information of the chalcopyrite and the back contact. With the help of the literature database JCPDS the 2θ angle position, which is partially included in the software, of the corresponding reflection are used to analyze the actual measurements and the trend of shifting characteristic reflection positions. The peak identifier extracts the intensity maximum of the important reflections with a certain signal-to-noise ratio automatically in order to separate them from background noise. A Pseudo Voigt fitting procedure is performed for the individual peaks. In the peak finder tool one can manually locate the individual reflections and parameterize them with up to 3 Voigt fits. The output parameters consist of the 2θ angle position, the integral intensity, the FWHM of the peaks, and the error of the fit to the experimental data.

Scanning electron microscopy

SEM imaging is performed to depict the morphology of the thin film, either in cross-sections or in plane views. The e^- are emitted from a metal cathode with applying a sufficient extraction voltage. The acceleration voltage brings the e^- on the desired energy. The primary e^- (PE) are focused on the sample with a combination of condenser and objective lenses. The scanning mode over the sample surface is enabled by deflector coils. In general, the SEM image originates from the interaction of PE with the sample, which results in elastic and inelastic scattering. The image contrast can be divided into topography (roughness of the layers), material (different elements) and channeling (different crystal orientations) contrast and has to be considered in the interpretation of the SEM image. Elastic scattering describes the process where the PE are influenced by Coulomb interactions due to the ion cores, which results in little energy transfer. The e^- which are used for imaging are either secondary e^- (SE) or back scattered e^- (BSE). SE's are emitted from sample with typical energies in the region 0-50 eV. In the case of the SE mode, representing the conventional SEM mode, just the SE are collected by the detector system. A Zeiss 1530 machine with a linked energy dispersive X-ray spectroscopy (EDX) system (INCA Energy from Oxford Instruments) is used to analyze the grown thin films.

X-ray fluorescence and energy-dispersive X-ray spectroscopy

X-ray fluorescence (XRF): The basic principle of XRF consists of the excitation of atoms in the sample by a characteristic line and retardation spectrum of an X-ray tube to the emission of the characteristic X-rays (XRF). The physics behind the fluorescence emission is described by the process where an inner shell e^- (E_1) is removed by the incoming high energy radiation (in this case X-rays) and the e^- at higher energy levels (E_2) fill the holes by emitting element-specific fluorescence radiation with photon energies of $h\nu = E_2 - E_1$. The fast and non-destructive quantitative estimation of the element concentration is used for elements with the atomic number $Z \geq 5$. For the purpose of this work, a Fischerscope XDV-SSD apparatus has been used in combination with analysis software which can identify the characteristic element lines and the concentration of the elements. With the help of an absorption model, the thickness of the individual thin film layers can also be evaluated.

Energy dispersive X-ray spectroscopy: For an element-specific analysis the excitation of inner shells with incoming PE and the emission of X-rays with energies of $E = h\nu$ has been used in EDX measurements. The competition between the non-radiative Auger-e$^-$ transition, especially for elements with smaller atomic numbers, has to be considered in the EDX spectra interpretation. The position of the radiative transition is determined by Moseley's law (see equation 3.11) where a direct dependency of λ on Z is reflected.

$$\frac{1}{\lambda} = \overline{\nu} = R_\infty (Z-K)^2 \left(\frac{1}{n_1^2} - \frac{1}{n_2^2} \right) \tag{3.11}$$

$\overline{\nu}$ is the wavenumber, R_∞ the Rydberg constant , K displays the screening factor between the core and inner e$^-$ shells and n_1, n_2 symbolize both e$^-$ states. The intensity of the emitted radiation strongly depends on the PE energy and Z, where elements with lower Z have lower intensities.

Secondary ion mass spectrometry (SIMS)

SIMS is a method which analyzes the composition of a material depth-dependent. The measuring signal is based on ion currents of ions with different masses. In order to extract the analyzing ions from the surface a sputtering process with Ar$^+$-ions is performed. Ar$^+$ ions are accelerated towards the sample surface and collide with atoms out of this region. SIMS has to be performed under ultrahigh vacuum (UHV) conditions with high acceleration voltages to generate a high sputter yield. The high sensitivity of SIMS makes it preferable for trace element detection like Na and K.

Glow discharge optical emission spectroscopy (GDOES)

The big advantage of GDOES in comparison to SIMS measurement is the lower acceleration voltage used in the sputtering process. On the other hand, it has a higher detection limit than SIMS. Furthermore, a high erosion rate in the region of 1.6 $\frac{\mu m}{min}$ allows a short analysis time. At nearly optimized sputtering conditions, depth profiles with detection limits of about 5-10 ppm are possible. The setup consists of a cathode (sample) and an anode with a short distance in between. The discharge conditions are characterized by Ar pressure, voltage and current. The emitted photons as a result of the discharge are measured with the help of a spectrometer, which makes the element-specific characterization possible. The mode of a constant dc potential is sufficient for conductive samples, whereas time-variant potentials are used for non-conductive samples like thin film solar cells on glass. GDOES needs calibration standards, which makes the choice of proper reference samples important to generate a correlation between measured line intensities and element concentration. The line intensities depend on the element concentration, the sputtering rate and emission yield.

3.2.2 Electrical characterization

The challenge of electrical device characterization lies in the interpretation of the data which is often complex and regularly combined with device simulations. In order to parameterize the input data, the one- and two-diode model have been introduced. In the following, the basic principles of I-V and EQE analysis are shown, which makes it possible to evaluate the important performance parameters. Furthermore, certain loss mechanisms which affects the solar cell are described.

Current-voltage measurements

The basic method used to characterize a solar cell is the I-V curve under 1 sun illumination, from which one can extract the important device parameters η, V_{oc}, J_{sc} and FF. In this case, J of a solar cell is measured as a function of applied voltage $J = J(V)$ in standard testing conditions under illumination and in the dark. At standard conditions, the sample temperature is constant at 25 °C under application of an AM1.5G spectrum [99]. It is a considerable challenge to generate a light source which is able to supply a spectrum comparable to the solar spectrum. During the measurement the device is contacted with a four point probe setup where the current measurement is connected in series with the load resistance while the voltage measurement requires two separate probes [21].

Quantum efficiency (QE) measurements

Internal quantum efficiency (IQE) and external quantum efficiency (EQE) measurements are another key tools to characterize solar cells, which directly measures the ability of the absorber to collect photons and convert them into charge carriers. EQE(λ) or EQE(E) illustrates the number of e^- collected per incident photon according to equation 3.12.

$$EQE(E) = \frac{1}{q}\frac{dJ_{sc}(E)}{d\Phi(E)} \tag{3.12}$$

$d\Phi$(E) describes the incident differential photon flux density which reflects the number of photons in the energy interval dE [4]. In the case of an ideal solar cell every photon with a sufficient energy $E > E_g$ will lead to one e^-/h^+ pair [10]. This leads to a $EQE(E) = 1$ for $E \geq E_g$ and $EQE(E) = 0$ otherwise [10]. However, in real solar cells some loss processes can occur as seen before, leading to $EQE(E) < 1$ for $E \geq E_g$ because of optical and recombination losses. Reflection losses can be substracted from the raw EQE measurements with the help of an additional reflectance (R) measurement in an integrating sphere configuration. This leads to a corrected internal QE (IQE, see equation 3.13) where any kinds of photon loss by reflection are substracted [21]. Especially for a CIGSSe solar cell with its high α, all photons which are not reflected by the window layer are absorbed in the device for usual thickness of 1.5 μm [21].

$$IQE(E) = \frac{EQE}{1 - R(E)} \tag{3.13}$$

For the purpose of this research, a monochromator based setup has been used, where only a very small spot of a few millimeters in diameter of the solar cell is illuminated. The generated light needs to pass through a chopper so that a periodic signal is created, which is amplified by a lock-in amplifier. Furthermore, a reference measurement of a solar cell with a sufficiently high and well characterized EQE (in our case, a certified c-Si cell from the Fraunhofer Institute of Solar Energy (ISE)) is needed to calibrate the actual measurement of the cell of interest. For measurement values at wavelengths longer than λ_c, one has to take into account the wavelength cut-off at approximately λ_c=1127 nm of the c-Si reference cell.

CHAPTER 4

Results and discussion

CIGSSe is a promising material due to its ability to alloy the material with In and/or Ga as well as with Se and/or S, which makes it possible to introduce compositional gradients to improve the electronic properties. By introducing back and surface graded material, an attempt has been made to reduce the recombination velocity of charge carriers and also to generate a better adjustment on the solar spectrum (already introduced in chapter 2.2.4). Therefore chapters 4.1 and 4.2 discuss Ga and S gradients in order to clarify their systematic formation and their impact on the device performance and chalcopyrite structure.

4.1 Modification of the Gallium profile in CIGSe

The following chapter addresses the question whether the Ga profile inside the absorber can be influenced by different driving forces in CIGSe thin films and solar cells. The motivation lies in the enhancement of the optoelectronic properties, both at the back and front surface as well as inside the bulk material. In the SEL process the Ga-rich CIGSe material for kinetic reasons agglomerates automatically next to the back contact. The Ga profile is either influenced by the chemical potential (driving force) or the kinetics. The parameters of selenization temperature (T_{Se}) and Se partial pressure directly influence the chemical potential; however, also the kinetics are influenced by T_{Se}. The question is now, to which degree is it possible to control these parameters within the SEL process?

4.1.1 Temperature dependent phase formation

A basic introduction into the temperature dependent CIGSe/Mo growth is needed to gain detailed informations about the CIGSe phase formation. Due to the fact that Se reacts with both layer stacks in the "aggressive" RTP process, the formation mechanism is separately discussed in order to find the optimal conditions for the pure absorber, the back contact and the interface region between the absorber and the back contact.

Cu(In,Ga)Se$_2$ phase formation ex- and in-situ

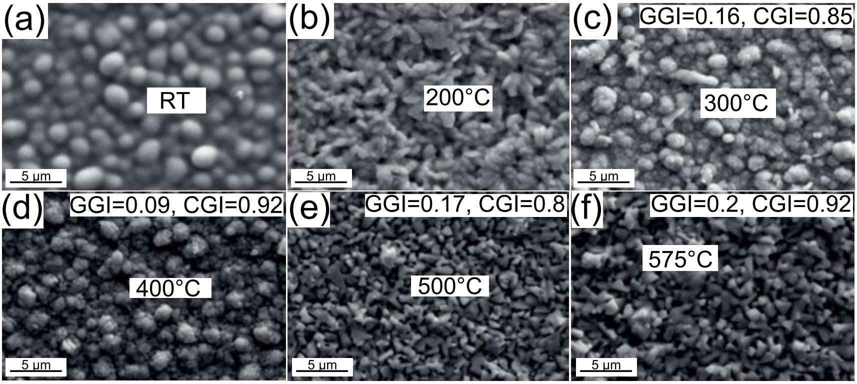

Figure 4.1: (a-f): SEM plane views of CIGSe thin films at different T_{Se} ranging from RT to 575 °C. The surface morphology changes from a ball- and flower-like surface structure towards a regular triangular shaped surface (especially for (f)). From (c-f) also the element compositions, extracted from EDX, are shown for CGI, CGI and Se/metal.

In order to analyze the phase formation of the SEL process, SEM cross sections and plane views, XRD scans and Raman scattering have been performed in the temperature range from RT to 575 °C. For the RT sample one can clearly observe the unreacted metal layers Mo, CuGa and In as well as a thick a-Se layer (see figure 4.2 (a)) with a ball-like surface structure (see figure 4.1 (a)).

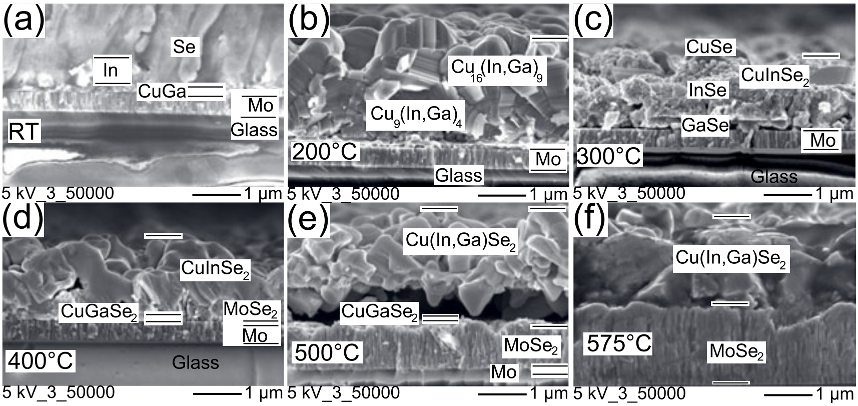

Figure 4.2: In the SEM cross sections the phase formation of the CIGSe thin film can be observed through different film thicknesses and grain morphologies. In (a) there is only a thick Se layer on the Mo back contact, whereas in (b) big grains with a comparable size are visible which belongs to the intermetallics. (c-f): Transition from small grained binary selenides (c), to CuSe rich phases (d) towards regular big CIGSe grains (e,f) are shown. Furthermore, the thickness of the back contact increases with temperatures above 400 °C according to the $MoSe_2$ growth.

The XRD and Raman analysis detect a broad amorphous region with weak crystalline In and Mo reflections (see figure 4.3 for diffraction patterns at RT), which is also underpinned by a broad amorphous mode belonging to Se (see figure 4.4, RT Raman spectra). When the process reaches temperatures around 200 °C, intermetallic compounds Cu_9In_4 and $Cu_{16}In_9$ (see figure 4.3, 200 °C diffraction pattern) are formed, which exhibit big grains (see figure 4.2 (b)). Additionally, a flower-like growth is observed on the top surface (see figure 4.1 (b)) identifying the crystallization of Se (h-Se reflections in figure 4.3, 200 °C diffraction pattern). At 300 °C the grains become smaller and porous and the surface transforms towards a nodular morphology, which originates from the CuSe (A1 mode of CuSe in figure 4.4, 300 °C Raman spectra) and In_4Se_3 growth (reflections in figure 4.3, 200 °C diffraction pattern). In this temperature range Se melting occurs around 256 °C, which represents the Se supply in the grain growth mechanism. Furthermore an A1 mode of CISe at 174 cm^{-1} as well as 112,

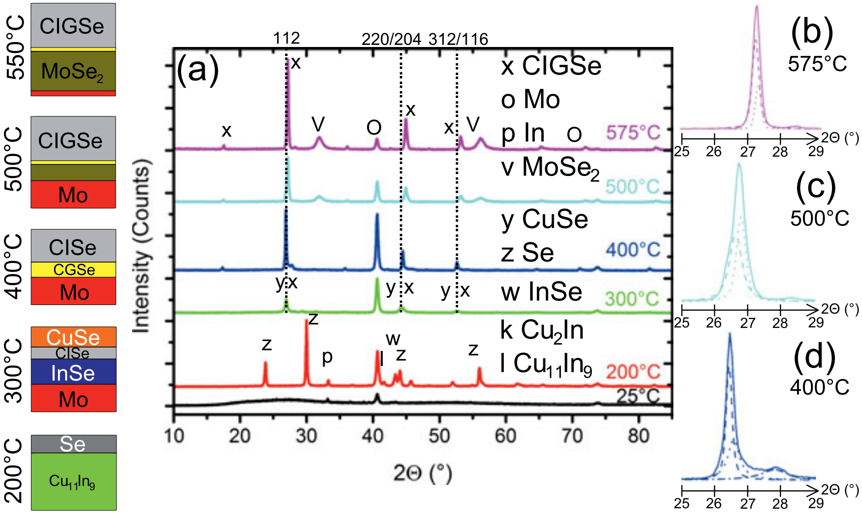

Figure 4.3: (a): XRD patterns of CIGSe thin films at different temperatures for the qualitative phase analysis of the bulk material. Between 200 °C to 300 °C the binary selenide formation takes place. (b-d): Reflection profiles of the 112 CIGSe with their corresponding Voigt fits for the temperature range 400-575 °C. The growing CISe shows a higher degree of Ga incorporation from 300 °C to 575 °C due to an increasing 2θ angle shift of the high intense 112 reflection and a reduced reflection asymmetry.

220/204 and 312/116 CISe/CuSe reflections are identified, which shows CISe growth. The grain size drastically increases towards 400 °C in cross section (see figure 4.2 (d)) and from a surface perspective the nodular grains become more dense (see figure 4.1 (d)). The crystal quality and grain size are enhanced, which is detected by an increasing reflection intensity and reduction in FWHM for the 112, 220/204 and 312/116 reflection (see figure 4.3, 400 °C diffraction pattern).

At this temperature also the CISe 101 reflection is seen, which does not overlap with a CuSe reflection (so a separate analysis with XRD becomes possible). The more asymmetric peak shape, especially for the 112, symbolizes a growing CGSe phase. According to cross sections (also proven by EDX profiles), the CGSe grains (small grain sizes) are located next to the back contact [100–104]. For 500 °C to 575 °C the slight 112

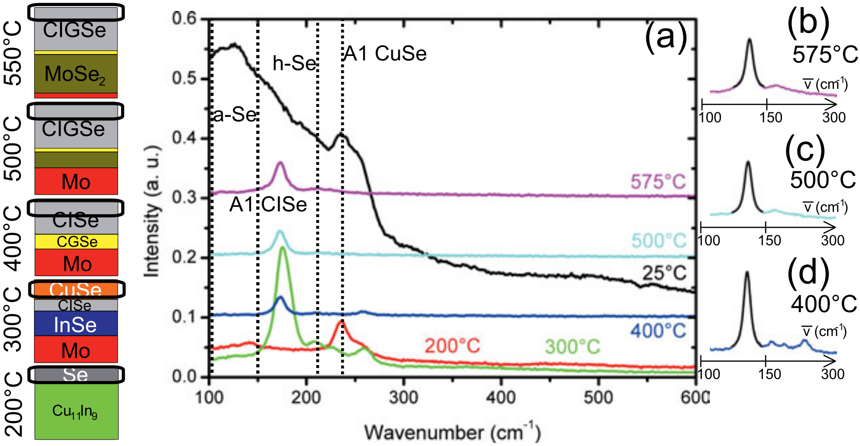

Figure 4.4: Surface sensitive Raman scattering identifies the A1 modes of CISe and CuSe at 300 °C which proves the absorber formation and the presence of CuSe near-surface. (a): The CuSe mode intensity vanishes for increasing temperatures, which reflects its consumption by the CIGSe growth path. (b-d): An overview of the CIGSe A1 mode profiles is given with their corresponding Voigt fits for the temperature regime 400-575 °C. The Raman active region is visualized by a black box on the schematic thin film compound structure for each temperature on the left side.

reflection shift to higher 2θ angles and a reduced degree of peak asymmetry indicates an enhanced Ga/In interdiffusion, which results in quaternary CIGSe grains (see figure 4.3 500 °C and 575 °C spectra). The surface structure changes significantly to triangular-shaped grains, which shows the presence of 112 orientation and furthermore gives evidence of a strong texture (see figure 4.1 (e,f)). In the cross section, the CIGSe grain size and the back contact thickness increases. The increase in back contact thickness is based on a strong $MoSe_2$ growth on the interface between the absorber layer and the back contact (see figure 4.2 (d,e)). This strong $MoSe_2$ growth, especially between 500 °C to 575 °C, can also be observed by an increasing reflection intensity of the $10\bar{1}0$ and $11\bar{2}0$ $MoSe_2$ and a reduced Mo 110 reflection intensity (see figure 4.3, 500 °C and 575 °C patterns). The information about the crystal structure and grain morphology at the end of each step of the process for different temperatures is very helpful in understanding basic material properties but in-situ analysis is needed to optimize crystal formation processes. First of all, a pure precursor without any Se supply is annealed under N_2 for 1 h at 300 °C. 300 °C is chosen because the ex-situ analysis showed that in between 200-300 °C the binary selenides start to grow after the Se melting point is reached. In figure 4.5 (a), time-dependent reflection patterns for three detectors in the 2θ range $14\,^\circ - 29\,^\circ$ (detector 1), $31\,^\circ - 46\,^\circ$ (detector 2) and $50\,^\circ - 65\,^\circ$ (detector 3) are shown. For temperatures above approximately 150 °C, the In reflections disappear because the In melting point is reached (see figure 4.5 (b)).

The intermetallic compound $Cu_{16}(In,Ga)_9$ starts to grow by alloying the precusor metals CuGa and In and later $Cu_9(In,Ga)_4$ is formed as an additional phase. With increasing annealing time the $Cu_9(In,Ga)_4$ reflection becomes more pronounced, which indicates a shifting compound ratio towards $Cu_9(In,Ga)_4$ rich phases by the slow consumption of $Cu_{16}(In,Ga)_9$ at this temperature regime (see figure 4.6 (b)). In the case of the in-situ annealing of the SEL all the ex-situ determined phase transitions were also detected (see figure 4.6 (a)), like the crystallization of Se at approximately 150 °C. Furthermore, the growth of the intermetallic compounds (comparable to the pure precursor), the transition to the binary selenides leading to the CISe grains and at higher temperatures the CGSe grains are observed. Additionally an enhanced Ga/In interdiffusion in the CIGSe growth is noticed. The interdiffusion process is observed according to a shift of the low intense 112 reflection to lower angles and a shift of the high intense 112 reflection to higher angles, which corresponds to CGSe and CISe related material (see figure 4.6 (b)).

The CE process predicts a growth path over a Cu-rich regime, which is always beneficial in terms of recrystallization and grain size (see chapter 3.1). To apply a similar situation in the SEL process, the linear heating ramp is modified to a two-step selenization process, where the temperature is kept at 300 °C for 20 min in the first step to achieve a CuSe/CISe film in order to modify the growth conditions. The transition region (binary selenides -> chalcopyrites) is extended (see figure 4.7 (a)) in order to support grain growth over the intermetallic compound $Cu_9(In,Ga)_4$ and the CuSe phase (see figure 4.7 (b)), also identified via ex-situ analysis

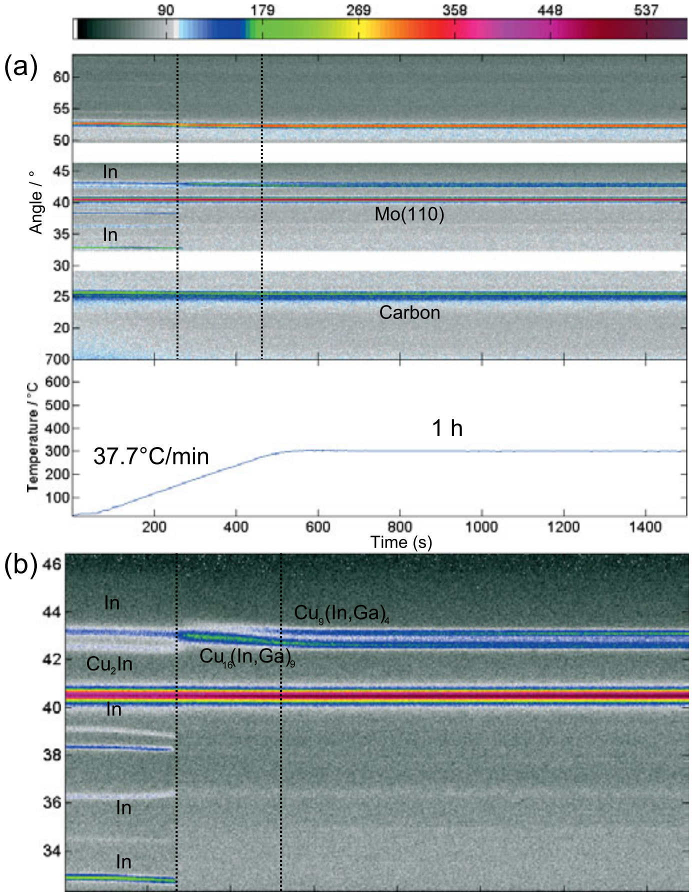

Figure 4.5: In-situ XRD analysis of a pure CuGa and In precursor layer annealed under N_2 for 1 h at 300 °C. (a): The time dependent color coded reflection profile for In, CuGa and their alloys are shown for the three different detector angles. (b): Zoom into the angle range of detector 2, where the most important reflections of In, $Cu_{19}(In,Ga)_9$ and $Cu_9(In,Ga)_4$ are located. In the angular range in between $2\theta = 42 - 44\,°$ a phase transition from In, CuGa to $Cu_{16}(In,Ga)_9$ and $Cu_9(In,Ga)_4$ is observed from changing reflection intensities.

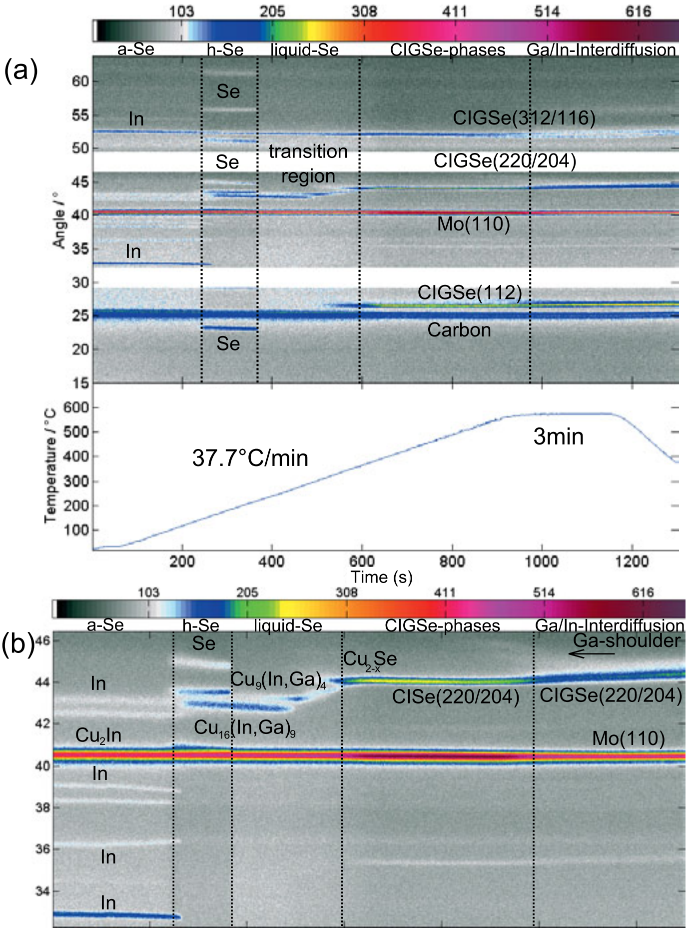

Figure 4.6: (a): In-situ XRD analysis of the SEL process with a linear heating ramp, showing the most important reflections of Mo, In, Se, intermetallic compounds, binary selenides and CIGSe. (b): Zoom into the angle range of detector 2 with the transition region from the intermetallic compounds to the binary selenides and the finally growing CIGSe.

(according to figures 4.3, 4.4, 300 °C data). However, as a result, the degree of Ga/In interdiffusion is reduced in contrast to the conventional procedure. This can originate from a lower Se partial pressure at the maximum process temperature due to an increased Se consumption (losses) over the longer process time. Additionally, CISe is the preferential growth path in the temperature regime around 300 °C and therefore the development of the CISe rich grains is strongly favored in comparison to the CGSe rich grains.

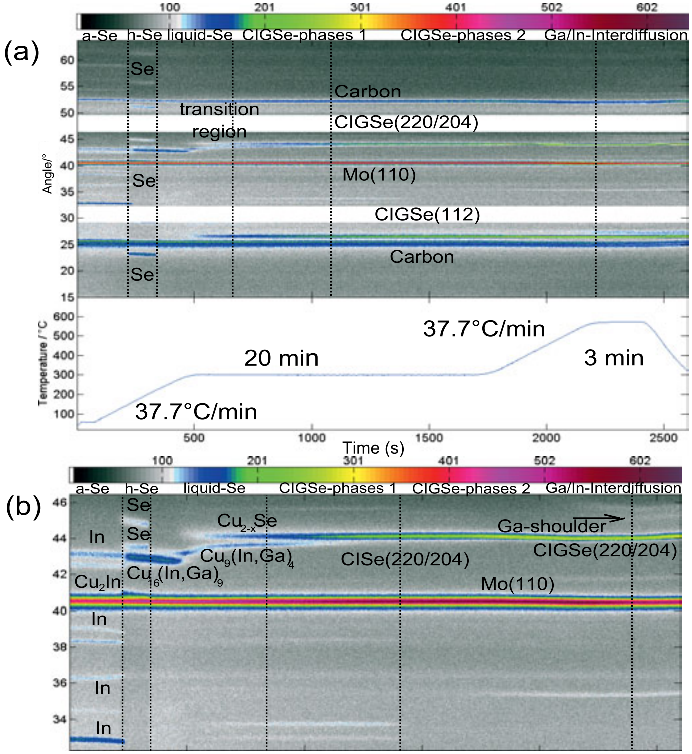

Figure 4.7: (a): In-situ XRD analysis of the SEL process with a two plateau heating ramp at 300 °C and 575 °C. (b): Zoom into the angle range of detector 2, which deals with the extended transition region.

However, by observing the solar cell performance parameters of these absorber structures the desired improvements could not be reached in the thesis (not shown). Especially, for the V_{oc} and FF lower values are determined in comparison to solar cells with absorbers produced by standard linear heating profiles. One explanation can be that the Se supply over the whole selenization process has not been sufficient due to long heating time at lower process temperature (300 °C and 400 °C) and not infinite Se source. Therefore the procedure of adding additional plateaus (300 °C or 400 °C) is only beneficial for an improved grain size and will not be further pursued in the thesis. In figure 4.8 and 4.9 the SEM cross sections are shown for the different plateaus and for different Se amounts ranging from 1 μm to 3 μm. Furthermore, the element ratios GGI and CGI are analyzed for each absorber via XRF. Strong MoSe$_2$ growth is seen for Se amounts around 2 μm (will be discussed in chapter 4.1.3) and the connection between CIGSe to the back contact is strongly reduced. Additionally, pronounced big CIGSe grains are seen especially for almost all variants.

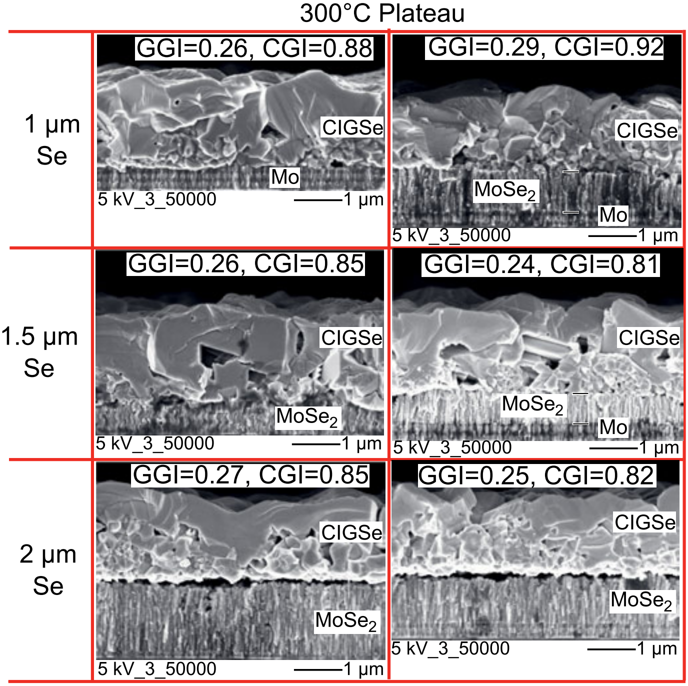

Figure 4.8: SEM cross sections of absorbers processed by 300 °C heating ramp and different Se amounts ranging from 1 μm to 2 μm. The element ratios GGI and CGI measured via XRF are additionally shown for each absorber.

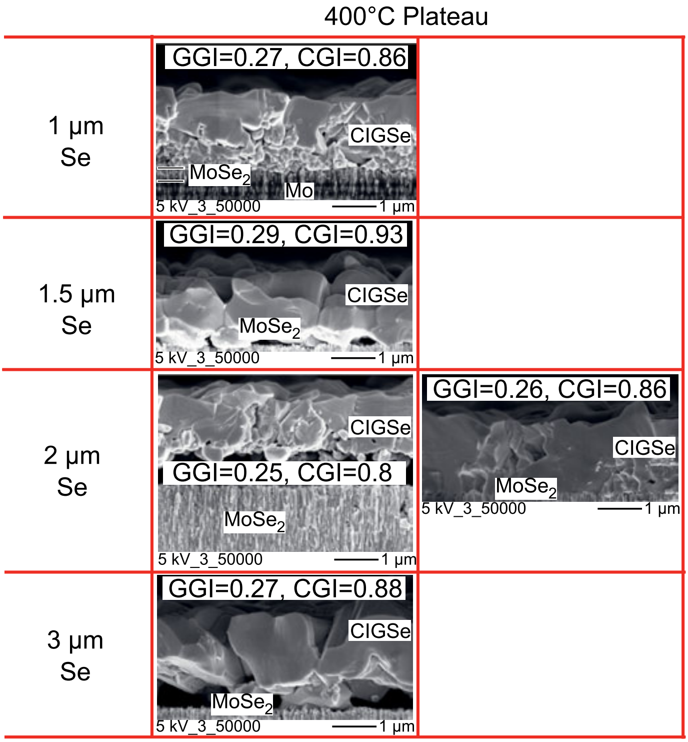

Figure 4.9: SEM cross sections of absorbers processed by a 400 °C heating ramp and different Se amounts ranging from 1 μm to 3 μm. The element ratios GGI and CGI measured via XRF are additionally shown for each absorber.

Short summary

It has been shown that during the heating of the SEL the absorber (stack) undergoes a sequence of phase formation and transformation. At higher temperatures the Ga/In interdiffusion is enhanced, which is recognized by the shift of the specific chalcopyrite reflections to higher 2θ angles. In-situ analysis via XRD is very helpful in visualising the phase formation changes of the intermetallic compounds. A two-step process with a growth over the Cu-rich regime at 300 °C leads to an improved grain size but not to beneficial solar cell performance properties.

4.1.2 Phase formation with different Selenium supply

In the following chapter, the influence of Se supply on the SEL process during the final annealing step is investigated. Most results have been already published in [13] and are reproduced with the permission of Elsevier Publishing.

Introduction

It is well known that CuSe phase acts as a flux agent on top of the CIGSe during the growth process, which leads to a desirable grain growth and a homogeneous Ga/In distribution [17, 23, 34]. In general, big grains are favorable in terms of reduced charge carrier recombinations at grain boundaries. Nevertheless, this CIGSe structure can lead to the formation of shunt paths caused by the highly conductive CuSe phase. Therefore, alternative concepts to obtain flat Ga/In profiles are of interest, like a Se post-treatment approach [105]. Another approach is via the formation of a liquid Se-phase above the CIGSe thin film, which promotes the Ga/In interdiffusion [106]. In this chapter, the Se dependent CIGSe phase formation is investigated in detail by conducting experiments with a varying Se supply. The main focus is on the Ga/In profiles and in particular the Ga amount near-surface since these parameters are known to have a large impact on the optoelectronic properties like the E_g and the solar cell device parameters. The experimental results are compared with numerical modeling results of the cells derived from SCAPS simulations, which are based on the actual concentration profile of the individual absorbers.

Structural investigation of the thin film

In figure 4.10, an overview of cross sections of the individual layers of the CIGSe structures obtained for different Se amount are shown. Furthermore qualitative EDX analysis of the different layers are shown for different spectra in table 4.1 (Spectrum 1: back contact/glass, Spectrum 2: absorber back side/back contact, Spectrum 3: absorber intermediate/absorber back side, Spectrum 4: absorber top/absorber intermediate region). In figure 4.10 (a,b) one can observe a strong structural difference in the grain size of the CIGSe between 0.5 μm and 1 μm Se. This can be explained by the Cu-In-Se phase diagram [107], which predicts a CuSe phase for slightly Se-poor compounds during growth [108]. Bigger grains in the CIGSe thin films (see figure 4.10) are found for higher CGI ratios (see table 4.2).

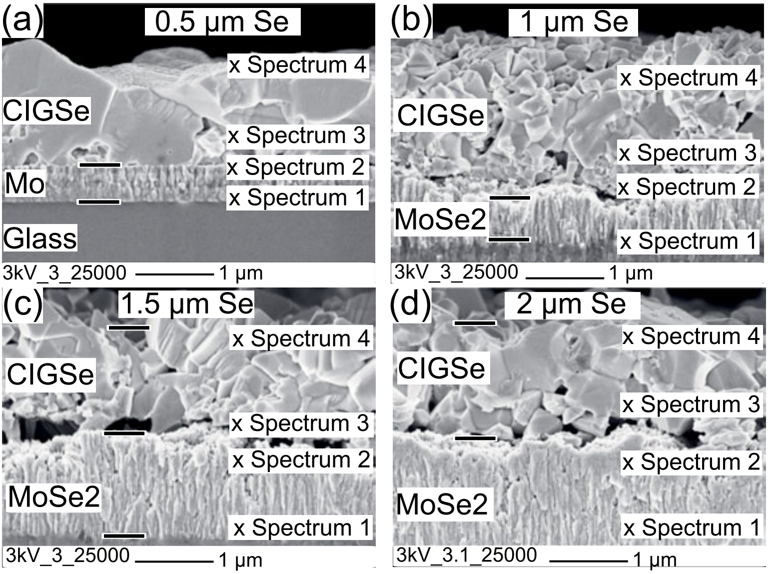

Figure 4.10: SEM cross sections for different Se film thickness ranging from 0.5 μm (a) to 2 μm (d). The crosses at the thin film indicate the region of EDX analysis, which is written as Spectrum 1, Spectrum 2, Spectrum 3 and Spectrum 4. The EDX results are given in table 4.1 (reproduced from [13] with permission of Elsevier Publishing).

The GGI measures the group III element ratio which has a strong influence on the E_g value (see table 4.2). Additionally, $MoSe_2$ formation is identified at the back contact by the presence of a weak contrast difference between Mo and $MoSe_2$ grains, which is also marked in the SEM cross sections (see figure 4.10 (b-d)). This can also be quantified with an increased Se/metal (Se/Mo) ratio obtained by XRF (see table 4.2) and EDX (see table 4.1, Spectrum 1) measurements. The red lines in the SEM images visualize thicknesses of CIGSe and back contact of the Mo/$MoSe_2$ and CIGSe layers. For the 0.5 μm Se sample high bulk values for GGI and CGI are observed. They most likely originate from In loss, which is caused

Table 4.1: Evaluated Se/Mo, GGI, CGI and Se/metal ratios from EDX spectra of CIGSe/Mo films processed with different Se amounts (see figure 4.10). The different measurement points on the thin film are Spectrum 1 (back contact/glass), Spectrum 2 (absorber back side/back contact), Spectrum 3 (absorber intermediate/absorber back side) and Spectrum 4 (absorber top/ absorber intermediate region).

0.5 μm	**Se/Mo**	**GGI**	**CGI**	**Se/metal**
Spectrum 1	0.07	0.7	0.5	0.6
Spectrum 2	0.61	0.86	0.69	0.88
Spectrum 3	6.29	0.68	1.03	1.17
Spectrum 4	29.33	0.21	1.58	1.42
1 μm	**Se/Mo**	**GGI**	**CGI**	**Se/metal**
Spectrum 1	0.12	0.67	0.5	1
Spectrum 2	3.34	0.78	0.78	7.31
Spectrum 3	11.43	0.76	0.85	1.31
Spectrum 4	35	0.25	1.75	1.59
1.5 μm	**Se/Mo**	**GGI**	**CGI**	**Se/metal**
Spectrum 1	0.2	0.71	0.57	1.73
Spectrum 2	3.61	0.78	0.67	8.67
Spectrum 3	12.25	0.4	1.65	1.85
Spectrum 4	31.67	0.55	0.95	1.28
2 μm	**Se/Mo**	**GGI**	**CGI**	**Se/metal**
Spectra 1	3.47	0.71	0.43	13.2
Spectra 2	3.62	0.75	0.75	8.79
Spectra 3	21.25	0.53	1	1.42
Spectra 4	36	0.39	1.3	1.36

by volatile In_2Se formation during the process [109, 110]. This behavior is frequently observed for an insufficient supply of Se (Se partial pressure) in the SEL process during the chalcopyrite formation.

For detailed investigation of the Ga/In depth profiles, GDOES measurements are performed. In figure 4.11, the ratio of emission intensity (EI) of Ga over the sum of the intensities of Ga and In is plotted vs. depth for different Se amounts supplied. Due to the lack of suitable calibration samples, these ratios may differ slightly from actual GGI ratios; however, the trends are reproduced well. An increasing Se supply results in smoother Ga/In profiles through the CIGSe sample and an enhanced Ga amount next to the surface. However, the integral Ga/In ratio stays the same

Table 4.2: GGI, CGI and Se/metal ratios of the CIGSe thin films determined via XRF for different Se film thicknesses, ranging from 0.5 μm towards 2 μm.

Se amount (μm)	GGI ratio	CGI ratio	Se/metal ratio
0.5	0.3 ± 0.01	0.98 ± 0.02	1.02 ± 0.027
1	0.26 ± 0.004	0.84 ± 0.01	1.77 ± 0.12
1.5	0.26 ± 0.006	0.84 ± 0.01	2.49 ± 0.18
2	0.24 ± 0.005	0.79 ± 0.008	2.6 ± 0.1

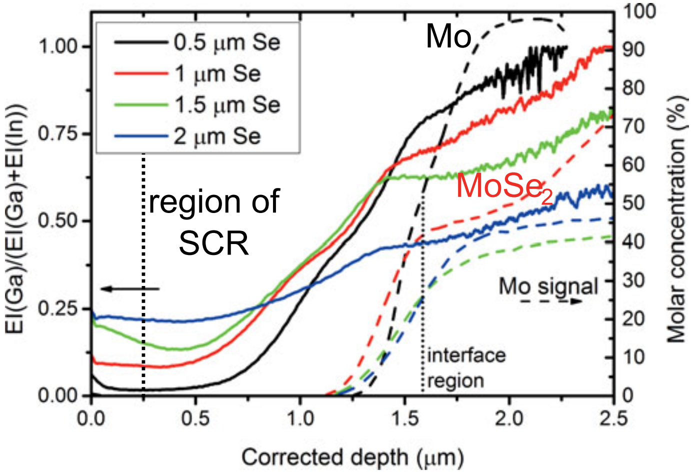

Figure 4.11: GDOES measurements showing the emission intensity (EI) ratio $EI(Ga)/(EI(Ga) + EI(In))$ ratio vs. the CIGSe depth (reproduced from [13] with permission of Elsevier Publishing).

for all the four samples. Furthermore, one can observe a constant GGI ratio at the front surface for 0.5 μm, 1 μm and 2 μm of Se, which is more pronounced with an increasing Se supply. The double grading structure in the GDOES profile for the 1.5 μm thick Se layer can originate from different surface roughness values of the absorber influencing the Ga and In emission intensity values during the GDOES analysis. Lateral inhomogeneities of the Ga distribution can furthermore impact measured Ga emission intensity ratios. Additionally, the growth process over the binary selenides $Cu_{2-x}Se$

or $CuSe_2$ (preferred for low and high Se supply) leads to different growth paths according to the Cu-In-Se phase diagram [83].

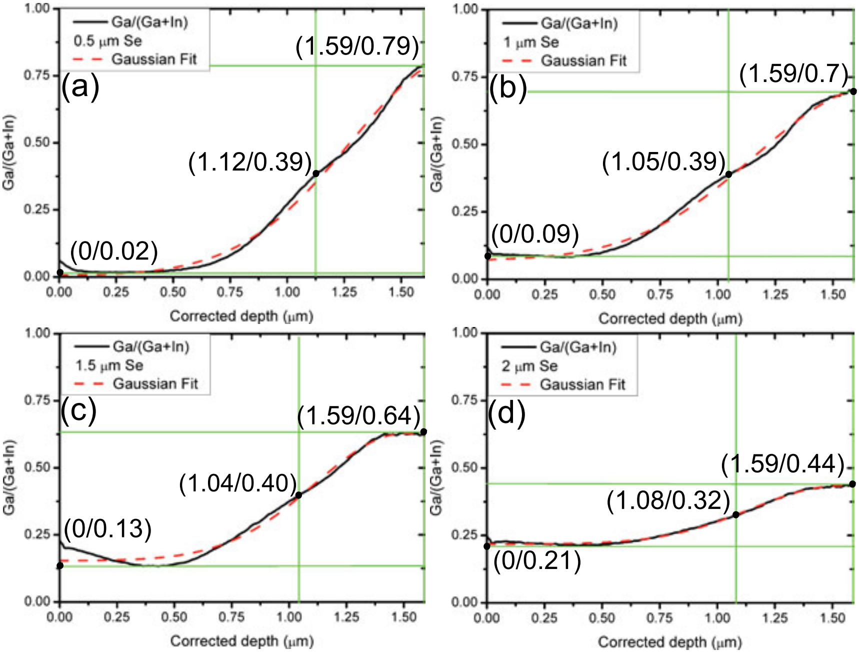

Figure 4.12: In (a-d) the GGI depth profiles (in black) from GDOES measurements are shown for different CIGSe thin films which were processed with different Se amounts ranging from 0.5 μm to 2 μm. The red dotted lines symbolize the fitted Gaussian error functions. The black dots on each profile stand for the characteristic regions near-surface, intermediate and back surface (reproduced from [13] with permission of Elsevier Publishing).

In figure 4.12, experimental Ga/In profiles for different Se amounts are fitted with a Gaussian error function. In the CIGSe system, the interdiffusion of Ga into CISe and In into CGSe are the relevant processes and therefore the determined diffusion coefficients (D) are mean values of D^{Ga}_{CISe} and D^{In}_{CGSe}, respectively. Equation 2.10 gives the well-known solution of the interdiffusion problem. Here, $c(x,t)$ is the concentration profile where c represents the GGI ratio, and erfc is the complementary Gaussian error function (see figure 4.12). c_2 and c_1 are the minimum and maximum concentration respectively in the diffusion area. The values of

Table 4.3: Overview of the D values for different Se amounts evaluated from the concentration profiles in comparison to literature values.

Se amount (μm)	$D (cm^2/s)$	$D^{lit}(cm^2/s)$ **[104, 111]**
0.5	3.32E-12	4.5E-11
1	3.44E-12	"
1.5	3.55E-12	"
2	3.9E-12	"

$erfc[x]$ are taken from [39]. In table 4.3, the values of D obtained in this way are listed for the different Se amounts. A value of 4.5 E-11 $\frac{cm^2}{s}$ for 575 °C selenization temperature [104, 111] serves as the reference value, as all the processes in this chapter are performed at 575 °C. Furthermore, the interdiffusion between the pure CISe film and a Ga layer was investigated in [111], which is slightly different from the system studied here. The different starting configurations can be seen as the reason for the one magnitude higher D value in [111]. Additionally, the experimental data show a weak dependency on the Se supply within the error of the measurement (see table 4.3).

In order to obtain more detailed information about the CIGSe phase formation, XRD investigation is used (see figure 4.13 (a)). In general, a peak shift to higher 2θ angles corresponds to higher Ga concentration in the CIGSe grains because of the smaller covalent radius of Ga in comparison to In. An asymmetric reflection shape is observed, which indicates a Ga/In concentration gradient over the CIGSe thickness [12]. In comparison to the GDOES results, the gradient, as detected from the reflection shape in XRD, decreases with an increasing Se amount. The 112 reflection profile shows a more asymmetric reflection shape for the 1-1.5 μm Se samples. The XRD peaks are analyzed with the help of 2-3 Voigt fits (see figure 4.13 (b-e)), which represent the In-rich (CISe), the Ga-rich part (CGSe) [11] and the intermediate region of the absorber layer. The CISe 112 reflection (between $2\theta = 26.8\,°$ and $2\theta = 26.83\,°$) and the CGSe 112 reflection at $2\theta = 27.31\,°$ (see figure 4.13 and table 4.4) are determined by a fitting procedure. The cumulative fit position describes the weighted average of 2-3 Voigt fits used to approximate the reflection shape. In order to obtain

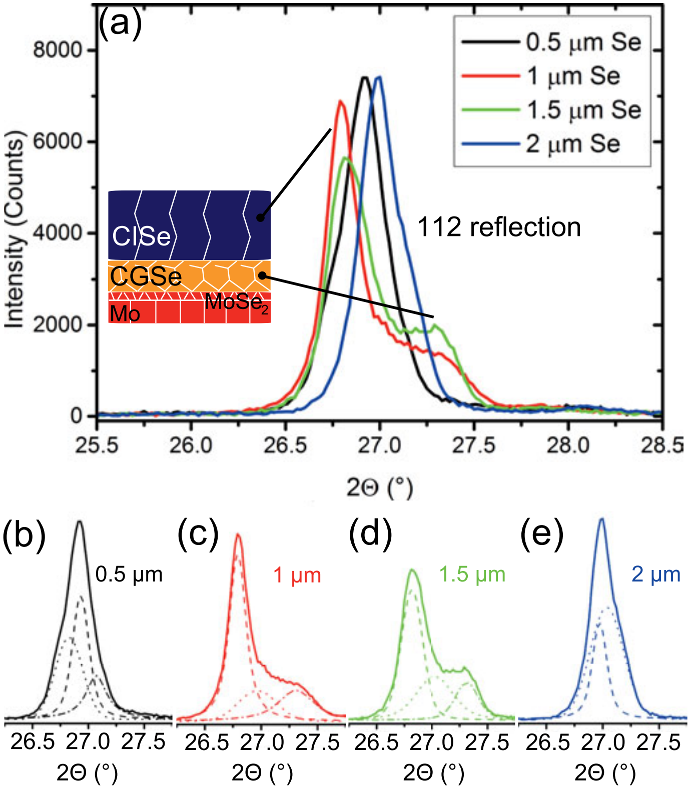

Figure 4.13: (a): XRD pattern in the region of the CIGSe 112 reflection for varying Se amounts. (b-e): The respective 112 reflection profiles are shown together with the individual Voigt profiles used in the fitting procedure (reproduced from [13] with permission of Elsevier Publishing).

a more quantitative measure for the degree of grading (see table 4.4), the difference in the 2θ angle positions between Fit 1 (CISe-like) and Fit 3 (CGSe-like) can be used as given by equation 4.1.

$$|2\theta_{112}^{Fit\ 1} - 2\theta_{112}^{Fit\ 3}| = \Delta 2\theta_{112}^{grad} \tag{4.1}$$

When the difference $\Delta 2\theta_{112}^{grad}$ (according to equation 4.1) becomes smaller, it is taken as an indication for an increased Ga interdiffusion into CISe-like grains. With the help of the Cumulative Fit it is possible to determine the integral GGI ratio (see table 4.4) according to the Bragg equation where the interplanar distance d_{112} is evaluated for a $2\theta_{112}$ angle position. For the tetragonal crystal system CIGSe with orthogonal crystallographic axis [26], d_{112} can be expressed by the lattice constant a and c according to equation 4.2 [26]. The lattice constants a and c change with respect to the GGI ratio x in the CIGSe film according to Vegard's law (see equation 4.3), which is identified via XRD analysis according to the $2\theta_{112}$ angle position and the calculation via the Bragg equation.

$$d_{hkl} = \frac{1}{\sqrt{(h/a)^2 + (k/b)^2 + (l/c)^2}}, \ d_{112} = \frac{1}{\sqrt{2/a^2 + 4/c^2}} \tag{4.2}$$

$$a = x \cdot a_{CGSe} + (1-x) \cdot a_{CISe}, \ x = \frac{Ga}{Ga + In} \tag{4.3}$$

For the 0.5 μm and 2 μm Se sample, one can find a quasi-single phase 112 CIGSe reflection corresponding to the $\mathit{\Delta} 2\theta_{112}^{grad}$ values of 0.14 ° and 0.07 °, which indicates a more homogeneous material (see figure 4.13 (a)). A high Se amount (2 μm) leads to a more homogeneous Ga/In distribution inside the CIGSe material, as evidenced from the low value of the degree of grading for this condition. A low 2θ angle difference for the 0.5 μm sample can be observed. However, in this case the quasi-single 112 reflection can also result from the formation of CuSe, which leads to a CuSe 111 reflection having a lattice spacing similar to the 112 CIGSe reflection. Additionally,

Table 4.4: Degree of grading (evaluated by the difference of the Voigt Fits 1 and 3, see main text). Cumulative Fit position (weighted average of the positions of the individual fitted peak positions) and GGI ratios evaluated from the cumulative reflection position according to Vegard's law and the 2θ angle position.

Se amount (μ**m**)	**Degree of grading** (°)	**Cumulative** (°)	**GGI**
0.5	0.14	26.83	0.28
1	0.52	26.97	0.17
1.5	0.49	27.02	0.19
2	0.07	27.04	0.34

a relatively strong (112) texture is identified by determining the reflection intensity ratios I_{112}/I_{220}, I_{112}/I_{312} and I_{112}/I_{101} respectively (see table 4.5). For the I_{112}/I_{220} ratio values around 3, for the I_{112}/I_{312} ratio values around 8 and for the I_{112}/I_{101} ratio values around 20 can be calculated. However, for all three ratios higher values than the reference CISe powder data are identified.

For a better insight into surface properties, especially the surface GGI ratio, which is very important for the p-n junction formation to the buffer layer of the complete solar cell device, surface sensitive Raman scattering is performed. The results are shown in figure 4.14. For the 0.5 μm Se sample, no CuSe A1 mode is found at 260 cm^{-1}, which indicates the absence of a CuSe layer at the surface. With increasing Se supply from 1 μm to 2 μm, the expected CIGSe A1 mode shift to higher energies is observed (see inset of figure 4.14). In general, one observes a linear correlation between Raman shift ($= y$) and Ga incorporation ($GGI = x$), which is widely used in the CIGSe community for determination of the GGI (see equation 4.4). However, strain effects can also play a role for example due to surface reconstructions, which is indicated by the presence of the ordered defect compound (ODC) $CuIn_3Se_5$ (preferable for Cu-poor compounds).

$$\frac{y - 173\ cm^{-1}}{m} = x,\ \ m = 184\ cm^{-1} - 173\ cm^{-1} \tag{4.4}$$

Table 4.5: Overview about the reflection intensity ratios of 112/220, 112/312 and 112/101 in order to determine the grain texture for different Se supply, also in comparison to CISe (JCPDS 00-035-1100) and CGSe (JCPDS 00-040-1487) powder values.

Se amount (μm)	I_{112}/I_{220}	I_{112}/I_{312}	I_{112}/I_{101}
0.5	3.45	8.84	25.29
1	2.9	7.36	22.83
1.5	3.38	8.52	18.07
2	2.87	7.2	20.35
Powder$_{CISe}$	1.96	4	16.67
Powder$_{CGSe}$	4	3.33	100

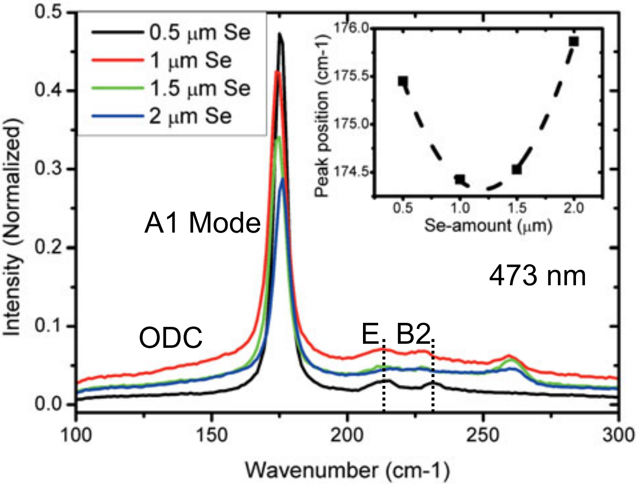

Figure 4.14: Raman spectra in the region of the CIGSe A1, E and B2 mode position showing the presence of the ODC shoulder mode. The inset shows the A1 mode position vs. the Se amount.

The PL spectra in figure 4.15 show intensive peaks in the region of 1.02-1.08 eV, which correspond to a quasi band-to-band transition. The peaks are fitted using two Voigts profiles to determine the average E_g position. For the 1.5 μm Se sample, the highest PL peak intensity is observed, which indicates a high degree of radiative over non-radiative recombinations. Generally, a higher PL peak intensity corresponds to a lower defect density [24]. A shift of the PL peak to higher energies, from an In-rich towards an intermediate Ga material according to the E_g increase in the inset of figure 4.15, is a hint for a more homogeneous Ga incorporation into the intermediate region of the CIGSe absorber layer. The analysis of the PL peak position also supports the conclusion from XRD and Raman with respect to the Ga/In interdiffusion.

Electronic properties of the solar cell

The CIGSe absorbers were processed to complete solar cell devices by the ZSW standard recipe with a sequential deposition of 50 nm CdS via chemical bath deposition, 50 nm i-ZnO via radio frequency sputtering and

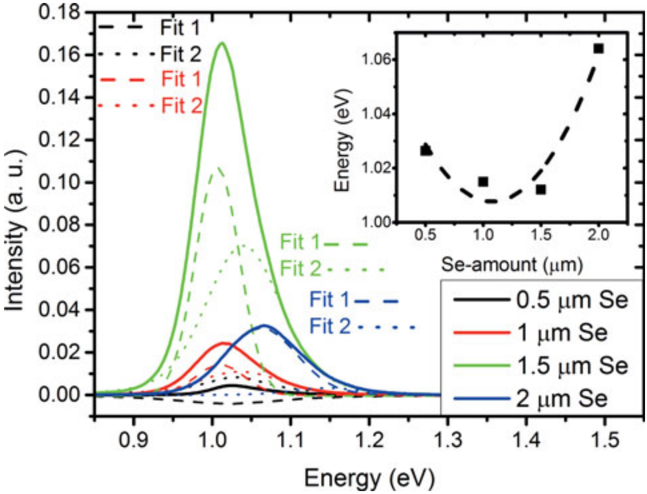

Figure 4.15: PL spectra vs. energy which corresponds to the band-to-band transition for CIGSe. The inset shows the trend of the peak maxima vs. Se supply. The corresponding GGI or x values are calculated by equation 4.5 (reproduced from [13] with permission of Elsevier Publishing).

400 nm ZnO:Al (AZO) via direct current sputtering. In a final step, a Ni/Al contact grid is grown on the AZO by electron beam deposition. The I-V curve is strongly influenced by the R_s, which is determined by modeling the measured I-V curves using the one diode model according to chapter 2.2.3 or along the following publications [50,51,112]. With the help of EQE measurements it is possible to investigate the wavelength dependent charge carrier collection efficiency of the CIGSe device and to identify possible losses. Photon absorption in the ZnO layer shows up in the region from the ultra-violet to 380 nm, and within the region from 380 to 520 nm absorption in the CdS buffer takes place (see chapter 2.2). From the region between 520 nm and 1200 nm the CIGSe absorber quality can be assessed [112]. Additionally, reflectance and transmittance measurements on the devices are performed via halogene lamps in an integrating sphere configuration (Ulbricht sphere) to determine the internal quantum efficiency (IQE), which reflects only the internal material properties (see figure 4.16 (a)). By

comparing the three samples (0.5-1.5 μm Se) one can observe an increase of the IQE with an increasing Se supply while maintaining nearly identical spectral shapes [113]. This shows an enhanced CIGSe absorber layer quality with an increasing Se supply, which is in accordance with the PL intensity evolution of the thin film as discussed above. In order to evaluate the E_g value, one can treat the IQE as an absorption curve and use the well-known relation for the dependence of the absorption on photon energy E for direct semiconductors [24] by plotting $\left[E \cdot ln\left(\frac{1-IQE}{100}\right)\right]^2 (eV)^2$ vs. E [113] (see figure 4.16 (b)). It has been found that CIGSe absorbers produced with 2 μm Se have a slightly higher E_g, which is in good agreement with the observation that there is a more homogeneous Ga/In distribution inside the CIGSe for larger Se supply. The evaluated effective E_g values for the analyzed film thickness (approximately 200 nm) lead to differently calculated GGI ratios according to equation 4.5 even though the same GGI ratio is determined by XRF in the total CIGSe film thickness (see table 4.2). This is a hint for a higher amount of Ga in the analyzed region (penetration depth of PL laser). When comparing the E_g values obtained by the different methods, one has to consider that IQE characterizes the performances of the CIGSe solar cell with respect to generation of e^-/h^+ pairs ($E_g = E_g^{min}$) whereas PL examines the absorption properties of a small part, approximately the size of the SCR, in the CIGSe layer ($E_g = E_g^{SCR}$).

The GDOES depth profiles analyze the ratio of Ga to In over the absorber depth. In order to estimate the theoretically expected E_g of a non-graded CIGSe material, one can use equation 4.5 with the bowing parameter b=0.21, which refers to the multinary composition $Cu(In_{1-x}Ga_x)Se_2$ [114]. For estimating E_g^{GDOES} just the near-surface GGI ratio serves as input parameter.

$$E_g(x) = (1-x) \cdot E_g^{CISe} + x \cdot E_g^{CGSe} - b \cdot x \cdot (1-x) \tag{4.5}$$

In this case x represents the GGI ratio evaluated by XRF or GDOES measurements (see table 4.6). The degree of grading can be estimated by comparing the differences between the E_g values obtained by PL, IQE and

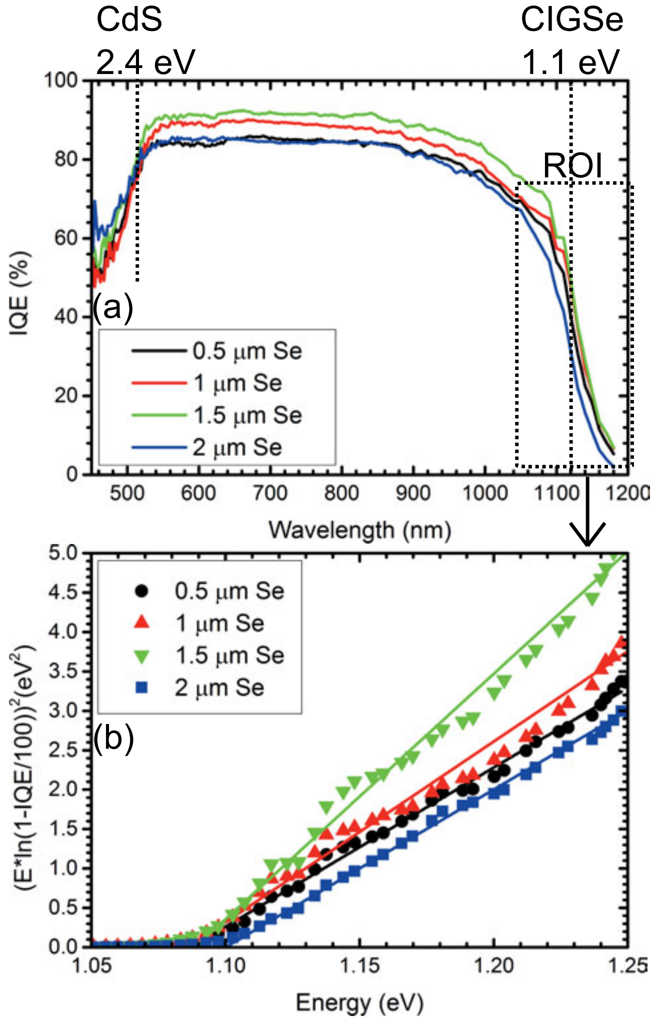

Figure 4.16: (a): IQE spectra vs. wavelength in between 450-1200 nm. The ROI indicates the absorption edge region used to calculate the E_g. (b): Plot of $\left[E \cdot ln\left(\frac{1-IQE}{100}\right)\right]^2 (eV)^2$ vs. E. The E_g is extracted from the intersection of the fitted straight lines with the energy axis (reproduced from [13] with permission of Elsevier Publishing).

XRF studies $E_g^{XRF-PL} = |E_g^{XRF} - E_g^{PL}|$ and $E_g^{XRF-IQE} = |E_g^{XRF} - E_g^{IQE}|$. E_g^{XRF} represents the E_g value calculated from GGI ratios according to XRF measurements and using equation 4.5. E_g^{PL} and E_g^{IQE} are the E_g values estimated from PL and IQE spectra. The differences between the E_g values obtained from using the different approaches are smaller for the 2 μm sample, which confirms the previously found result that this sample has a more homogeneous Ga/In distribution (see table 4.6). It seems that the E_g data determined via IQE measurements and indirectly estimated from GDOES are not consistent. The E_g^{IQE} is averaged over the total thin film solar cell, and the evaluated E_g^{IQE} values range from 1.086 eV to 1.1 eV. The values differ from expected E_g values from GDOES analyzing the CIGSe absorber. The E_g value with the help of equation 4.5 and the bowing parameter b=0.21 is varying in the range between 1.04 eV (for GGI=0) and 1.13 eV (for GGI=0.2). The GDOES depth profiles do not deliver exact GGI ratios because of the lack of calibration/normalization samples as reference.

In figure 4.17 (a) an overview of the I-V curves for different Se amounts is shown, which reflect the differences in the CIGSe absorber and back contact properties. Additionally, the plots of dark I-V data in log scale are shown together with the corresponding fits (see figure 4.17 (b-e)). There is a good agreement between fit and measured data. The one diode model fits are applied in order to evaluate the parameters for R_s, R_p, J_0 and n_{id}. A decrease of the FF with an increasing Se supply (see figure 4.18 (b)) has been found, which can either be caused by the interface of the absorber

Table 4.6: E_g values from PL, IQE, GDOES and XRF measurements on the thin film and solar cell device. An overview of E_g^{XRF-PL} and $E_g^{XRF-IQE}$ is additionally shown (see main text for discussion).

Se (**μm**)	E_g^{PL} **(eV)**	E_g^{IQE} **(eV)**	E_g^{GDOES} **(eV)**	E_g^{XRF} **(eV)**	E_g^{XRF-PL} **(eV)**	$E_g^{XRF-IQE}$ **(eV)**
0.5	1.026	1.087	1.05	1.188	0.162	0.101
1	1.015	1.086	1.09	1.165	0.15	0.079
1.5	1.012	1.089	1.1	1.166	0.154	0.077
2	1.06	1.1	1.15	1.155	0.091	0.055

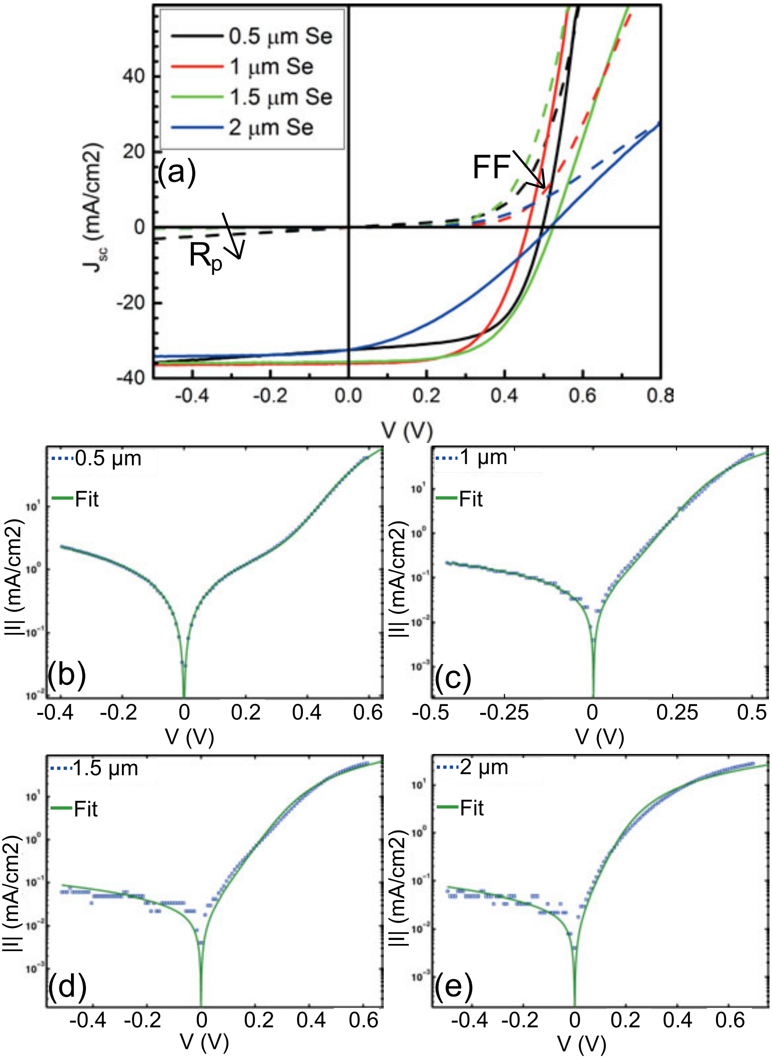

Figure 4.17: (a): The dark and illuminated I-V curves of the solar cell devices are shown on a linear scale. The regions where the Se-induced effects on the R_s and FF are most obvious, have been highlighted using arrows. (b-e): The experimental dark I-V data are separately shown on a log scale (dotted) together with the corresponding fit curves (line), according to the one diode model (reproduced from [13] with permission of Elsevier Publishing).

towards the back contact or towards the buffer [12]. In real p-n junction solar cells the theoretical maximum V_{oc} according to the SQ model cannot be reached because of (non-radiative) recombination effects [9]. In order to investigate the p-n junction properties, the R_p, n_{id} and J_0 have been calculated by fitting the experimental I-V curves using the one diode model. According to the results of the analysis, both R_s and R_p increase with an increasing Se supply (see table 4.7). The increase in R_s indicates a higher $MoSe_2$ layer thickness which affects the resistivity of the back contact system and lead to a reduction in FF and V_{oc} (see table 4.7). The decrease in R_p with an increasing Se supply indicates a decreased probability for the formation of shunt paths (see table 4.7). For the 0.5 μm sample a relatively low R_p value is found, which can be correlated to the higher CGI ratio in the absorber material. The values of J_0 and n_{id} should be handled with care due to the fact that they are fitted from dark I-V curves in the presence of high R_s values. This makes it hard to extract n_{id}, J_0 and R_s unambiguously and therefore values are subject to large errors (values are not shown in table 4.7). Furthermore, n_{id} and J_0 are coupled with the V_{oc} according to equation $V_{oc} = \frac{n_{id} k_B T}{e} \ln\left(\frac{J_{sc}}{J_0} + 1\right)$.

Figure 4.18 (a) shows the Se/metal ratio determined by XRF. It should be noted here that the XRF measures the total amount of Se in the sample and not only the amount of Se incorporated into the absorber layer. The stoichiometry line for Se/metal=1 represents the "ideal" composition of the CIGSe absorber. A deviation from this line is the consequence of a Se under- ($Se/metal < 1$) or oversupply ($Se/metal > 1$). In the latter case, the excess Se incorporates in the Mo layer and forms $MoSe_2$.

Table 4.7: R_s and R_p values for different Se supply are shown. R_s and R_p increase significantly with the Se supply.

Se (**μm**)	R_s (Ωcm^2)	R_p (Ωcm^2)
0.5	1.3	175
1	2.1	2254
1.5	3.8	6771
2	17.5	7734

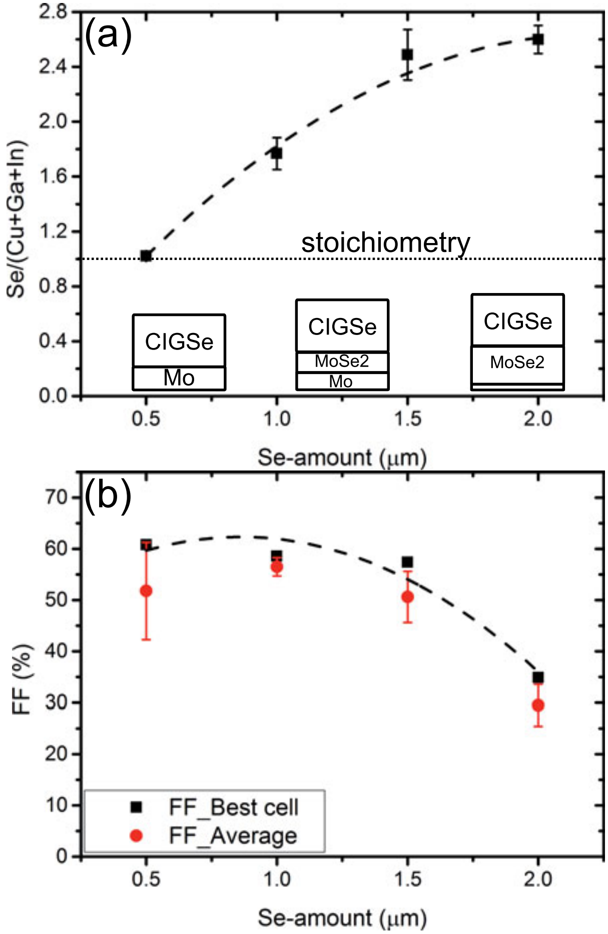

Figure 4.18: (a): Se/metal ratio as determined by XRF for the different Se supply, also visualized by the schematic SEL layer stack. (b): The *FF* of cells produced with different Se supply (black squares) as determined from I-V curves shown in figure 4.17 (a) (reproduced from [13] with permission of Elsevier Publishing).

One way to judge the quality and performance of a solar cell is to compare the cell properties with predictions made by theoretical models or numerical simulations. The SQ model provides the first approach to the limit of the performance of a solar cell under highly idealized conditions (radiative recombination limit) [10]. Here, the E_g^{IQE} values serve as input parameter for the SQ calculation because the total CIGSe solar cell is taken into account. The experimentally determined J_{sc} values from I-V measurements exhibit a parabolic trend (see figure 4.19 (a)). By comparing the experimental results with the SQ limit, it becomes obvious that the trend in the J_{sc} values cannot be explained by only taking into account the reduction of the number of absorbed photons caused by the increase of E_g. Other factors, like grain size and $MoSe_2$ layer thickness, are also strongly influenced by the Se supply and have an impact on J_{sc}.

In figure 4.19 (b), it can be observed that the experimental V_{oc} has a similar dependence on the Se supply as predicted by the SQ model, which can be attributed to the E_g dependence in the SCR of the solar cell device on the Se content. SCAPS simulations have been performed using the experimentally determined GGI profiles from the GDOES measurements (see figure 4.11). Furthermore the input of absorption profiles [63] of the CIGSe absorber (thickness of 1.5 μm) are used for the material data GGI=0, 0.31, 0.45, 0.66 and 1 with the corresponding E_g values 1.04 eV, 1.2 eV, 1.29 eV, 1.43 eV and 1.68 eV. The other layers are kept constant like CdS buffer with 50 nm, the front contact with 1000 nm i-ZnO/n-ZnO. The basic material specific input parameters based on [56, 66] are summarized in table 2.1. As explained in section 2.2.4, the absorber structure has been modeled by means of three separate layers with different E_g values for each layer, representing the front, center and back regions of the CIGSe absorber. The individual E_g values are determined using equation 4.5 and linear GGI concentration gradients are directly transferred to linear E_g variations. All four depth profiles in figure 4.11 have the same structure, a more or less constant GGI ratio at the front (E_g at the front) a linear increasing GGI ratio in the intermediate region (E_g in the intermediate region) and a more or less constant GGI ratio at the back (E_g at the back). The experimental J_{sc} trend for intermediate Se supply is well reflected

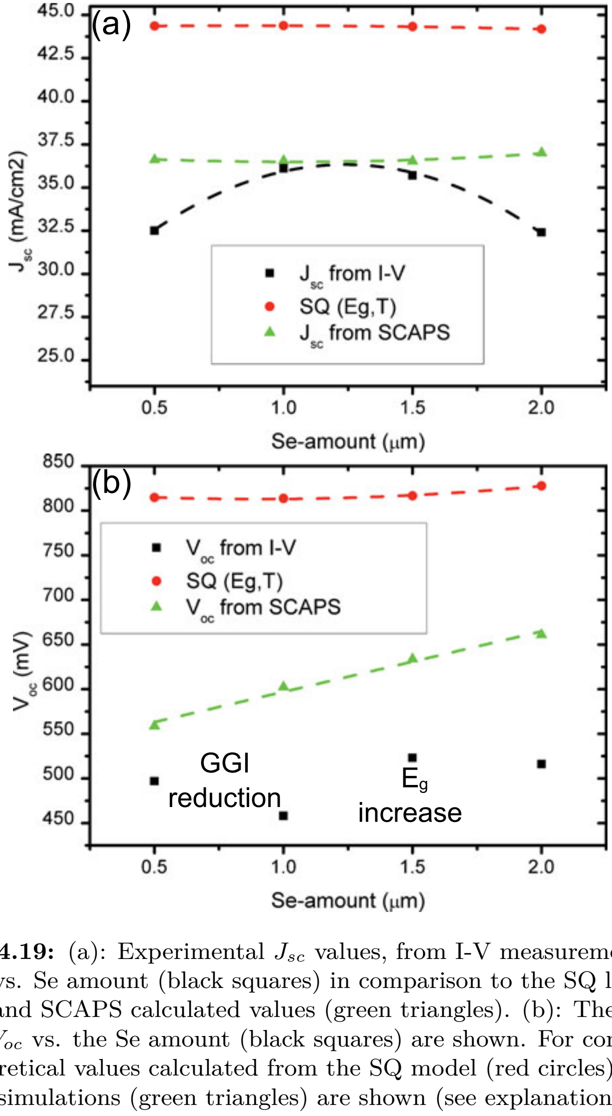

Figure 4.19: (a): Experimental J_{sc} values, from I-V measurements, are plotted vs. Se amount (black squares) in comparison to the SQ limit (red circles) and SCAPS calculated values (green triangles). (b): The experimental V_{oc} vs. the Se amount (black squares) are shown. For comparison, the theoretical values calculated from the SQ model (red circles) and SCAPS simulations (green triangles) are shown (see explanation in main text) (reproduced from [13] with permission of Elsevier Publishing).

by the SCAPS simulations. However, for high and low Se supply there is a larger difference between simulations and experimental values, which indicates the presence of additional factors reducing the performance of the cell, like $MoSe_2$ layer growth and reduction of CIGSe grain size.

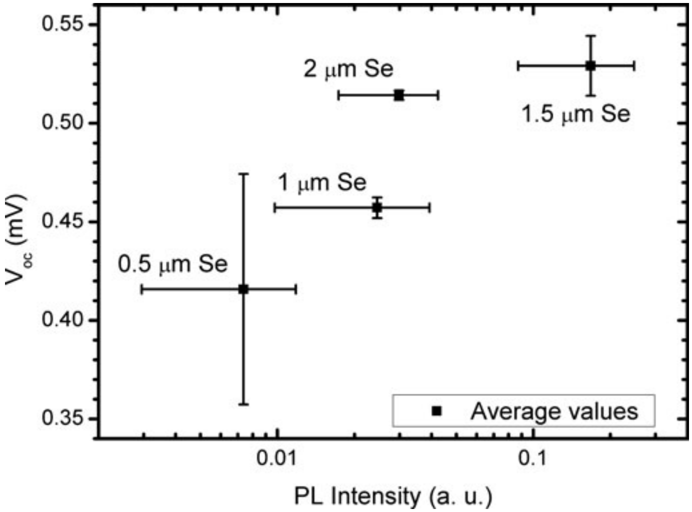

Figure 4.20: Semi log arithmic plot of the average V_{oc} vs. average PL intensity. Additionally, the standard deviation for each series of solar cell devices are given along the intensity and voltage axis.

The SCAPS simulations predict that the V_{oc} increases linearly with Se supply, which supports the expectation of a positive effect of high Se supply on the cell performance. An increasing GGI ratio at the front also means an increasing E_g in the absorber, which should lead to an increasing V_{oc} value in the solar cell. According to the fact that the Se amount increases the GGI ratio at the front, an increasing V_{oc} trend with Se amount is recognized for the SCAPS simulations. In the real CIGSe solar cells presented here the influence on the V_{oc} value is more complex and cannot only be described by the absorber properties alone. According to [12] and [115], the V_{oc} can be furthermore influenced by interface recombinations at the back contact interface and the p-n junction heterointerface.

In figure 4.20, the average V_{oc} value vs. the log values of the average PL intensity are shown. Up to Se supply of 1.5 μm, a monotonic increase of V_{oc}

with PL intensity has been observed [21]. The highest V_{oc} is reached for the 1.5 μm Se sample, which also has the highest PL intensity signal (see figure 4.20). These observations can be understood considering the relationship of PL yield (Y_{PL}) with quasi-fermi level splitting ($\Delta\mu$): $\ln(Y_{PL}(E)) \approx \Delta\mu$ [21]. $\Delta\mu$ represents the maximum achievable V_{oc} according to [9,21].

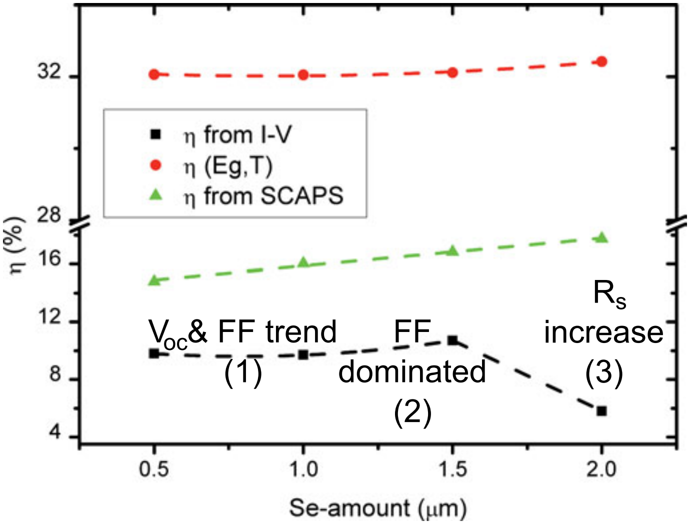

Figure 4.21: Plot of η vs. Se amount (black squares). The data can be divided into V_{oc} dominated (1), FF dominated (2) and R_s dominated (3) regions. In comparison, the values calculated from SQ model (red circles) and SCAPS simulated (green triangles) values vs. E_g are shown (reproduced from [13] with permission of Elsevier Publishing).

The η trend with increasing Se supply in figure 4.21 can be explained by the combined effect of the V_{oc} increase, which dominates in the region of 0.5-1.5 μm, and the increase of R_s with Se supply, which dominates for high Se supply (2 μm).

Short summary

With a higher Se supply, a more homogeneous CIGSe absorber is formed with regard to Ga and In distribution, which is proven by XRD and characterization of the optical properties. For high Se supply, a narrow 112 Bragg reflection is found, indicating a better homogeneity of the lattice parameter. This finding is further supported by an increase of E_g (as determined from PL, IQE and GDOES studies) with the Se amount. These results demonstrate the beneficial effect of increased Se supply on the Ga/In interdiffusion inside the CIGSe. The shift of the CIGSe A1 Raman mode shows that the surface properties also follow this trend. The GGI ratio next to the surface appears to be proportional to the Se supply during the chalcopyrite formation. Ga/In interdiffusion coefficients in the range 3.3E-12 $\frac{cm^2}{s}$ to 3.9E-12 $\frac{cm^2}{s}$ at 575 °C have been found from evaluation of the GGI concentration profiles. The depth profiles show a less pronounced degree of Ga grading towards the back contact with increasing Se supply. A linear increase of V_{oc} with increasing PL intensity of the thin films is observed, which indicates a reduced amount of non-radiative recombination for the optimum Se supply used. Although an enhanced Ga incorporation near-surface has been achieved, the CIGSe properties still remain far behind the theoretical limits, which is clearly demonstrated by comparison with the calculated values obtained from 1D SCAPS modeling. The results demonstrate that an overall improvement of the CIGSe solar cell performance can only be achieved with an optimized back contact system (lower $MoSe_2$/Mo ratio), while simultaneously maintaining the homogeneity inside the CIGSe layer.

4.1.3 Phase formation with a diffusion barrier layer at the back contact

In the previous chapter, it has been demonstrated that a high Se amount (Se partial pressure) during the SEL process is beneficial for the CIGSe absorber layer in terms of Ga/In interdiffusion and Ga enhancement at near-surface regions. However, the high Se supply leads to back contact corrosion, which results in adhesion problems of the film and an increase of the R_s of the solar cell device. This chapter presents a new approach for an alternative back contact system which includes a functional Mo-N layer. The results have already been published in [14] (reproduced with the permission of Elsevier Publishing).

Introduction

During the "aggressive" SEL process with solid chalcogen layers an enhanced $MoSe_2$ formation at the interface to the CIGSe takes place [13]. $MoSe_2$ formation at the back contact starts at approximately 400 °C at a moderate Se pressure in the presence of CIGSe [116]. A thick $MoSe_2$ layer limits the current collection efficiency of the back contact due to its increased resistivity in comparison to pure Mo [117]. Additionally, the layered structure CIGSe/$MoSe_2$/Mo can peel off due to an increased overall compressive stress. This limits the amount of Se which can be supplied during the SEL process, since otherwise the cell performance may be severely affected by the corrosion of the back contact. On the other hand, a sufficient Se supply is essential for achieving an optimum absorber structure [13]. A possible solution for this dilemma is the introduction of a diffusion barrier in the back contact area, which may allow to better control the amount of $MoSe_2$ formation at the back contact. Diffusion barriers are widely used in microelectronic systems [118, 119]. Several systems consisting of W, Cr, Ta, Nb, V, Ti and Mn together with the metal nitrides have been established in the past [120]. Very promising diffusion barrier concepts are based on TiN [121, 122]. Ultrathin Mo-N/Mo bilayers are used in nanostructures [123]. Furthermore Mo-N is applied in layered semiconductor systems to prevent Cu diffusion [124]. The advantage of Mo-N as diffusion barrier material is that it requires little process modification if the reactive sputtering process in N_2-Ar atmosphere [125] is used (also used in this work). Alternative approaches are given in [126], where Mo-N is grown by a pulsed laser deposition technique under N_2 radical exposure. The aim here is to find the optimum thickness of reactively sputtered Mo-N diffusion barrier layers in terms of back contact conductivity and diffusion barrier efficiency.

Growth of reactive sputtered MoN on Mo

In this part of the thesis a new approach for an alternative back contact system is investigated, where a functional Mo-N layer is reactively sputtered above a conventional Mo back contact. The process for the Mo-N/Mo layer stack growth (see figure 4.22) can be controlled by the sputter voltage V (in V), process pressure p (in mbar) and N_2/Ar flux (in sccm) vs. process time t (in s). In figure 4.22 (a) one can observe Mo deposition on glass for 3 min; afterwards a transition part to Mo-N takes place for 10 s, followed by the final Mo-N deposition step for 25 s. A pure Mo-N deposition process for 100 s in figure 4.22 (b) also includes the 10 s transition part, where the N_2 flux is increased from 0 sccm towards 200 sccm. In consequence V is rising to 600 V at constant sputter power of 8 kW. The different voltage levels for Mo and Mo-N sputtering originate from the change of the work functions of the target surface due to the fact that the Mo target surface is nitrided in the reactive atmosphere. The process pressure during the individual steps is explicitly adjusted with mass flow controllers to ensure good adhesion and conductivity of the Mo-N/Mo layer sequence.

Se reaction with Mo back contact

Mo is widely used as a back contact material for CIGSe solar cells [116] because it is thermally stable at the process temperatures and has good conducting as well as reflecting properties [127]. A thin $MoSe_2$ layer between CIGSe and Mo is desirable, since it forms a quasi ohmic contact in contrast to a Schottky-like CIGSe-Mo contact [127].

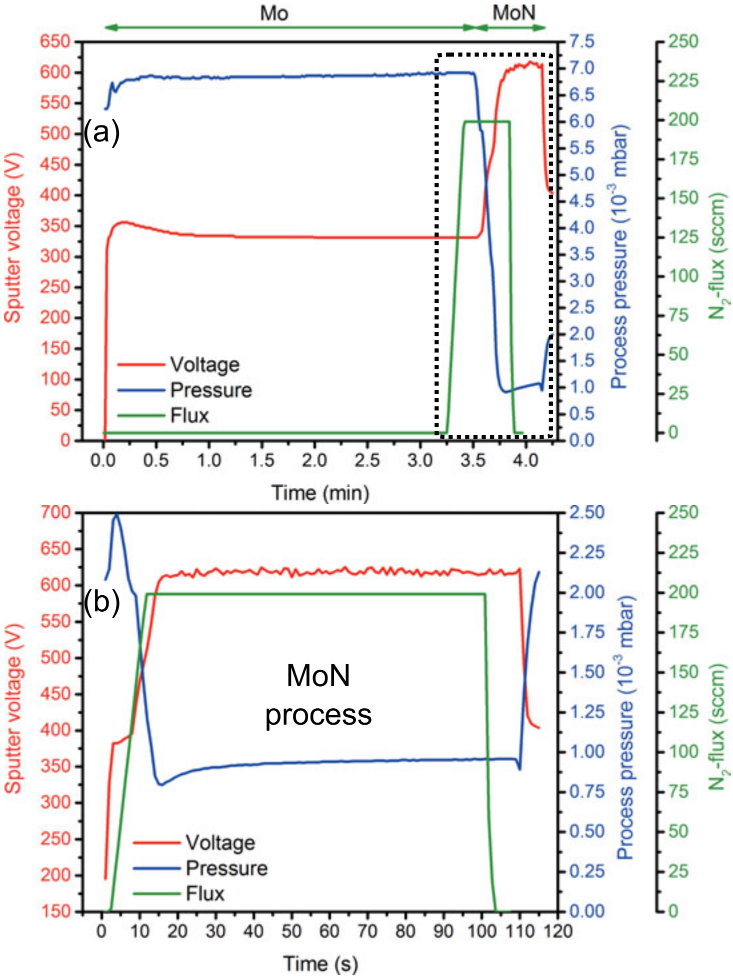

Figure 4.22: (a): Deposition process parameters voltage (black line), pressure (red dashed) and N_2 flux (green dotted) of Mo-N/Mo on glass substrates vs. process time. (b): In-view into the Mo-N reactive sputter process vs. time (reproduced from [14] with permission of Elsevier Publishing).

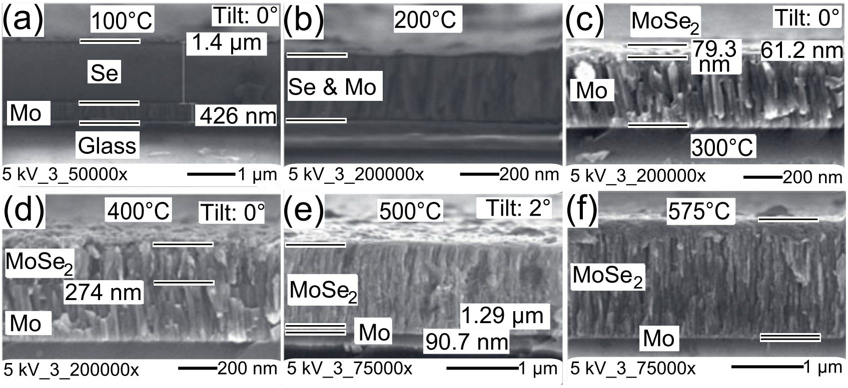

Figure 4.23: (a-f): Cross sections of pure Se/Mo stacks annealed at 100-575 °C. Strong morphology change in cross section at the back contact can be observed together with thickness increase as a consequence of $MoSe_2$ formation. The white bars highlight the thickness of the Se layer in (a), the Se-Mo layer in (b) and the Mo layer in (c-f). The numbers indicate the Mo and Se layer thickness in (a) and the $MoSe_2$ layer thickness in (c-f) (reproduced from [14] with permission of Elsevier Publishing).

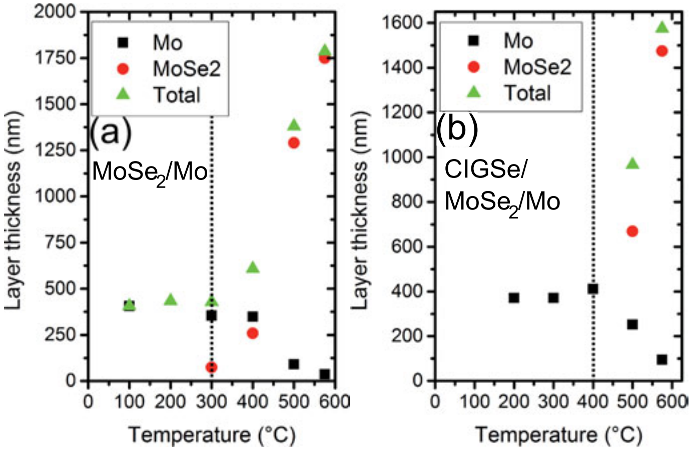

Figure 4.24: Layer thickness of Mo (black squares), $MoSe_2$ (red circles) and total thickness of the back contact (green triangles) at different temperatures for the system Mo-Se in (a) and the system Mo-CIGSe in (b). The starting points for $MoSe_2$ formation are determined at 300 °C and 400 °C respectively according to SEM analysis (reproduced from [14] with permission of Elsevier Publishing).

Additionally, the orientation of $MoSe_2$ influences the conductance and adhesion between CIGSe absorber and Mo back contact. The control of the $MoSe_2$ formation at the back contact is a very important topic in CIGSe growth during the SEL process. Figure 4.23 shows cross sections of selenized Mo back contacts for different process temperatures.

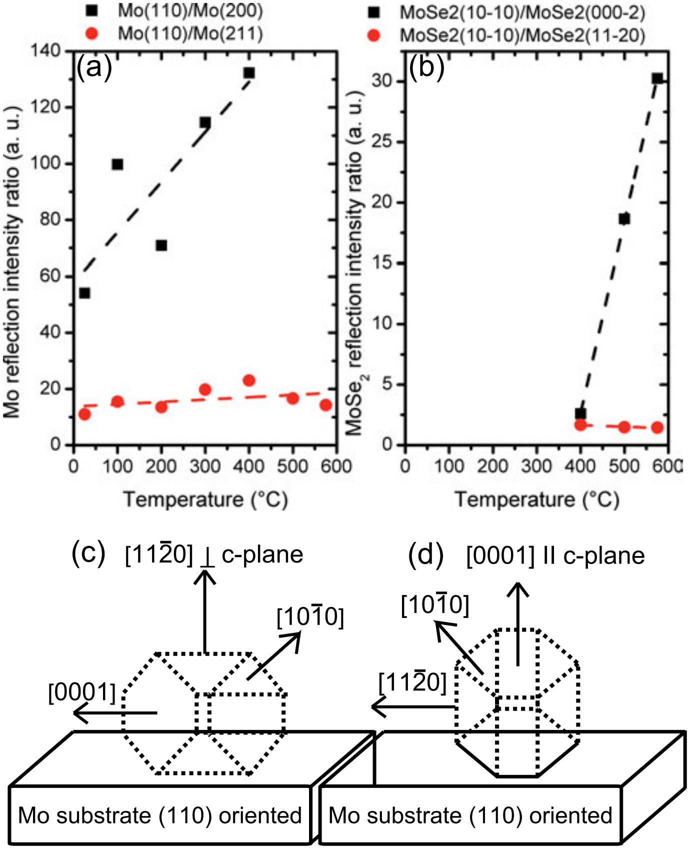

Figure 4.25: (a): 110/200 and 110/211 reflection intensity ratios of Mo. (b): $MoSe_2$ $10\bar{1}0/000\bar{2}$ and $10\bar{1}0/11\bar{2}$ reflection intensity ratios at different temperatures (reproduced from [14] with permission of Elsevier Publishing).

The growing $MoSe_2$ layers have similar columnar grains like Mo close to the interface [116]. The corresponding layer thicknesses of Mo, $MoSe_2$ and total back contact are shown in figure 4.24 (a). Additionally the layer thicknesses of Mo, $MoSe_2$ and total back contact in the presence of the CIGSe thin film are summarized in figure 4.24 (b). The overall volume expansion of the back contact starts at 300 °C (see figure 4.23 (c) and 4.24), which is recognized by the phase contrast in SEM cross section. It is important to advise a growth direction of $MoSe_2$ film perpendicular to the substrate surface like $[10\bar{1}0]$ and $[11\bar{2}0]$, which is highly relevant for the electronic properties of the CIGSe solar cells. Increasing the temperature towards 400 °C results in an enhanced Mo 110 texture (see figure 4.25 (a)) and the Mo 200 reflection vanishes at 400 °C (not shown here) due to an overlapping $MoSe_2$ $11\bar{2}0$ reflection, which is seen in the corresponding XRD patterns. According to figure 4.25 (b), a strong $MoSe_2$ growth into the $[10\bar{1}0]$ and $[11\bar{2}0]$ direction is identified above 400 °C because the ratio of $10\bar{1}0/000\bar{2}$ increases while the $10\bar{1}0/11\bar{2}0$ ratio stays constant.

Influence of MoN interlayer on Se reaction with Mo back contact

The Mo-N/Mo layer is selenized at a temperature of 575 °C and a Se amount of 1.5 μm, which is shown in the cross section in figure 4.26 (a). The different layers are analyzed with the help of EDX measurements (see figure 4.26 (b-d)) and Raman scattering (see figure 4.26 (e)). According to the SEM image, just a thin $MoSe_2$ layer has formed near-surface (see figure 4.26 (a)). The Mo-N interlayer forms a partial diffusion barrier against Se vapor, which leads to a growth limited thin $MoSe_2$ layer relatively independent of Se supply in the reaction chamber. The Se-reacted Mo-N/Mo sample is analyzed by EDX on the surface (Spectrum 1), intermediate (Spectrum 2) and bottom layer (Spectrum 3) region (see figure 4.26 (b-d)). A reduction in the Se signal at 1.4 keV in the excited volume from the top to the bottom (red arrow in the EDX spectra) has been observed, which originates from a limited Se penetration into the Mo-N/Mo film. Surface sensitive Raman scattering (see figure 4.26 (e)) is used to analyze the top few nanometers of the absorber. A $MoSe_2$ compound formation is identified by the characteristic E_{1g}, A_{1g} and E_{2g} Raman modes.

XRD measurements give information about the rate of $MoSe_2$ formation by comparing the relative reflection intensities of the Se/Mo samples (black curve) with the Se/Mo-N/Mo samples (red curve) in figure 4.27. Both

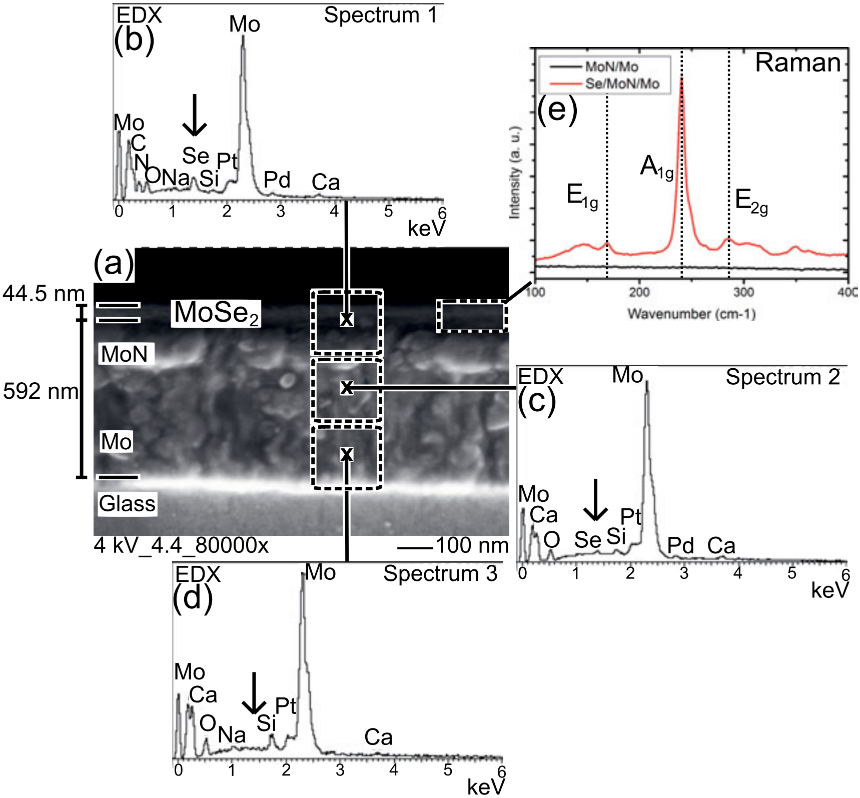

Figure 4.26: (a): SEM cross section of the layer stack $MoSe_2$/Mo-N/Mo is shown. Additionally, the corresponding EDX spectra for near-surface (b), intermediate (c) and bottom layer (d) region are included. (e): Raman spectrum of the $MoSe_2$/Mo-N/Mo sample (reproduced from [14] with permission of Elsevier Publishing).

samples were selenized under the temperature of 575 °C and with a Se amount of 1.5 μm. Additionally, it is notable that the preferred orientation of the $MoSe_2$ film seems to change from a $[10\bar{1}0]$ and $[11\bar{2}0]$ for standard back contacts towards a $[000\bar{2}]$ oriented growth for Mo-N containing diffusion barriers. The Mo-N film is represented by the Mo-N 111 and Mo_2N 112 reflections, which overlap and appear as a single asymmetric peak at approximately $2\theta = 36.5\,°$. The growth mechanism of $MoSe_2$/Mo and $MoSe_2$/MoN/Mo is schematically shown in figure 4.28. The Mo substrate

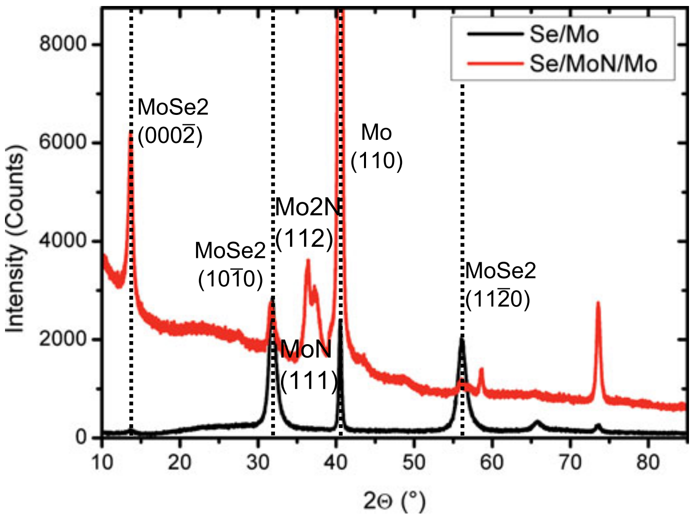

Figure 4.27: XRD pattern of Se-reacted back contacts in the conventional Mo back contact (black line) and the modified Mo-N/Mo system (red line). The presence of a Mo_2N 112 and Mo-N 111 reflection indicates formation of the Mo-N thin film. The reflection intensity ratios of 10$\bar{1}$0 $MoSe_2$ / 110 Mo and 11$\bar{2}$0 $MoSe_2$ / 110 Mo are significantly reduced for the sample without an additional diffusion barrier (reproduced from [14] with permission of Elsevier Publishing).

is [110] oriented and the preferred $MoSe_2$ growth direction changes when a thin Mo-N interlayer is introduced.

In order to analyze the functionality of the Mo-N diffusion barrier, samples with different Mo-N thicknesses (Mo-N sputtering time 25-120 s) and different selenization conditions (0.5-1.5 μm Se layer thickness and a temperature of 575 °C) have been produced. The SEM cross sections in figure 4.29 show a similar columnar growth of Mo-N on top of Mo like for the pure Mo. In the case of the 0.5 μm Se sample a thin film with a flake-like structure is observed at near-surface regions. The 1.5 μm Se samples show a similar flake-like surface layer with a larger thickness as compared to the 0.5 μm Se samples.

The thickness of the total back contact does not increase significantly with a longer Mo-N sputtering time, which is also related to the increasing

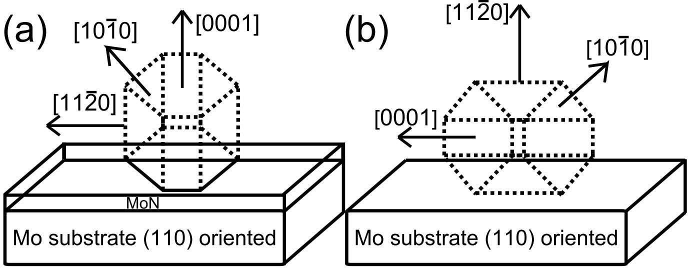

Figure 4.28: Growth model of $MoSe_2$ in the single crystal approach for the case of an [110] oriented Mo substrate with (in (a)) and without (in (b)) an additional Mo-N interlayer (reproduced from [14] with permission of Elsevier Publishing).

poisoning of the Mo target with sputter time (reactive sputter process with N_2) [125]. An average deposition rate of 0.65 nm/s (see table 4.8) is estimated in between 0 s and 25 s deposition time with respect to the error of thickness measurement according to the SEM cross sections (Mo-N layer thickness=total layer thickness-500 nm). The 500 nm is related to the Mo average thickness in the sputter process on float glasses.

Furthermore, the back contact thickness appears to be nearly independent of Se supply. Only a small thickness increase of the flake-like structure is observed from the 0.5 μm to the 1.5 μm Se samples, which proves the functionality of the Mo-N interlayer. According to EDX analysis, the flake-like structure mainly consists of $MoSe_2$ for all Mo-N sputtering times. That means that Mo-N/Mo shows a strongly reduced $MoSe_2$ growth at moderate selenization temperatures in comparison to the Mo reference. The more [000$\bar{2}$] oriented growth of $MoSe_2$ on Mo-N/Mo can be explained

Table 4.8: An overview of the average deposition rate of Mo-N for the different sputtering times 25 s, 45 s, 60 s and 120 s.

Deposition time (s)	Deposition rate (nm/s)
0-25	0.65
25-45	0.52
45-60	0.43
60-120	0.32

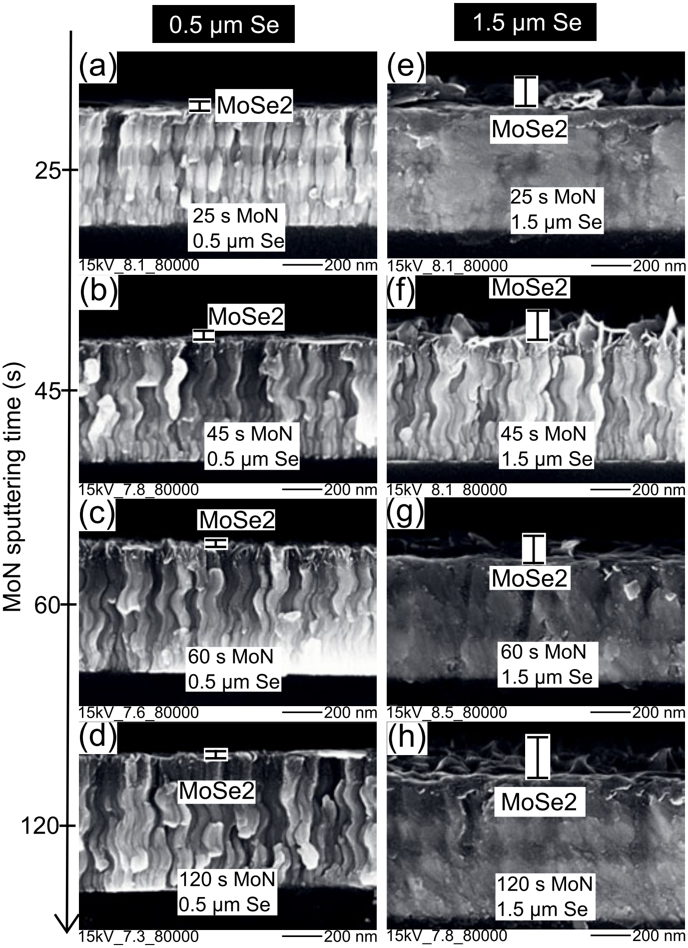

Figure 4.29: SEM images of cross sections of Mo-N/Mo samples with different Mo-N sputtering times after reaction with 0.5 μm (a-d) and 1.5 μm (e-h) Se. The Mo-N layer thickness is varied by running the sputtering process for 25 s (a,e), 45 s (b,f), 60 s (c,g) and 120 s (d,h) sputtering time. A thicker $MoSe_2$ surface layer with a flake-like structure is observed for the 1.5 μm samples (reproduced from [14] with permission of Elsevier Publishing).

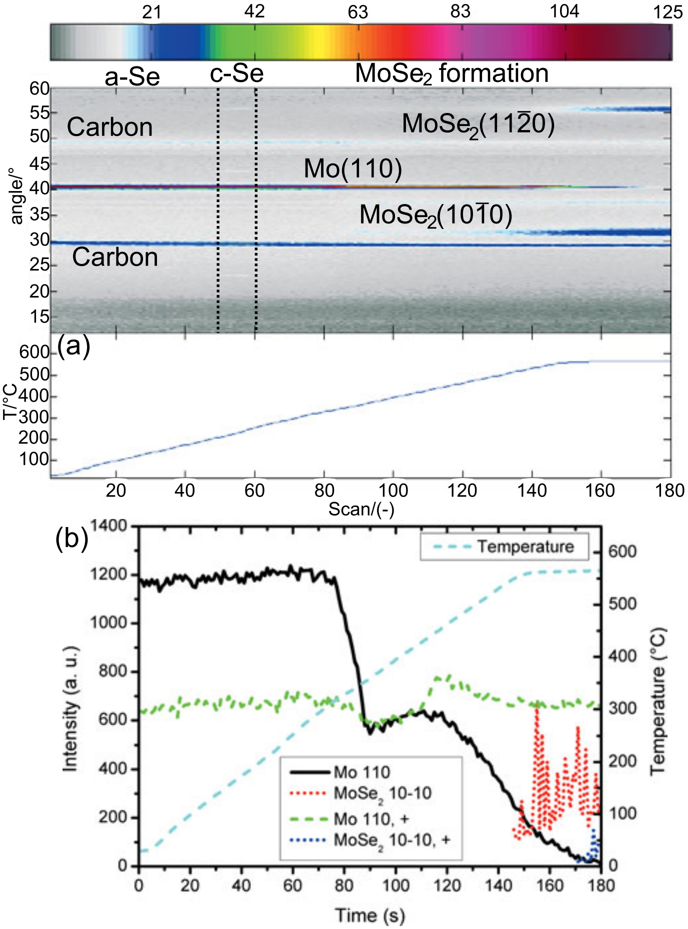

Figure 4.30: (a): In-situ XRD pattern of a Se/Mo/glass sample during heating for 15 min towards 575 °C and with a holding time of 3 min (see temperature-time profile at the bottom). $MoSe_2$ formation is observed starting from approximately 343 °C by an increasing $10\bar{1}0$ and $11\bar{2}0$ reflection intensity. (b): Reflection intensities extracted with the help of Pseudo Voigt fits vs. time for the Mo 110 and $MoSe_2$ $10\bar{1}0$ Bragg reflections of samples with (identification with +) and without an additional Mo-N diffusion barrier (reproduced from [14] with permission of Elsevier Publishing).

by a quasi-epitaxial relation between Mo-N and $MoSe_2$. With the help of in-situ XRD analysis the $MoSe_2$ formation on standard Mo and on Mo-N/Mo is investigated as a function of temperature. The reflection intensities have been extracted by fitting with a Pseudo Voigt function [11, 15]. Representative in-situ XRD data are shown for the case of Mo rich back contact in figure 4.30 (a), which clearly shows the evolution from a Mo rich back contact (strong Mo 110 reflection) towards an increasing $MoSe_2$ amount at the back contact (rising $MoSe_2$ $10\bar{1}0$ and $11\bar{2}0$ reflection intensity) until the Mo signal vanishes (see figure 4.30 (b)). However, samples with a Mo-N diffusion barrier show a persistent Mo 110 reflection intensity, which indicates a diffusion limited selenization process at the back contact (see figure 4.30 (b), green short dots).

Influence of Mo-N interlayer properties on the CIGSe absorber growth

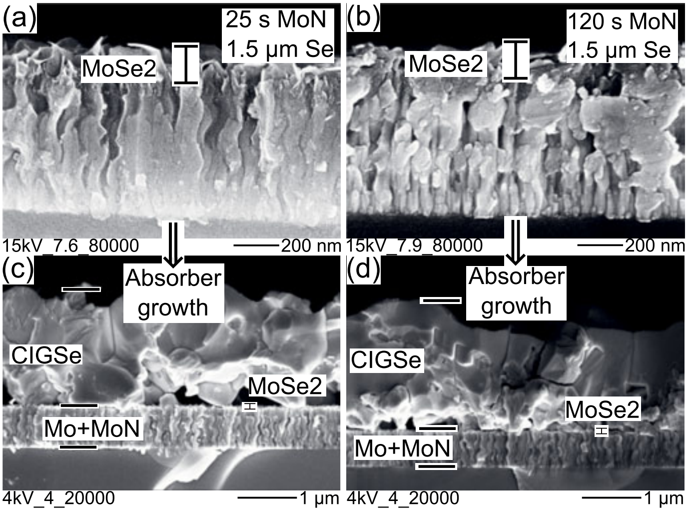

Figure 4.31: Cross sections of CIGSe/Mo-N/Mo films processed by a 25 s Mo-N sputtering time in (a) and 120 s in (b) reacted with 1.5 μm Se under 575 °C (reproduced from [14] with permission of Elsevier Publishing).

In order to find out the optimum Mo-N sputtering times for best solar cell performance, structural characterization, electronic analysis and modeling are performed. The CIGSe thin films are prepared according to the SEL process with 1.5 μm Se amount at 575 °C, which results in a CGI ratio of 0.9 and a GGI ratio of 0.27 with a CIGSe absorber thickness of 1.6 μm. SEM cross sections of the CIGSe/Mo-N/Mo films with 25 s and 120 s Mo-N sputtering times show a comparable film thickness (see figure 4.31) and back contact dimension. Furthermore, the CIGSe morphology does not differ significantly, including the grain size of both CIGSe films.

The XRD patterns of the two films (see figure 4.32) show MoN 111 and Mo_2N 112 reflections [125] of the Mo-N/Mo substrate and the Se reacted Mo-N/Mo film. The presence of the SEL stack CuGa and In on top of Mo-N during the selenization process strongly influences the Mo-N texture towards (001) [125]. Like in almost all SEL processed CIGSe absorbers, a strong 112 texture is observed which is characterized by the 112/220 and 112/312 ratios of 5.28 and 11.9 respectively. Additionally, the intensity of the CIGSe reflections 112, 220/204 and 312/116 for the 25 s sample (see figure 4.32 (a)) is enhanced in comparison to the 120 s sample (see figure 4.32 (b)) by approximately a factor of 2 (see table 4.9). The CIGSe sample with 120 s sputtered Mo-N diffusion barrier shows a 112 reflection with a huge FWHM in figure 4.32 (b), which is the effect of small grain sizes or compositional inhomogeneities. Mo-N is still working well for Se amounts of 2 μm or even 3 μm in terms of avoiding Mo back contact corrosion (not shown here). According to I-V curve (see figure 4.33, and parameters extracted from curves in table 4.10), solar cells with a Mo-N diffusion

Table 4.9: Reflection intensities of the 112, 220, 312 reflections and the calculated ratios I_{112}/I_{220} and I_{112}/I_{312} for the 25 s and 120 s CIGSe samples, also in comparison to CISe (00-035-1100) and CGSe (JCPDS 00-040-1487) powder values.

Mo-N (s)	I_{112} **(Counts)**	I_{220} **(Counts)**	I_{312} **(Counts)**	$\frac{I_{112}}{I_{220}}$	$\frac{I_{112}}{I_{312}}$
25	77905.4	14753.9	6547.7	5.3	11.9
120	30891.8	7569.2	2922.9	4.1	10.6
Powder$_{CISe}$				1.96	4
Powder$_{CGSe}$				4	3.33

barrier (interlayer) show an increased FF for the 25 s Mo-N sample, which is caused by a reduced $MoSe_2$ layer thickness (reduced R_s in the device). However, the V_{oc} is slightly decreased which might be related to additional recombination processes at the back contact interface due to the preferred $MoSe_2$ growth with [0001] direction perpendicular to substrate surface. The 120 s Mo-N sample is strongly shunted, which can be seen in the shape of the dark and illuminated I-V curve (especially in the slope at 0 V). This is related to a low R_p in the device, which can be related to the reduced crystal quality (increased FWHM) of the CIGSe film structure.

Short summary

It has been shown here that the introduction of Mo-N as a diffusion barrier into the Mo back contact prevents Se incorporation into the back contact, thus reducing Mo back contact corrosion. Mo-N grows on Mo in a self-limited process up to a well defined thickness. A self-limited thin $MoSe_2$ film is observed when the Mo-N/Mo is selenized. The $MoSe_2$ thin film grows as flake-like structures on the Mo-N/Mo surface with the $[000\overline{2}]$ direction perpendicular to the substrate surface. This is different from the growth behavior on standard Mo substrates, where a $[10\overline{1}0]$ and $[11\overline{2}0]$ orientation of the $MoSe_2$ perpendicular to the substrate surface is observed. From an electronic viewpoint, the solar cell performance (as measured by

Table 4.10: The solar cell performance parameters η, V_{oc}, J_{sc} and FF of solar cells with a 25 s and 120 s sputtered Mo-N diffusion barrier and a pure Mo reference sample as comparison. The best performance values for each solar cell modification are shown together with the arithmetic average values (ave) with the corresponding standard deviations.

MoN (s)	η (%)	V_{oc} **(mV)**	J_{sc} **(mA/cm2)**	FF (%)
0	10.7	523	35.7	57.4
ave	9.4 ± 0.9	529.1 ± 15.2	35.2 ± 0.5	50.6 ± 5
25	12.1	517.1	35.9	65.3
ave	10.6 ± 0.6	490.1 ± 14.7	34.9 ± 0.7	62.1 ± 2.5
120	5.4	431.6	30.1	41.3
ave	2.1 ± 1.7	296.5 ± 113.3	20.14 ± 9	30.8 ± 6.9

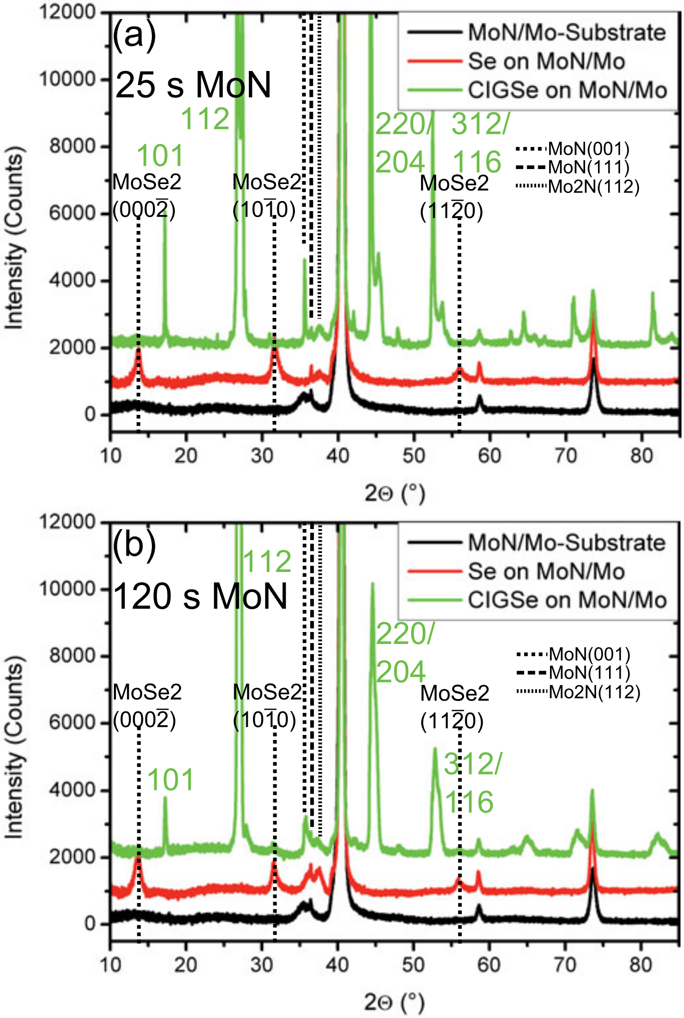

Figure 4.32: Overview of the XRD pattern of as-grown Mo-N/Mo (black line), Mo-N/Mo reacted with 1.5 μm Se at 575 °C (red line) and films consisting of CIGSe/Mo-N/Mo (green line) with Mo-N sputtering time of 25 s (in (a)) and 120 s (in (b)). The strongest CIGSe, Mo, $MoSe_2$ and Mo-N reflections are highlighted by the dashed lines in the diagram (reproduced from [14] with permission of Elsevier Publishing).

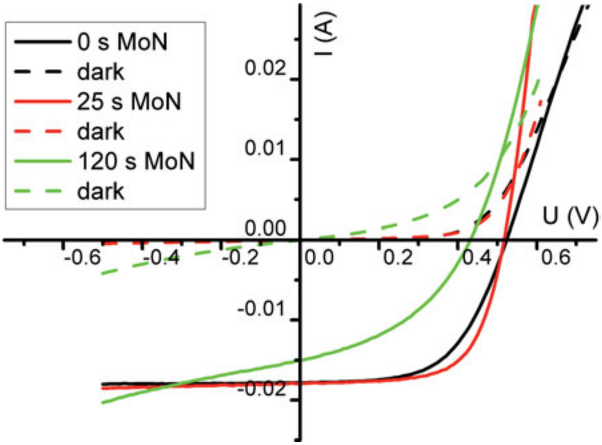

Figure 4.33: Dark (dashed lines) and illuminated (solid lines) I-V curves of solar cells with an additional 25 s and 120 s Mo-N diffusion barrier in comparison to solar cells based on a pure Mo back contact. The illumination was performed with an AM 1.5 spectrum (reproduced from [14] with permission of Elsevier Publishing).

η and FF) can be improved with relatively short Mo-N sputtering times in comparison to the pure standard Mo back contact.

4.1.4 Influence of high temperature processes

The last two chapters dealt with the influence of the Se amount on the Ga/In profile and the back contact corrosion in the SEL. It was found that for a better absorber quality, a high Se partial pressure (Se amount) is required and therefore also a functional diffusion barrier is needed in the cell structure. The current chapter reports about the influence of temperature and glass substrate on Ga/In interdiffusion and chalcopyrite phase formation in the SEL process. According to the SQ limit, the optimum E_g for single junction device is near 1.4 eV, which is strongly coupled on the GGI ratio of CIGSe thin film solar cells. To increase the Ga content in the active region of the CIGSe a 70:30 CuGa alloy target is used. The results have already been published in [15] and are reproduced with permission of Elsevier Publishing.

Introduction

The strong influence of Na on the chalcopyrite solar cell performance is a surprising result of many investigations over the last decades and still leaves a lot of questions open. From an electronic perspective, Na generally increases the carrier concentration in the solar cell [73, 128, 129]. From CIGSe growth perspective, Na is responsible for an enhanced grain growth. The Na diffusion from the glass into the CIGSe inhibits the Ga/In interdiffusion by preventing the Ga out-diffusion in the stage of binary selenide growth [130]. This effect is strongly influenced by the choice of the glass substrates and their specifications, such as Na and K amount. In recent publications, the effect of K on the CIGSe absorber growth has been in focus, as it changes the morphology and leads to a thin Cu-poor surface layer [131, 132]. In the SEL process, higher temperatures during the selenization process accelerate the Ga/In interdiffusion inside the absorber material [130, 133]. Additionally the grain size of the CIGSe will increase due to higher selenization temperature (T_{Se}) [47, 129, 134–137]. In this part of the thesis a special high temperature glass (HTG) from Schott is examined in comparison to a standard float glass (SFG). Within the scope of the public funded project comCIGS II the HTG has been specially designed by Schott to deliver a higher Na supply in contrast to conventional glasses.

Temperature induced phase formation in the chalcopyrite structure

Four different selenization temperatures (T_{Se}=575 °C, 600 °C, 625 °C and 650 °C) on two different glass substrates were chosen to analyze the influence of T_{Se} and Na or K supply on the CIGSe growth. It is interesting to investigate how the Mo/glass interfaces and the glass substrates behave under different thermal treatments.

The temperature next to and above the glass transition temperature (T_g) is of particular interest because it also serves as an indicator for possible diffusing trace elements. These diffusing elements can furthermore influence the Ga/In distribution. For this purpose, light microscope measurements were performed on the back side of the glass in order to adjust the focus plane into the glass substrate near the Mo interface (see figure 4.34). It becomes quite obvious that higher T_{Se} above the T_g of glass leads to delamination at the interfaces which is possibly caused by introducing a huge amount of tension during the cooling down process. Furthermore the difference in coefficient of thermal expansion (CTE) between CIGSe (8-11 ppm/K)/Mo (4.8 ppm/K) [138] and SFG (9 ppm/K) [138] can also influence the deformation (bowing) of the thin film package CIGSe/Mo/glass [138]. The cracks at higher T_{Se} (see figure 4.34 (c,d)) seem to be oriented preferentially. The different behavior of SFG and HTG can be explained by the different glass matrix. The main substance in glass is SiO_2 and its T_g depends on the composition, especially on the amount of network formers and modifiers (Ca, Na, Al, B,...) [139, 140]. However, the addition of elements with valency more than four leads to an increasing silicate bond energy and in consequence increases the T_g. The different optical appearance of SFG and HTG can result from the different Fe content in the glass matrix. The higher the Fe content, the greener the glass becomes.

The composition of the CIGSe does not differ measurably after the annealing process (within the detection limits of the methods applied here) which is recognized in the GGI, CGI and Se/metal ratios (see table 4.11). Additionally, the CIGSe layer thickness stays constant with varying T_{Se}

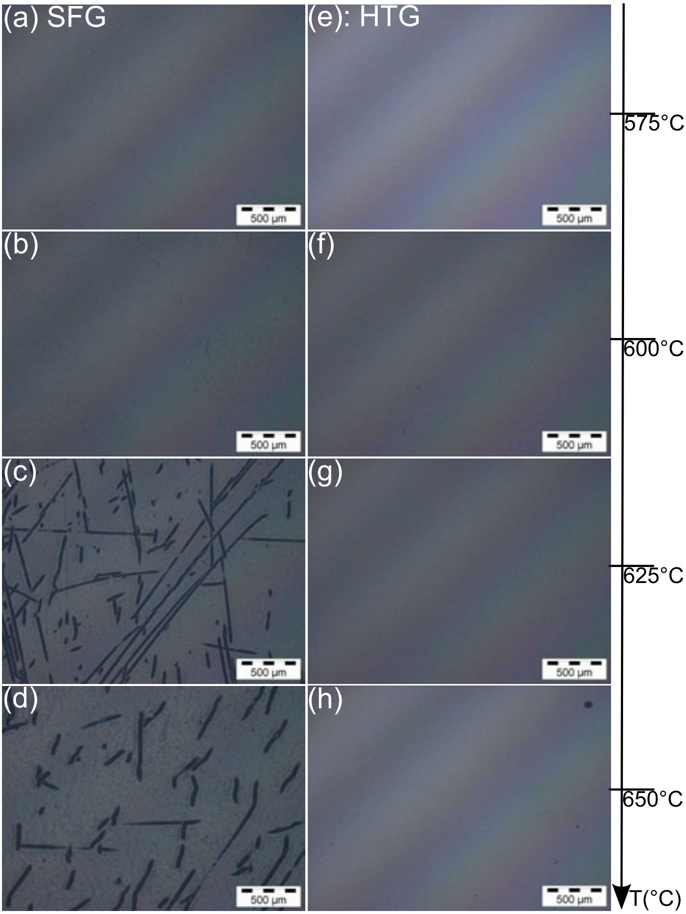

Figure 4.34: Light microscope observations of the Mo/glass interface in the T_{Se} regime from 575 °C to 650 °C for SFG (a-d) and HTG (e-h) from the backside after the annealing process. The SFG shows visible cracks at $T_{Se} \geq 625\,^{\circ}\mathrm{C}$, whereas the morphology of HTG stays unchanged with respect to optical resolution (reproduced from [15] with permission of Elsevier Publishing).

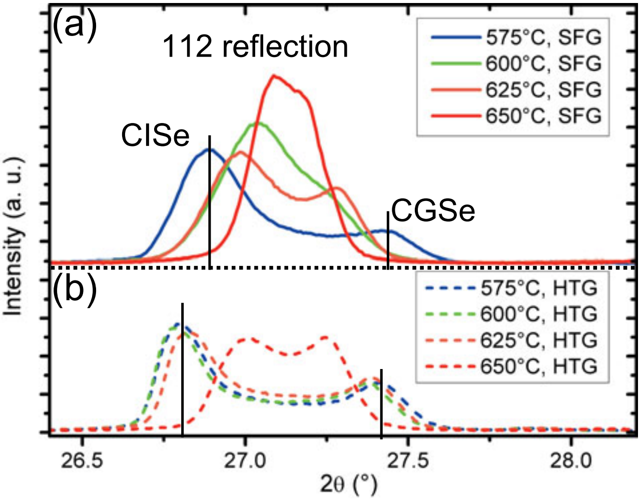

Figure 4.35: The CIGSe 112 reflection profiles of samples on SFG (line) and HTG (dashed) are visualized. The high (CISe) and low (CGSe) intense peak at approximately 26.7 ° and 27.4 ° correspond to the In- and Ga-rich material (reproduced from [15] with permission of Elsevier Publishing).

(no evaporation at high T_{Se}) at approximately 1.6 μm, which indicates that no evaporation of Se takes place at higher T_{Se}. From a structural perspective, the XRD results show a more homogeneous Ga/In distribution inside CIGSe for high T_{Se} for the SFG. In figure 4.35 the 112 reflection profile of CIGSe is shown for the SFG in (a) with lines and for HTG in (b) with dashed lines with varying T_{Se} from 575 °C to 650 °C. The more homogeneous Ga/In distribution can be observed by the 2θ angle position of the high and low intense 112 reflection (degree of asymmetry). In contrary, the degree of asymmetry stays constant for the HTG in the T_{Se} range between 575 °C to 625 °C (see figure 4.35 (b), dashed) and just an abrupt change in the reflection shape for 650 °C occurs. The interdiffusion of Ga and In is the main process influencing the XRD reflection shape. By fitting the reflection profiles with a weighted average function (cumulative) of 2-3 Voigt fits one can approximate the GGI ratio of the thin film (see table 4.12). The degree of grading ($\Delta 2\theta_{112}^{grad}$) as defined according to equation

4.1 (from chapter 4.1.2) indicates the Ga/In interdiffusion amount and a narrow reflection (modeled by Fit 1 - Fit 3) identifies a homogeneous material (small value for the degree of grading).

The reflection intensity ratios, which may be taken as indicators for preferred growth orientation, 112/220, 112/312 and 112/101 in table 4.13 don't show a trend with increasing T_{Se} or grain size according to the SEM images in figure 4.36. The reflection intensity ratios 112/220 and 112/312 are furthermore comparable for both glass substrates displaying values between 2-3 and 4-6 respectively. A dependency of the 112/220 and 112/312 intensity ratios on T_{Se} is not observed. However, the 112/101 ratio seems to be strongly coupled with the nature/choice of the glass substrate for T_{Se} greater than 575 °C. For SFG one observes much higher values (25.11) than for HTG glass (15.4 in the case of 650 °C), which indicates that a higher Na supply suppresses the [101] orientation of the CIGSe grains. Na inhibits the Ga/In interdiffusion [129], which explains the less homogeneous material for absorbers on HTG (at low T_{Se}). Therefore the two parameters temperature and Na content have a different impact on the Ga/In interdiffusion. For CIGSe the CGI ratio is a sensitive factor in determining the grain size [34], which means the higher the ratio, the bigger the CIGSe grains. In [129] it is postulated that the Na content strongly influences the grain size during CIGSe growth in passivating the

Table 4.11: Cation ratios obtained via XRF with a GGI ratio of approximately 0.33. The CGI ratio is found to be close to 0.89 for slightly Cu-poor material. The characteristic Se/metal ratio is approximately 1.1.

T_{Se} $(°C)$	**GGI ratio**	**CGI ratio**	**Se/metal ratio**
SFG			
575	0.32 ± 0.01	0.89 ± 0.01	1.09 ± 0.01
600	0.34 ± 0.003	0.91 ± 0.01	1.1 ± 0.01
625	0.33 ± 0.002	0.91 ± 0.01	1.12 ± 0.004
650	0.34 ± 0.001	0.89 ± 0.01	1.11 ± 0.002
HTG			
575	0.33 ± 0.002	0.9 ± 0.003	1.07 ± 0.003
600	0.32 ± 0.004	0.89 ± 0.01	1.09 ± 0.01
625	0.33 ± 0.002	0.88 ± 0.01	1.05 ± 0.03
650	0.33 ± 0.002	0.9 ± 0.01	1.1 ± 0.01

Table 4.12: The summary of the difference in 2θ fit position ($\varDelta 2\theta_{112}^{grad}$), the weighted average fit position of the three individual fit curves (cumulative) and the calculated GGI ratios (XRD-GGI) for SFG and HTG respectively are shown.

T_{Se} ($°C$)	**Degree of grading** ($\varDelta 2\theta_{112}^{grad}$)	**Cumulative** ($°$)	**XRD-GGI**
SFG			
575	0.51	26.85	0.22
600	0.16	26.96	0.32
625	0.29	26.91	0.27
650	0.02	27.02	0.38
HTG			
575	0.6	26.79	0.15
600	0.58	26.77	0.13
625	0.55	26.8	0.16
650	0.25	26.97	0.33

grain boundaries. However table 4.11 shows that the CGI ratio stays relatively constant for varying T_{Se}. According to SEM cross sections in figure 4.36 (a-d), the grain size increases with temperature for CIGSe on SFG substrates from approximately 1 μm towards 1.5-2 μm. In the case of CIGSe on HTG, the grain size stays relatively constant at 0.7 μm over the T_{Se} range from 575 °C to 625 °C (see figure 4.36 (e-g)). Only the 650 °C sample shows a significant increase of the grain size to approximately 1.5-2 μm (see figure 4.36 (h)). However, the higher amount of Na supplied by the HTG glass has no influence on the grain size in the temperature regime 575 °C to 625 °C on the HTG.

PL analysis examines the E_g at an absorber depth of approximately 200 nm (effective E_g). The E_g is strongly influenced by the T_{Se} between 625 °C and 650 °C (see figure 4.37 (a)). At 650 °C, an E_g around 1.12 eV is found, which is close to a local SQ maximum at $E_g^a = 1.1$ eV [10, 44]. This means that a good solar spectrum matching is possible with the given GGI and CGI ratios for a selenization at $T_{Se} = 650$ °C. The large standard deviation of some samples also reflects the degree of inhomogeneity resulting in E_g fluctuations, which is mainly caused by differing Ga/In ratios in near-surface regions. With the help of the correlation in equation 4.5 with

Table 4.13: An overview of the different ratios for the 112/220, 112/312 and 112/101 reflection intensities is given, also in comparison to CISe (JCPDS 00-035-1100) and CGSe (JCPDS 00-040-1487) powder values. The values for the 112/220 and 112/312 ratios are comparable for both glass substrates. Significantly higher values for the HTG are recognized for the 112/101 ratios.

T_{Se} $(°C)$	I_{112}/I_{220}	I_{112}/I_{312}	I_{112}/I_{101}
SFG			
575	2.34	4.79	15.03
600	2.64	5.17	32.86
625	2.92	5.76	20.99
650	2.57	4.66	25.11
HTG			
575	2.19	4.71	13.69
600	2.14	5.15	19.32
625	1.58	3.48	12.85
650	2.22	5.04	15.4
Powder$_{CISe}$	1.96	4	16.67
Powder$_{CGSe}$	4	3.33	100

a bowing parameter of b=0.21 [114] one can determine which GGI ratio defines the optical E_g measured via PL.

By comparing the relative GGI values evaluated by XRF with the GGI values estimated PL it is possible to estimate whether the E_g increase with T_{Se} is relevant (see figure 4.37 (b)). Interestingly, the samples on SFG tend to have higher E_g values throughout the whole range of T_{Se} regime. The biggest difference, also in comparison to other substrates, is seen for the 600 °C samples on SFG. The origin of this difference in the optoelectronic properties lies in the variation of the Na supply from the glass substrate. A certain amount of Na is necessary to achieve E_g higher than pure CISe, which can be concluded from absorbers on glass with a SiO_xN_y barrier (not shown here). The SiO_xN_y prevents trace elements like Na and K to diffuse from the glass substrate [141] into the absorber during the selenization process. For a depth-resolved in-view into Ga/In profiles, SIMS measurements of the CIGSe on SFG (see figure 4.38 (a)) and on HTG (see figure 4.38 (b)) have been performed. By transforming the SIMS Ga and In profiles into the GGI ratios (see figure 4.38), it is possible

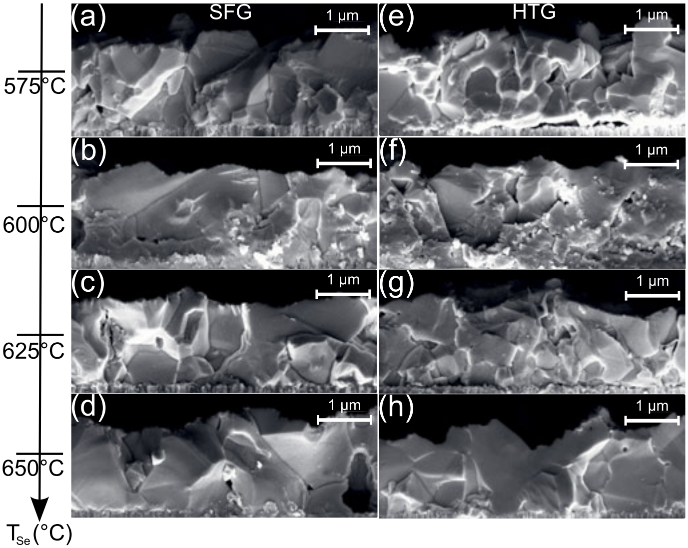

Figure 4.36: SEM cross sections of CIGSe on SFG for increasing T_{Se} from (a-d) and on HTG from (e-h) after selenization at different temperatures for approximately 20 min (reproduced from [15] with permission of Elsevier Publishing).

to extract the group III element distribution versus depth. In order to locate the interface region between CIGSe and Mo in the SIMS profile, one can use the position in which the Mo signal reaches half of its maximum value [103, 111].

It becomes quite obvious that the degree of Ga agglomeration next to the back contact decreases with T_{Se}, which can be interpreted as a result of an enhanced Ga/In interdiffusion. Furthermore, the Ga distribution over the absorber thickness is more homogeneous with increasing T_{Se}, which affects the E_g profile. In order to estimate the diffusivity of Ga inside different CIGSe samples, a two layer diffusion model is used [103, 111]. The interdiffusion coefficients D are taken from fitting of an Gaussian error function to the SIMS GGI profile [13] (see figure 4.39 and 4.40) for varying T_{Se} and glass substrates. The extracted D values are shown in table 4.14. It is observed that D increases from 575 °C to 650 °C for both glass substrates.

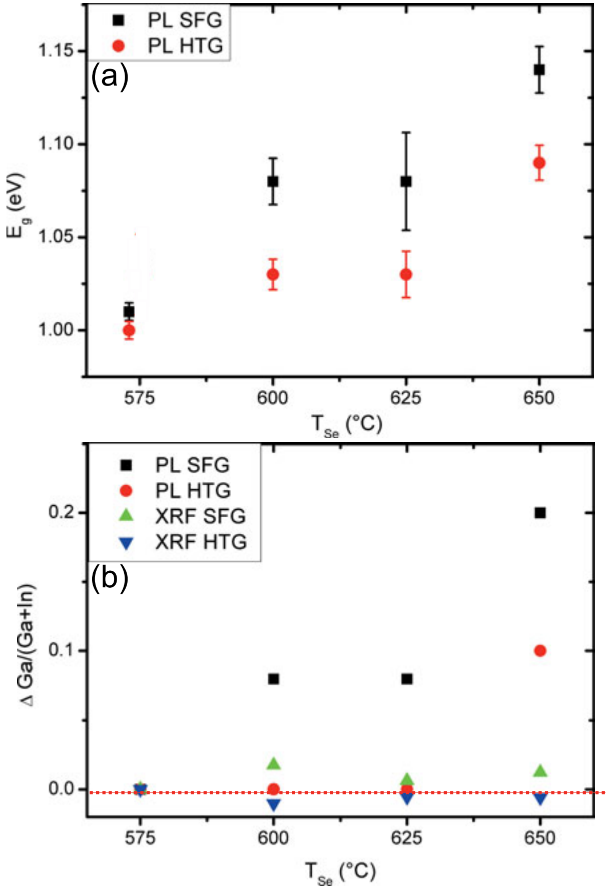

Figure 4.37: (a): Evaluated PL peak position for CIGSe on SFG and HTG are compared for different T_{Se}. (b): The difference between the GGI ratios determined from XRF data or the PL near-surface analysis respectively, are plotted vs. T_{Se} (reproduced from [15] with permission of Elsevier Publishing).

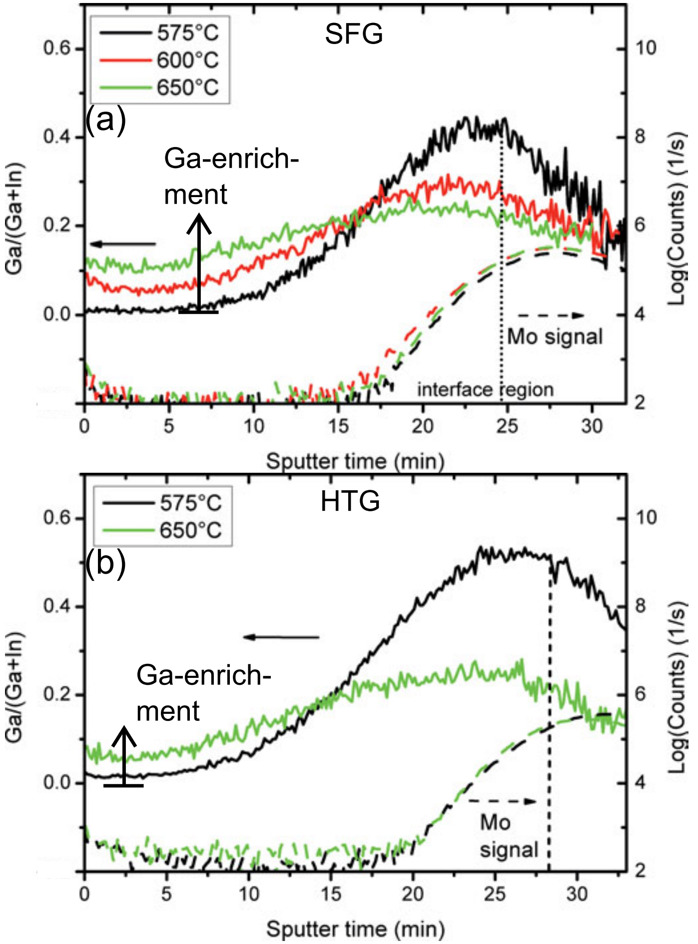

Figure 4.38: Depth resolved GGI ratios from SIMS measurements for CIGSe on SFG for 575 °C, 600 °C and 650 °C in (a) and on HTG for 575 °C and 650 °C in (b). The dashed lines correspond to the Mo signal (log values) on the right axis (reproduced from [15] with permission of Elsevier Publishing).

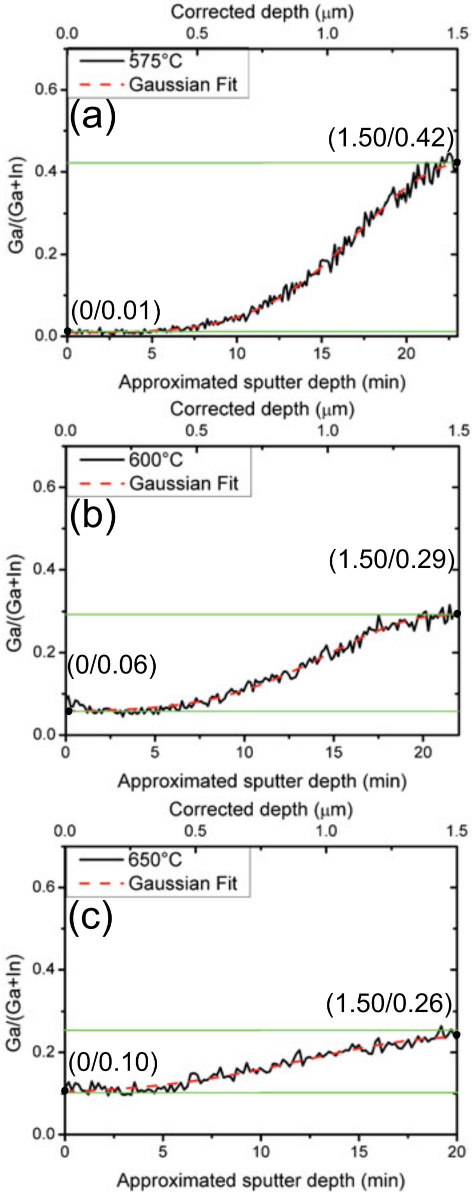

Figure 4.39: Ga/(Ga+In) concentration profiles for different annealing temperatures 575 °C (a), 600 °C (b) and 650 °C (c) on the SFG substrates. The data have been fitted by means of Gaussian error function (reproduced from [15] with permission of Elsevier Publishing).

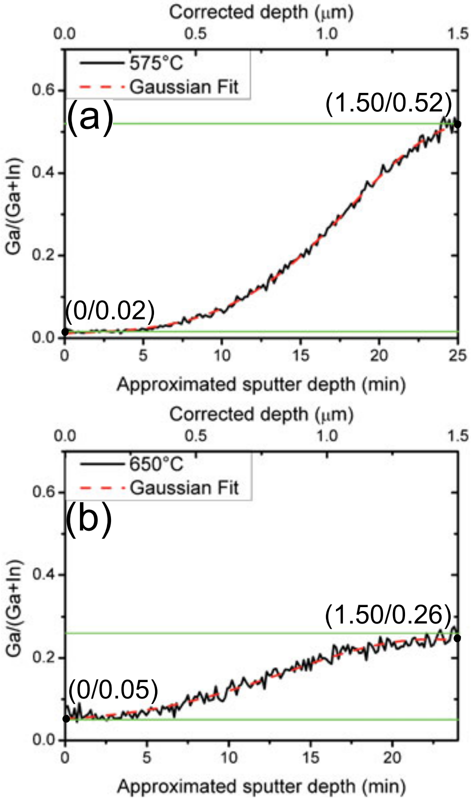

Figure 4.40: Ga/(Ga+In) concentration profiles for the annealing temperatures 575 (a) and 650 (b) on HTG substrates. The data have been fitted by means of Gaussian error function (reproduced from [15] with permission of Elsevier Publishing).

For the SEL process, fast heating ramps (about 200 °C/min) and long holding times at peak temperature (typically 20 min) are used. The difference in the total annealing time for the samples annealed at 575 °C, 600 °C and 650 °C is equal or smaller than 1%. The literature D values are almost two magnitudes higher than the experimental values which are extracted from the SIMS depth profiles 4.14. This is based on different chemical compositions of the two media used in the experiments. In [104, 111] there is fully Ga-free CISe (c_1) on the one hand and fully In-free

CGSe (c_2) on the other hand. The interfaces are furthermore relatively smooth, which leads to more reliable D values. In the experiment the interfaces between the CISe rich and CGSe rich grains are not really smooth and additional defects may lead to reduced D values.

Additionally, the grains consist of different compositions ($\mathrm{CuIn}_{1-x}\mathrm{Ga}_x\mathrm{Se}_2$) with different x-value for the more CISe-like and the more CGSe-like material. As it is schematically shown in the inset of figure 4.42, the layer system consists of an upper CISe-like (dark blue, big grains) and a bottom CGSe-like layer (orange, small grains). The Na doping into the absorber (see figure 4.41) is analyzed because of its relevance for the device quality. The question, into which regions Na diffuses from the glass substrate, does have structural and electronic impacts. By taking a closer look into the depth distribution of the trace elements, one can see a similar behavior for Na and K on both glass substrates (see figure 4.41 black and red lines). On SFG, however, the enrichment of Na or K next to the CIGSe/Mo interface slightly increases with T_{Se} (see figure 4.41 (a)). This observation can be explained by an increased Na diffusion from the SFG matrix with T_{Se}. However, the 600 °C sample has a significantly higher K content towards the front surface and develops a smoother overall K distribution. For the lowest and highest T_{Se}, the Na supply in the intermediate (3E6 Counts for 5-18 min sputter time) region of the absorber and towards the front (1E6 Counts for 0-5 min sputter time) is similar. In the surface region, an increasing Na amount with increasing T_{Se} is observed. The enrichment of Na in the near-surface region can also be influenced by the amount of moisture in the air, which binds the Na. In particular, on the HTG substrates there is a strong enrichment of Na and K next to the CIGSe/Mo interface for lower T_{Se}. This can be explained by the presence of small grains and a high density of grain boundaries in the CGSe and MoSe_2 layers. Furthermore, Na is theoretically soluble in CIGSe up to 1‰, but in reality a total Na content of 1% is often found in the material, which can be explained by Na diffusion along the grain boundaries. As it has been seen before (see figure 4.36), the grain size increases with T_{Se} and therefore the amount of grain boundaries decreases with T_{Se}. Therefore

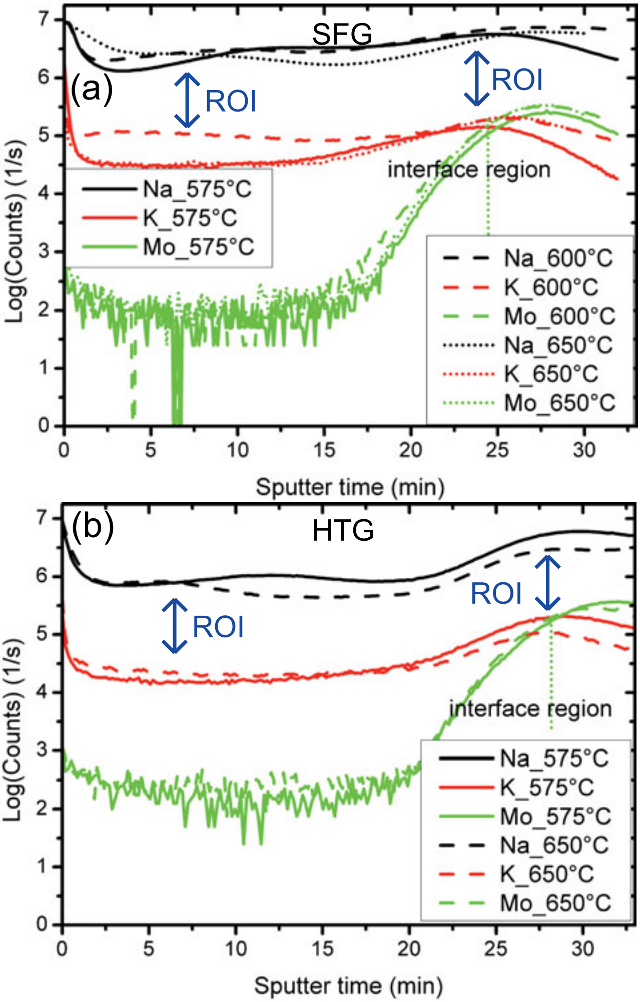

Figure 4.41: Depth-resolved K and Na detection (log values) via SIMS for the case of SFG with three different T_{Se}, the Mo signal serves additional as reference for the CIGSe/Mo interface estimation in (a). For the HTG the depth profiles for 575 °C and 650 °C are collected in (b). The Mo signal is shown in green full lines, dashed lines and with points, which correspond to the different T_{Se} values (reproduced from [15] with permission of Elsevier Publishing).

one can conclude that a strong correlation exists between enhanced Na content in CIGSe and T_{Se} in the process.

In-situ analysis of Ga/In temperature-dependent interdiffusion

For a better insight into the Ga/In interdiffusion inside the absorbers on HTG and their dependency on T_{Se}, in-situ XRD analysis is performed [11, 14]. The Bragg Brentano scan after the selenization process (post-treatment scans) of the SEL in figure 4.42 show an asymmetric reflection profile of the 112 Bragg peaks of the CIGSe phase. The peak becomes narrower with increasing T_{Se} which can be seen by the extracted 2θ values out of each reflection profile 26.92 °/27.46 ° for 575 °C, 26.99 °/27.29 ° for 625 °C, 27.13 ° for 650 °C and 27.14 ° for 675 °C. The two peaks represent the CISe-like (high intense peak) and CGSe-like (low intense peak) regions. The schematic 112 Bragg reflection profile in figure 4.43 (a) at a certain time reflects the integral Ga/In interdiffusion in the CIGSe film. The CISe-like peak position shifts over time in the in-situ XRD scan and looks like the trend in figure 4.43 (b), showing the increasing 2θ angle (decreasing lattice constant) due to Ga diffusion into the CISe rich film.

The time-dependent 2θ angle values in figure 4.44 (a-d) are extracted via a series of Pseudo Voigt fits for each temperature profile. The color code in the reflection maps (see figure 4.44 (a-b)) serves as the third dimension in order to reflect the peak intensity (increasing intensity from white to red [11]).

The 650 °C (see figure 4.44 (c)) and 675 °C (see figure 4.44 (d)) samples have a quite similar angular shift rate, but the absolute 2θ angle is slightly increased as a result of the 25 °C temperature difference. The $2\theta_{112}$ angle of CIGSe is strongly affected by T_{Se}; in particular, the time dependency and maximal value of the peak intensity vary with T_{Se} (see figure 4.44 (e)). The different rate of angular shift over time is attributed to different Ga diffusivity and Na delivery from the glass. However, it is difficult to determine the Ga/In interdiffusion from IXRD scans. The IXRD scans just reflect a decrease in lattice constant, during the annealing procedure. In the time section 200-400 s (see figure 4.44 (e)) the fast heating procedure (section A) occurs. In this region the Ga/In interdiffusion can be explained

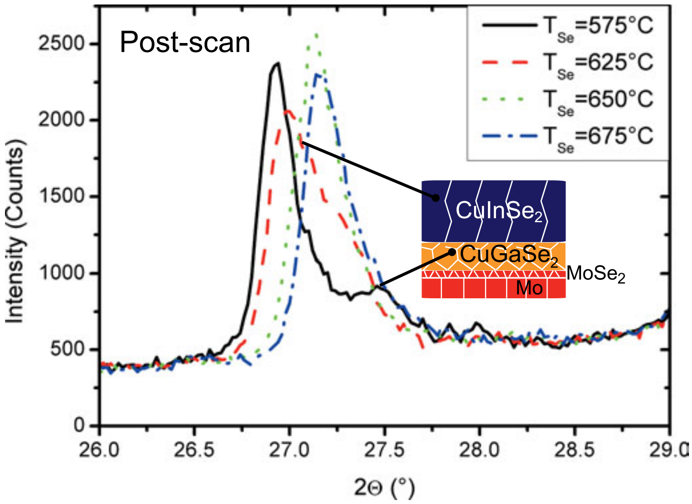

Figure 4.42: XRD post-treatment scans of CIGSe films with different T_{Se}, focussing on the asymmetric 112 reflection profile. The peak profile becomes narrower with increasing T_{Se}, which is explained by an enhanced Ga/In interdiffusion with increasing temperature (reproduced from [15] with permission of Elsevier Publishing).

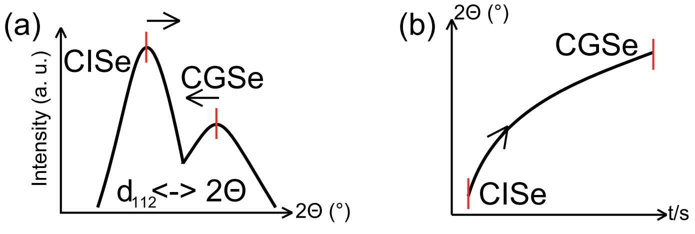

Figure 4.43: (a): Schematic reflection profile of a 112 reflection with a certain degree of Ga/In interdiffusion. (b): The estimated 2θ angles for each diffraction pattern are plotted over time. The 2θ values which are extracted, are approaching 2θ values of Ga containing CIGSe (reproduced from [15] with permission of Elsevier Publishing).

by two quasi planar diffusion fronts with average spacing d_{112}^{CISe} at the top and intermediate region as well as d_{112}^{CGSe} at the bottom region (see figure 4.43).

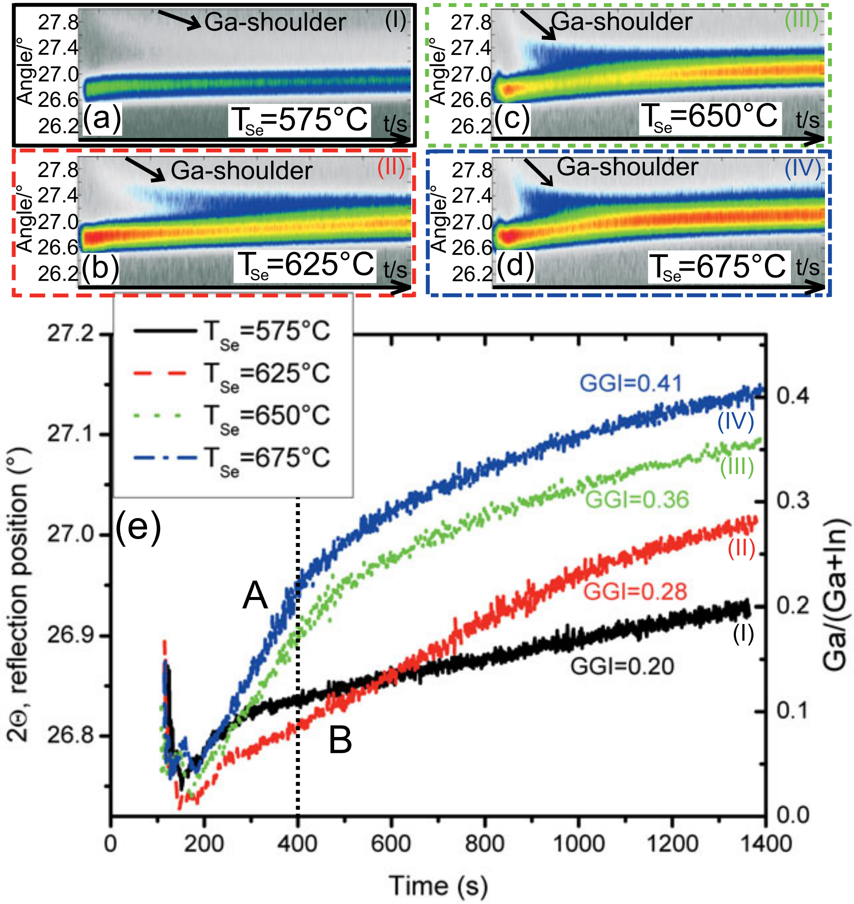

Figure 4.44: In-situ XRD analysis of samples with different T_{Se} for the 112 reflection. The color coded reflection maps are shown from (a-d), where the 2θ angle is plotted vs. time. (e): The extracted 2θ values vs. time are evaluated by a Pseudo Voigt fit (reproduced from [15] with permission of Elsevier Publishing).

In this region the 575 °C and 600 °C curves differ from the curves obtained at a higher temperature in regard to that they show a more abrupt change in the 2θ angle vs. time trend. The time section 400-1400 s (see figure

4.44 (e), section B) is dominated by a slowly linearly increasing 2θ value, which is attributed to a continuous Ga/In interdiffusion process [11]. In order to extract the D values from the experimental evaluated 2θ (or d_{112}) values the Gaussian error function has been used to fit the time dependent trend as explained in section 4.1.2. The estimated D values from in-situ investigations in table 4.14 confirm the trend from the SIMS analysis just in T_{Se} range between 625 °C and 675 °C. The 575 °C sample shows an increased D value in comparison to the other temperatures, which is in accordance with the steep increase of the peak shift rate in the time section between 200-250 s (see figure 4.44 (e)). The D values determined from SIMS profiles are two magnitudes lower than literature values, which can be explained by different experimental conditions. However, the D values extracted from SIMS and IXRD measurements match quite well. The trend of increasing D with increasing T_{Se} can be seen for the CIGSe films on both glass substrates. The D values on SFG is slightly higher in comparison to HTG due to a reduced Na amount in the glass substrate, which inhibits the Ga/In interdiffusion process.

The estimated Ga content (see figure 4.45) is determined from the 2θ angle position by means of Vegard's law. The three most intense reflections of the chalcopyrite crystal are the 112, 220/204 and 312/116. The estimated GGI value from the IXRD measurement increases with T_{Se} and shows a decreasing ratio from the 112 towards the 220/204 and 312/116 reflections (see figure 4.45). The IXRD measurements are performed in-situ at high

Table 4.14: Overview of the D values for the different glass substrates SFG and HTG as well as different T_{Se} evaluated from the concentration profiles and the model of interdiffusion in comparison to literature values. Furthermore IXRD input parameters are fitted with a Gauss error function to estimate D.

T_{Se} (°C)	D^{lit} **[104, 111]** **(cm^2/s)**	D_{SFG} **(cm^2/s)**	D_{HTG} **(cm^2/s)**	D_{IXRD} **(cm^2/s)**
575	4.3E-11	2.9E-13	3.4E-13	1.2E-12
625	4.5E-11	3E-13	-	5.8E-14
650	4.6E-11	4.6E-13	3.7E-13	1.6E-13
675	-	-	-	7.6E-13

temperature and therefore thermal stress as induced by different coefficients of thermal expansions of film and substrate has to be considered. The thermal stress leads to a tetragonal distortion in the crystal and therefore affects the evaluated GGI ratio. The significant difference between the 112 towards 312/116 reflection may result from this additional thermal expansion, which is different for the different crystal planes (112), (220) and (312).

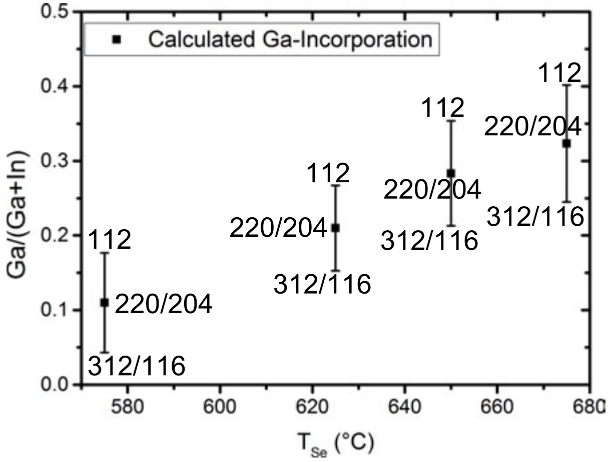

Figure 4.45: Calculated average Ga incorporation by means of the 2θ angle position and the use of Vegard's law (see equation 4.3) for the reflections 112, 220/204 and 312/116. Large differences between the 112 GGI, 220/204 GGI and 312/116 GGI are observed, always with increasing GGI values going from 312/116 to 112 (reproduced from [15] with permission of Elsevier Publishing).

Electronic analysis of the solar cell

In order to analyze the influence of T_{Se} on the electronic properties, three solar cells on two SFGs and on one HTG for five different T_{Se} are compared. The I-V curves are summarized in figure 4.46 for the SFG and HTG substrate. By comparing the trend of the I-V curve between SFG (a) and HTG (b) a similar temperature dependency of the J_{sc} value has been recognized. However the V_{oc} is more strongly influenced by the temperature changes for SFG, which can be directly correlated to the different degree of

Ga/In interdiffusion. A summary of the solar cell performance parameters (with average values "ave") for the samples on SFG (see table 4.15) and HTG (see table 4.16) respectively is shown in the temperature range between 575 °C and 675 °C in comparison to SCAPS simulated values [60, 64, 66]. The experimentally determined GGI profiles from SIMS measurements serve as input data (see figure 4.38) for the SCAPS simulations by transferring the concentration ratios into E_g variations [13]. Here, the CIGSe absorber is modeled by a three layer system, which represents the front, intermediate and back region [13] (introduced in chapter 2.2.4). The total E_g trend is similar for all the five samples, which start with a constant front E_g for a certain depth (front), then a linear increasing E_g follows with different slopes (intermediate) and a constant E_g next to the back contact (back) is adjusted at different levels calculated from the SIMS data. The trend of the SCAPS values follow the experimental trend but there is still a big gap to the experimental values.

For all solar cells produced in this work a loss in V_{oc} ($\approx$ 150 mV) is observed, which is explained by non-optimized post-treatments before the CdS buffer deposition causing defects in the p-n junction region. The FF does not show a significant trend and seems to be relatively independent of T_{Se} (see table 4.15 and 4.16).

Short summary

The CIGSe thin films formed in the high temperature processes show a strong T_{Se} dependency of E_g and Ga/In distribution throughout the film, especially for the SFG substrate. The Ga profile is investigated via ex-situ as well as in-situ methods and an approximate value of D has been determined. The diffusion is modeled with a two layer system consisting of CISe-like and CGSe-like parts. The input parameters are either SIMS Ga/In profiles or time-dependent positions of Bragg reflections from IXRD. The D values estimated from SIMS and IXRD show similar values and the same trend of increasing D with T_{Se}. The grain size in the absorber on a HTG seems to be independent of T_{Se} within the temperature regime from 575 °C to 625 °C. The HTG from Schott shows a better stability and good performance during high temperature processes from the structural point

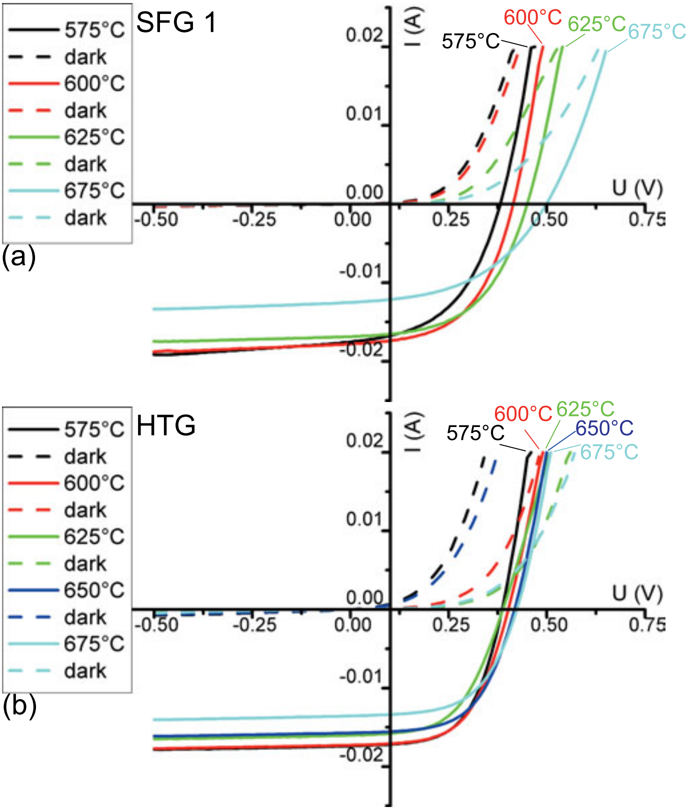

Figure 4.46: (a): Dark (dashed) and illuminated (lines) I-V curves for the different temperatures 575 °C, 600 °C, 625 °C and 675 °C on substrate SFG 1. (b): Dark (dashed) and illuminated (lines) I-V curves for the different temperatures 575 °C, 600 °C, 625 °C, 650 °C and 675 °C on substrate HTG (reproduced from [15] with permission of Elsevier Publishing).

Table 4.15: Solar cell performance parameters (η, V_{oc}, J_{sc} and FF) of CIGSe solar cells on SFG processed with different T_{Se} in comparison to SCAPS simulated values. "Ave" describes the average value of all solar parameters of one sample.

T_{Se} (°**C**)	η (%)	V_{oc} (**mV**)	J_{sc} (**mA/cm^2**)	FF (%)
SFG 1				
575	8.3	381	35.6	61.1
ave	7.8 ± 0.4	374.9 ± 4.9	35.2 ± 0.4	59 ± 2
SCAPS	20.31	559.4	49.04	74.01
600	8.9	418	35.2	49.9
ave	8.5 ± 0.6	408.6 ± 7.2	35.3 ± 0.2	47.6 ± 3.1
SCAPS	21.1	583	49.09	74.11
625	9.2	432	34.4	62.1
ave	8.6 ± 0.5	415.7 ± 11.6	34.3 ± 0.2	60.2 ± 1.8
650	-	-	-	-
ave	-	-	-	-
SCAPS	21.98	617	47.98	74.23
675	8.8	469	31	60.8
ave	8 ± 0.8	457.9 ± 17.6	30.4 ± 0.7	57.5 ± 3.1

of view. Due to the fact that the HTG has an increased amount of Na in comparison to SFG, the diffusion of Na into CIGSe has to be considered in adjusting the optimal E_g profile. During the CIGSe formation on HTG, the Ga/In interdiffusion is significantly reduced in comparison to the absorbers on SFG substrates. Furthermore, there is a slight T_{Se} dependency of K and Na profiles for the SFG and HTG (additionally a constant moisture delivery from the atmosphere might have an impact). The Ga content close to the surface is increased with T_{Se}, which is accompanied by the positive effect of an increasing E_g leading to a V_{oc} improvement. Altogether this leads to an optimized adjustment on the solar spectrum. The V_{oc} values follow a linear increasing trend with T_{Se}, which correlates with the Ga induced E_g increase. However, the J_{sc} follows a more complex trend which cannot only be explained by a reduced absorption of solar radiation due to an E_g increase.

Table 4.16: Solar cell performance parameters (η, V_{oc}, J_{sc} and FF) of CIGSe solar cells on HTG processed with different T_{Se} in comparison to SCAPS evaluated values. "Ave" describes the average value of all solar parameters of one sample.

T_{Se} (°**C**)	η (%)	V_{oc} (**mV**)	J_{sc} (**mA/cm^2**)	FF (%)
HTG				
575	7.9	386	34.7	59.1
ave	4.4 ± 2.1	282.3 ± 78.4	32.8 ± 1.6	44.1 ± 8.3
SCAPS	20.79	571.3	49.07	74.18
600	8	402	34.6	57.5
ave	5.2 ± 1.9	305.7 ± 70.5	33.8 ± 0.8	48.1 ± 6.8
625	6.8	388	32	54.9
ave	4.9 ± 0.8	307.3 ± 43.1	32.9 ± 1.8	48.8 ± 2.9
650	7.6	417	31.4	58.1
ave	7.2 ± 0.3	404.8 ± 11.8	30.7 ± 0.5	58.2 ± 1
SCAPS	21.34	593.3	48.35	74.4
675	6.6	423	27.1	57
ave	5.6 ± 0.6	387.9 ± 26.1	27 ± 0.6	53.7 ± 4.5

4.2 Modification of the Sulfur profile in CIGSSe

This chapter deals with the question how to optimize the optoelectronic properties, especially in the near-surface region, of the CIGSSe solar cell by introducing S/Se concentration gradients. The current setup, a SEL process with evaporated solid chalcogen layers, makes a S post-treatment possible. The chapter starts with a short review of temperature dependent phase formation in the pure CIGS/Mo system. This is followed by the investigation of the effect of simultaneous S/Se supply during the SEL process and its impacts on the structural and electronic properties, especially on the E_g. The chapter ends with the in- and ex-situ analysis of S diffusion into different pre-treated CIGSe thin films to obtain S/(S+Se) (SSSe) graded solar cells. The good time resolution in the analysis of the phase formation via the in-situ XRD setup allows us to investigate the diffusion process with the planar diffusion front model, from which information about the spatial distribution of the diffusing elements can be obtained.

4.2.1 Temperature dependent phase formation

In the following chapter a brief introduction into phase formation of CIGS/Mo in the SEL process is given. The approach is divided into three parts, which deal with the pure CIGS absorber material growth, the back contact properties and the properties of the CIGS/Mo interface. The SEL process with S is performed with the same heating procedure as the one used with Se. In this case a linear heating ramp of 37.7 °C/min until 575 °C (= peak temperature) and a holding time of 3 min at peak temperature is applied. In order to analyze the phase formation in the CIGS system, samples obtained by heating to different temperatures in between 25-575 °C are analyzed ex-situ.

CIGS phase formation

In figure 4.47, the SEM cross sections of different CIGS films with varying temperatures ranging from 200 °C to 575 °C are shown. The CIGS morphology changes from a droplet growth for 200 °C towards a denser film at 500-575 °C. The more droplet-like film in figure 4.47 (a) corresponds to In, S and intermetallics. In figure 4.47 (b), the metallic films correspond to Cu-sulfides with ball-like structure and additional binary sulfide layers below. From figure 4.47 (c) to (e), the CIGS phase formation towards a dense film is visualized by the growing grain size and development of a closed film.

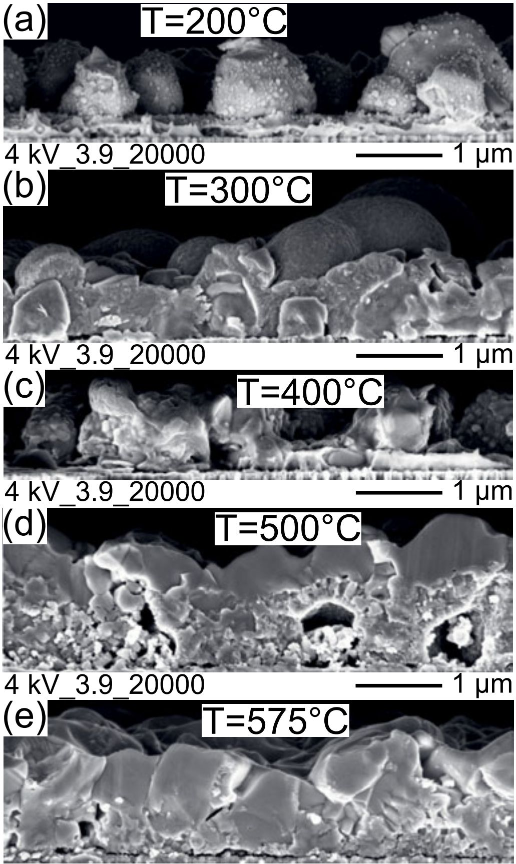

Figure 4.47: (a-e): SEM cross sections of CIGS thin films processed in the temperature range 200-575 °C show different morphologies. The grain structure changes from a droplet growth to a more closed and denser film. For 500 °C a two-layer structure is found with a large grained film on top of a porous structure.

According to XRF measurements, the GGI ratio stays relatively constant (with exception of the 400 °C sample) in the range between 0.28 to 0.34 with T_S over the growth process (see figure 4.48 (a)). The CGI ratio in figure 4.48 (b) is slightly below 1 for all the films except the 400 °C sample, which has a value of approximately 1.1 (might be caused by the presence of a volatile In containing compound in this temperature regime).

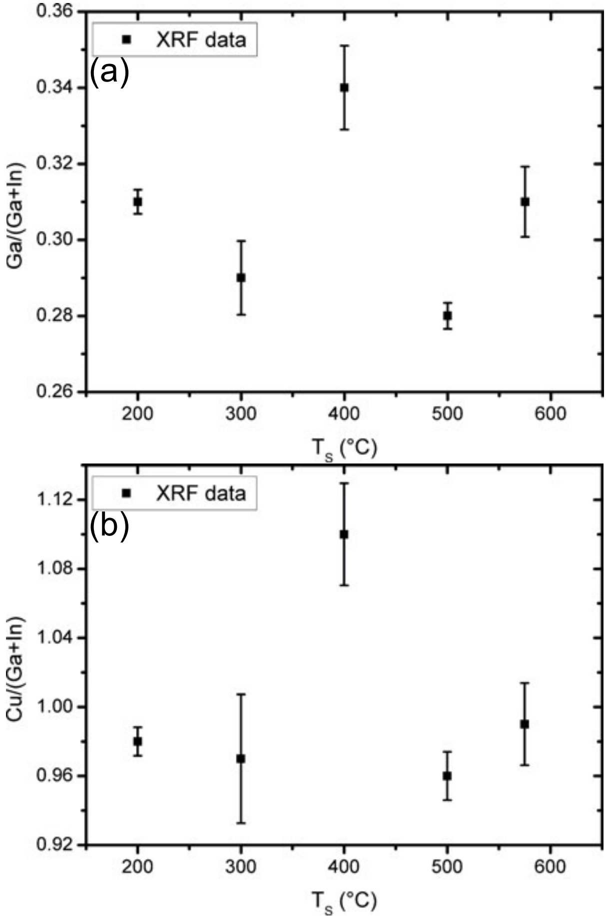

Figure 4.48: GGI (in (a)) and CGI (in (b)) element ratios of CIGS thin films at different temperatures measured via XRF. The 400 °C sample has an increased GGI and CGI ratio compared to the other temperatures.

The drops at 300 °C grow closer together and they are covered by an additional phase, which is identified as CuS containing material according to Raman (see figure 4.49, red 300 °C line) and XRD (see figure 4.50, red 300 °C line) analysis. The rapid CuS growth regime can be observed by the intense A1 CuS mode observed in figure 4.49 (a). For the 500 °C sample a clear double layer structure is observed with additional hole-like regions (see figure 4.47 (d)), which mostly consists of CIGS grains. This is recognized by the presence of 112, 220/204 and 312/116 reflections (see figure 4.50 blue 500 °C line) and by the A1 Raman line (see figure 4.49 (c) blue 500 °C line). Furthermore MoS_2 starts to grow at the absorber/back contact interface identified by weak $10\bar{1}0$ and $11\bar{2}0$ reflections (see figure 4.50 (a)).

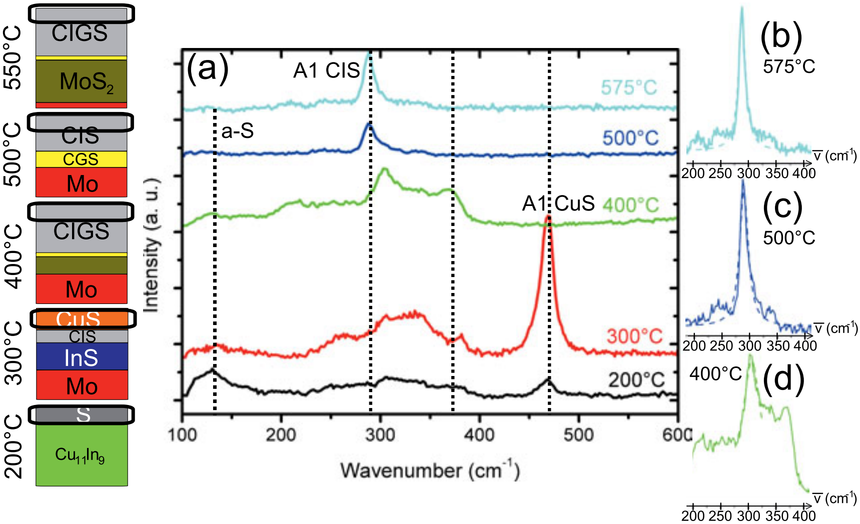

Figure 4.49: The phase formation in the CIGS system schematically is visualized for the different annealing temperatures. The black frame in the schemes on the left represents the analyzed volume. (a): Near-surface Raman analysis of CIGS samples with a clear CuS formation at 300 °C identified by the appearance of the CuS A1 mode. The CIGS growth is clearly identified for the samples annealed to 500 °C by the CIGS A1 mode. (b-d): The CIS A1 mode is observed for the temperature range 400-575 °C; the experimental data are fitted with Voigt profiles.

The degree of asymmetry of the 112 reflection at 575 °C seems to decrease, which indicates an enhanced CGS growth (see figure 4.50 (a) and (b)). Furthermore no CuS modes are present at the highest sulfurization temperature (T_S) according to figure 4.49 (a). The phase formation of CIGSSe with different SSSe ratios is investigated in detail in chapter 4.2.2 together with its impact on the structural and electronic properties of the thin films and solar cells.

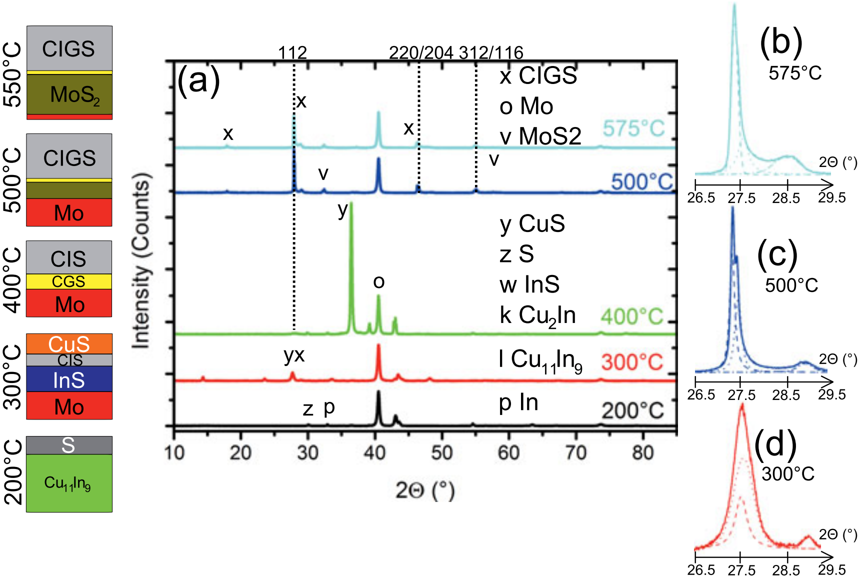

Figure 4.50: (a): Phase analysis via XRD after heating to different temperatures (200-575 °C). A clear CIGS phase is found for temperatures around 500 °C. Between 300 and 400 °C a strong CuS growth is observed by the corresponding reflections. (b-d): The Voigt fits for the CIGS 112 reflections are shown for the 300 °C, 500 °C and 575 °C samples.

Short summary

As in the CIGSe system, strong temperature dependent structural changes are recognized for the CIGS system during the SEL process. However, from material science point of view the shape of the grains are more columnar at lower temperatures in the CIGS system visualized in the SEM cross section images. A pronounced CuS growth is identified at approximately 400 °C according to Raman and XRD investigations.

4.2.2 Influence of different Se to S ratios

In this chapter, the effect of different elemental Se to elemental S ratios on the chalcopyrite phase formation in CIGSSe thin films [142] has been investigated. The influence of different SSSe ratios on the anion incorporation and on the Ga/In distribution is investigated [142]. The results of this chapter have already been published in [12], and are reproduced here with permission of AIP Publishing.

Introduction

For CIGSSe, the anion/cation rule describes the increase of the CB level with GGI ratio and the reduction of the VB level with SSSe ratio [62, 143]. An increase of the GGI ratio towards the back surface reduces the charge carrier recombination rate [29], which is explained by the formation of a back surface field (BSF). In the SEL process, additional S is needed close to the surface to increase the surface E_g [144,145]. In a "classical" SEL process, CGSe growth is kinetically hindered compared to CISe [146] leading to Ga segregation at the back surface. In this part of the thesis a modified process is investigated where adjustable amounts of S and Se are supplied in the form of solid layers, which is compatible with the requirement of a fast and efficient process suitable for industrial application. The influence of different SSSe ratios on the chalcopyrite structure, uniformity, Ga distribution and on the solar cell performance are analyzed.

Structural investigation of the thin film

In the following, the incorporation of S into the absorber films is investigated. XRF has been used to measure the total amount of S in the film. XRD and Raman scattering are sensitive to the incorporation of S into the crystal lattice of the CIGSSe and GDOES analysis gives additionally the depth distribution. The SSSe ratios obtained from XRF are plotted over the evaporated SSSe ratios (here, the SSSe ratio by the relative thickness of the S layer to the total chalcogenide layer thickness is defined), which were measured via a quartz crystal thickness monitor taking into account the different material properties. Figure 4.51 (a) depicts two different sets of experiments with different initial GGI and CGI values (A and B). The sample set A corresponds to samples with a material composition of GGI=0.28, CGI=0.89 and sample set B corresponds to a material composition of GGI=0.29, CGI=0.94. It is apparent that small evaporated SSSe ratios (the smallest evaporated SSSe ratio used is 0.003) lead to much higher SSSe ratios in the XRF resulting in data points above the ideal incorporation line (preferred S incorporation).

Some S can be deposited on the chamber walls during the sulfo-selenization process. Re-deposition of S from the walls may then occur during the following sulfo-selenization processes. This can explain why S is found in the samples even when the S content in the chalcogenide layer is almost zero. However, for higher SSSe ratios the ideal incorporation line is approached (see figure 4.51). In reference [86] a similar phenomenon of different CIGSSe growth regimes for varying SSSe ratios has been discussed. In the following, the S/(S+Se) ratio determined from the XRF results has been used. XRD measurements are performed to distinguish between S incorporation into the back contact and absorber layer. The S incorporation into the back contact can be analyzed by the shifting $Mo(S,Se)_2$ $11\bar{2}0$ reflection with SSSe ratio (see figure 4.51 (b)) and a behavior resemblant of Vegard's law is recognized. Figure 4.52 (a) shows the average interplanar spacing d_{112} as determined from the XRD peak fit vs. the SSSe value determined by XRF. For comparison, theoretical values calculated by application of Vegard's law [29,98] for fixed GGI values of 0 or 1 are shown. In this case an average GGI ratio, obtained by XRF, is used for simplicity.

The d_{112} values are determined by approximating the asymmetric measured peak profiles by a superposition of three Voigt profiles (see figure 4.52 (b)), and then taking the weighted average of the three individual d_{112} values. The reflection shape of the XRD peak changes from the lowest towards the highest S amount. In the following, the SSSe ratios of the absorber evaluated for GGI=0 are used as x-axis, as the reflection shift with S incorporation follows the Ga-poor material. In this case a good correlation between the experimental values and theoretical predictions from Vegard's law has been found. GDOES depth profiling was performed to estimate SSSe and GGI profiles vs. the film depth. The ratio of the

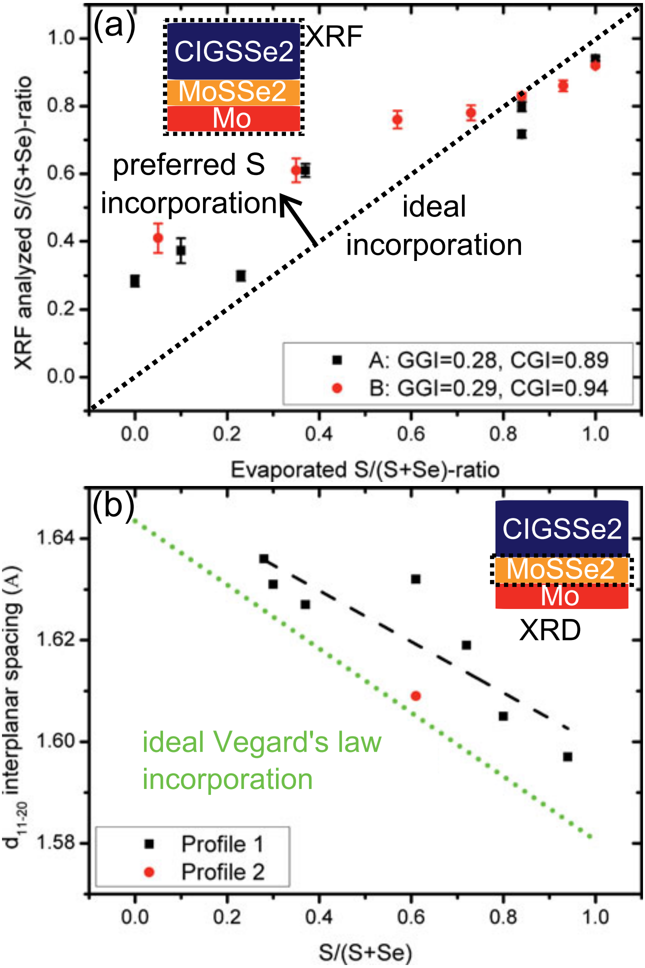

Figure 4.51: SSSe ratios analyzed by XRF of the thin film vs. evaporated SSSe ratio in (a) for experiment A (GGI=0.28 and CGI=0.89) and B (GGI=0.29 and CGI=0.94). Evaluated interplanar spacing d for the Mo(S,Se)$_2$ 11$\bar{2}$0 reflection in (b) by means of Voigt fits. A Vegard's law like shift of the $d_{11\bar{2}0}$ interplanar spacing upon incorporation of S is recognized for the Mo(S,Se)$_2$ back contact (reproduced from [12] with permission of AIP Publishing).

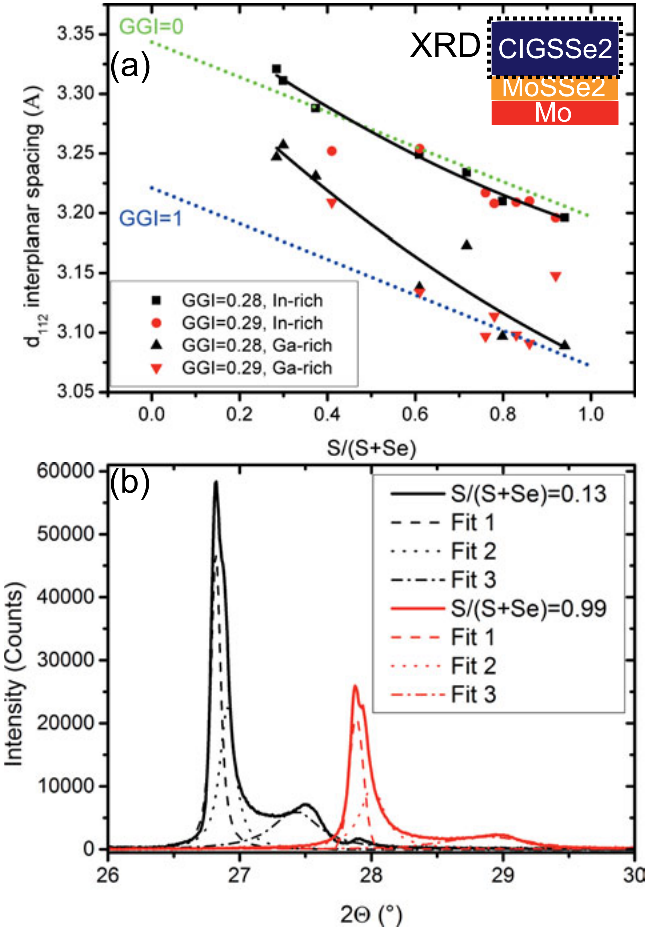

Figure 4.52: Evaluated interplanar spacing *d* for A and B experiments in (a) by means of Voigt fitting for the CIGSSe 112 reflection. The dotted lines show the values calculated by applying Vegard's law for different GGI ratios of 0 or 1. The Voigt fitting procedure is illustrated for two XRD peaks with the lowest and highest S amount in (b), showing a changing 112 reflection shape (reproduced from [12] with permission of AIP Publishing).

emission intensity (EI) of Ga over the intensity of Ga and In together is shown in figure 4.53 (a) and the ratio of the S EI over the total intensity of S and Se in figure 4.53 (b). Due to the lack of suitable calibration samples, these ratios may differ from the GGI and SSSe ratios as defined above. However, one can expect them to be roughly proportional to the true GGI and SSSe values.

In any case, the EI ratios may indicate the absence or presence of concentration gradients of Ga or S in the absorber layer. The absorber thickness was determined by using the position where the Mo signal reaches half intensity of its maximal value (marked by dotted lines). For the different SSSe ratios (0.13, 0.61, 0.99), a homogeneous chalcogen intermixing was found. However, an average GGI value of 0.28 with different SSSe ratios leads to pronounced Ga gradients towards the back contact (see figure 4.53 (a)). This means that the current density gain J^{BSF} through the BSF is expected for all samples. Due to the fact that GDOES is not so surface sensitive for the first 100 nm and XRD gives only the integral information of the absorber, Raman scattering is performed to investigate the surface properties in detail because of their relevance for p-n junction formation in the solar cell device. The A1 modes of CISe (175 cm^{-1} - 200 cm^{-1}) and CIS (290 cm^{-1}) are very sensitive to the SSSe ratio [92] (see figure 4.54). The A1 mode intensity of CISe sharply increases and the A1 mode intensity of CIS decreases with a decreasing SSSe ratio (see figure 4.54 (a)). A relatively constant CIS A1 mode position (vibration of S against the cation sublattice) and a linearly increasing CISe A1 mode position with the SSSe ratio [142, 147] (see figure 4.54 (b)) is observed. This means that an increasing amount of S in the first 100 nm of thin film is followed by a linear Raman shift of the CISe A1 mode due to different SSSe incorporation ratios (attributed to a change in anion sublattice occupation), which makes a fast and exact determination of the SSSe possible.

The microstructural features are visualized via SEM. Cross sections (prepared by Ga focussed ion beam milling) show a systematic morphology change for sets of samples A and B with increasing SSSe ratio (see figure 4.55). The images show that the morphology is influenced by the different anion rather than cation ratios in the samples. Predominantly small grains

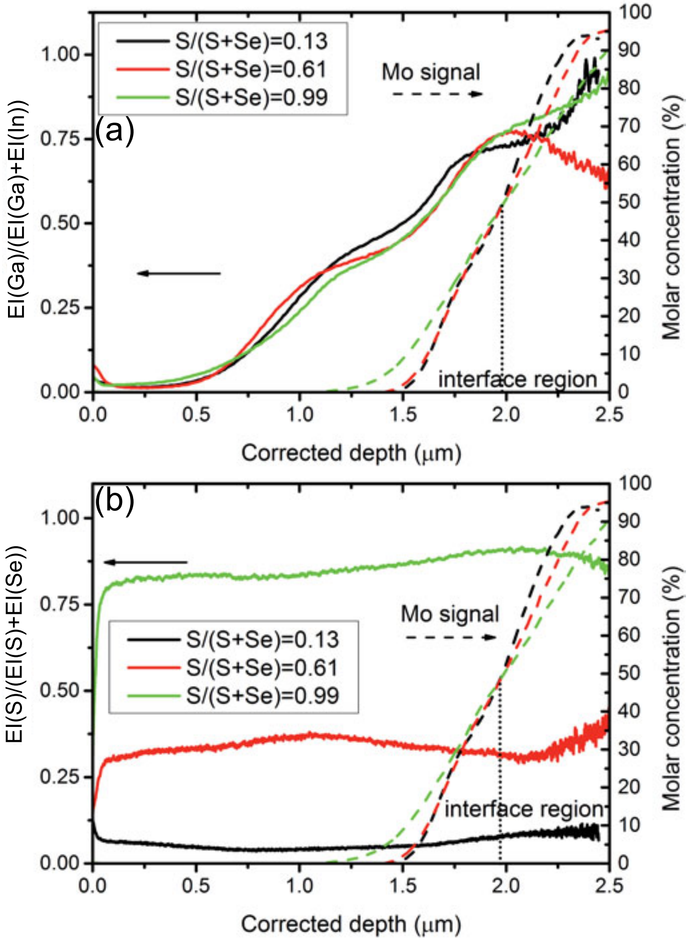

Figure 4.53: GDOES depth profiles for absorbers with different EI ratios $EI(Ga)/(EI(Ga)+EI(In))$ and $EI(S)/(EI(S)+EI(Se))$ respectively. In (a) the $EI(Ga)/(EI(Ga)+EI(In))$ ratio (proportional to the GGI depth profiles) shows a similar Ga concentration gradient towards the back contact with a Ga depleted surface for all samples. In (b) the $EI(S)/(EI(S)+EI(Se))$ ratio (proportional to the SSSe depth profiles) shows a homogeneous S to Se ratio over the whole corrected absorber depth (reproduced from [12] with permission of AIP Publishing).

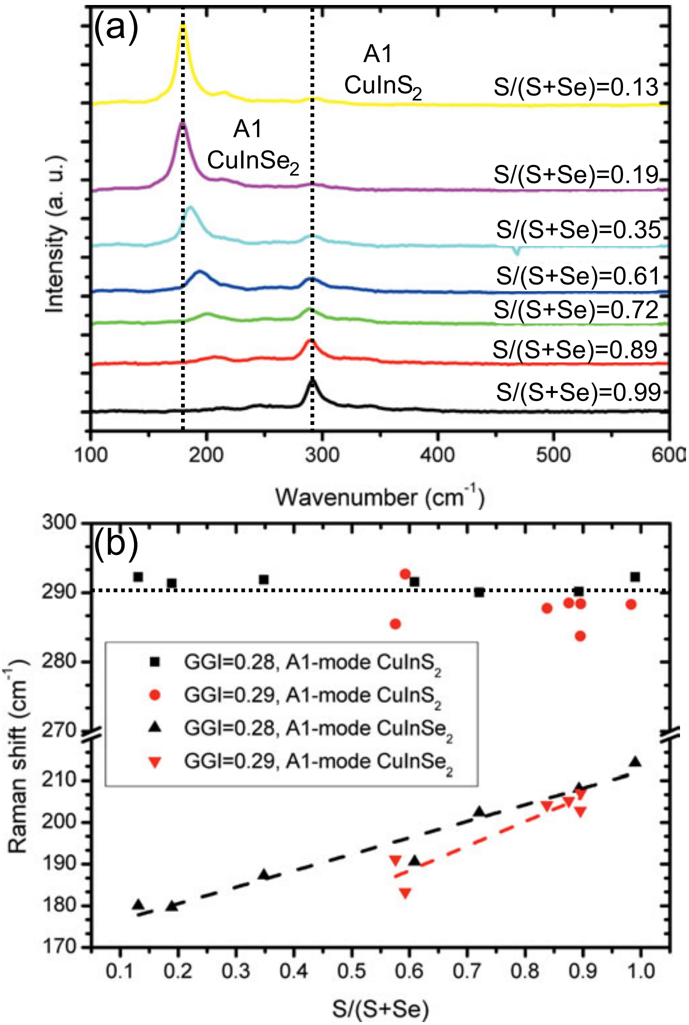

Figure 4.54: Raman spectra of different CIGSSe thin films with varying SSSe ratios ranging from 0.13 to 0.99 are shown in (a). The characteristic CISe and CIS A1 mode shifts are marked in the diagram. The Raman shifts for A1 CuInSe$_2$ and A1 CuInS$_2$ vs. SSSe ratio are shown in (b) with dotted trend lines (reproduced from [12] with permission of AIP Publishing).

at intermediate SSSe ratio have been found for both sets of samples, whereas large grains are formed for very small or very large SSSe ratios. This also affects the roughness of the absorber layer, which may influence the overall cell performance.

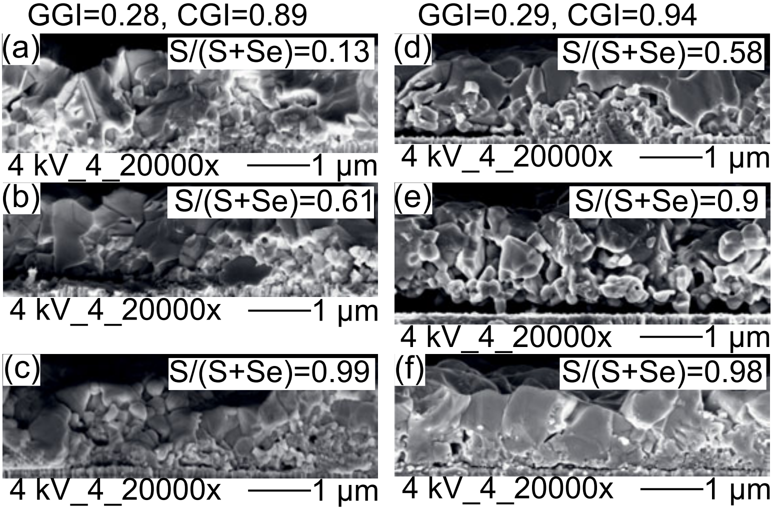

Figure 4.55: SEM cross sections of absorbers with different SSSe compositions, ranging from 0.13 in (a) to 0.99 in (c) for A and 0.58 in (d) to 0.98 in (f) for B (reproduced from [12] with permission of AIP Publishing).

The optoelectronic properties of the thin films were examined via PL. At room temperature and with the current setup the analyzed emission is attributed to the interband transition. With an increasing SSSe ratio, the PL peak maximum shifts to higher energy values due to a higher S incorporation. Additionally, the peak width increases with higher SSSe ratio, which may be attributed to S-induced defects and local E_g fluctuations. At values greater than 0.61, an additional weak emission (see figure 4.56, dashed curves) was detected beside the main PL peak, which indicates the presence of an additional phase. The E_g values have been determined by fitting the asymmetric emission peaks with a superposition of two Voigt profiles, and then taking the weighted average of the individual peak positions (see figure 4.56).

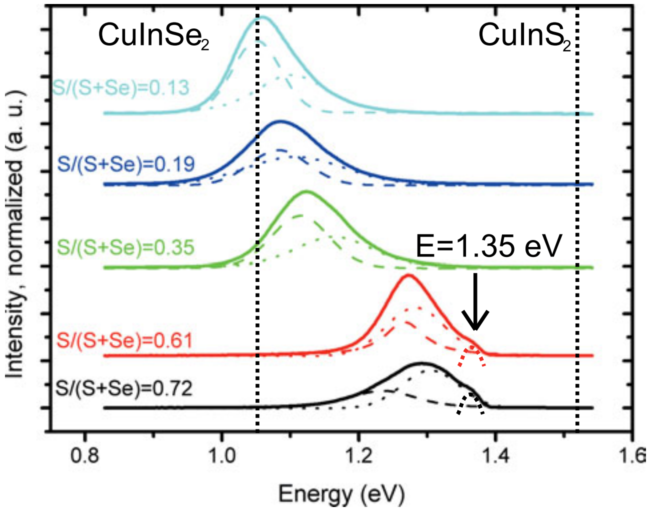

Figure 4.56: PL emission of CIGSSe absorbers with varying SSSe ratios at room temperature. The main PL peak is shifting with increasing SSSe ratio. For SSSe values greater than 0.61 an additional emission is detected at 1.35 eV (dashed curve) beside the main PL peak (reproduced from [12] with permission of AIP Publishing).

Electronic properties of the solar cell

In this part, the results of the electrical characterization of the completed solar cells are presented. An equivalent circuit model is used to extract the relevant cell parameters. For this purpose, EQE measurements and I-V curve measurements under AM 1.5 illumination have been conducted. In addition, the experimental results with theoretical predictions based on the SQ limit are compared. In figure 4.57 (a), EQE spectra are shown. It can be observed that the EQE values for lower SSSe ratios, especially from 0.61 to 0.13, indicates an improved absorber quality. Additionally, the band edge shifts with decreasing SSSe ratio to higher wavelengths. The E_g values from EQE are extracted by calculating the derivative of the spectra and determining the maximal value, which is related to the drop on the low energy wing towards the absorption edge. In figure 4.57 (b), the three dotted lines symobolize the theoretical dependence of E_g [55,58,62,143,148] on the SSSe ratio for different GGI ratios. For comparison, the E_g values obtained from the PL and the EQE data are shown.

The measured E_g values compare quite well with the theoretical data for In-rich material. The optimum values for highest device performance of a single junction solar cell can be estimated from the SQ limit [3, 10]. I-V curves of cells with S-poor, intermediate S amounts and S-rich conditions under AM 1.5 illumination are plotted in figure 4.58 (a) in comparison with the corresponding dark curves (dashed lines), which serve as input parameter for the one diode model fit [50, 51].

Figure 4.58 (b,c) shows the dark I-V curves of two selected cells with low and high SSSe ratios of 0.13 and 0.99, respectively (open squares). For comparison, the fits obtained from the one diode model are also shown. Figure 4.59 (a) shows an almost linear decrease of the J_{sc} with E_g for the investigated cells. For comparison, reference data from National Renewable Energy Laboratory (NREL) cells [137] and the J_{sc} calculated in the limit of the SQ model are shown. The observed trend is attributed to a decreased photon absorption as a consequence of the overall E_g increase.

The J_{sc} is reduced in comparison to the SQ limit due to E_g independent loss mechanisms such as grid shading, surface reflexion, ZnO and CdS absorption and insufficient charge carrier collection [9]. It can be observed that the slopes of the curves are similar. The SQ model predicts a linear increase of V_{oc} from 829 mV to 1213 mV in the range of E_g's considered here (see figure 4.59 (b)). The experimental V_{oc} (499 mV to 678 mV) data also show an increasing trend with increasing SSSe ratios but with a reduced slope. The shift to lower V_{oc} values and the reduced slope of the fit curve in comparison to the SQ limit can be explained by additional loss mechanisms not considered in the SQ model. The reduction of the experimentally determined V_{oc} values in comparison to the SQ model predictions indicates that additional recombination processes play a role.

In principle, interface recombination (IF) becomes important for an increasing CIS-like surface because under illumination this recombination process dominates the device characteristics [149, 150]. However, it is hard to decide which process is dominant on the basis of the present data. In comparison, the NREL V_{oc} trend [137] also shows a V_{oc} increase with E_g

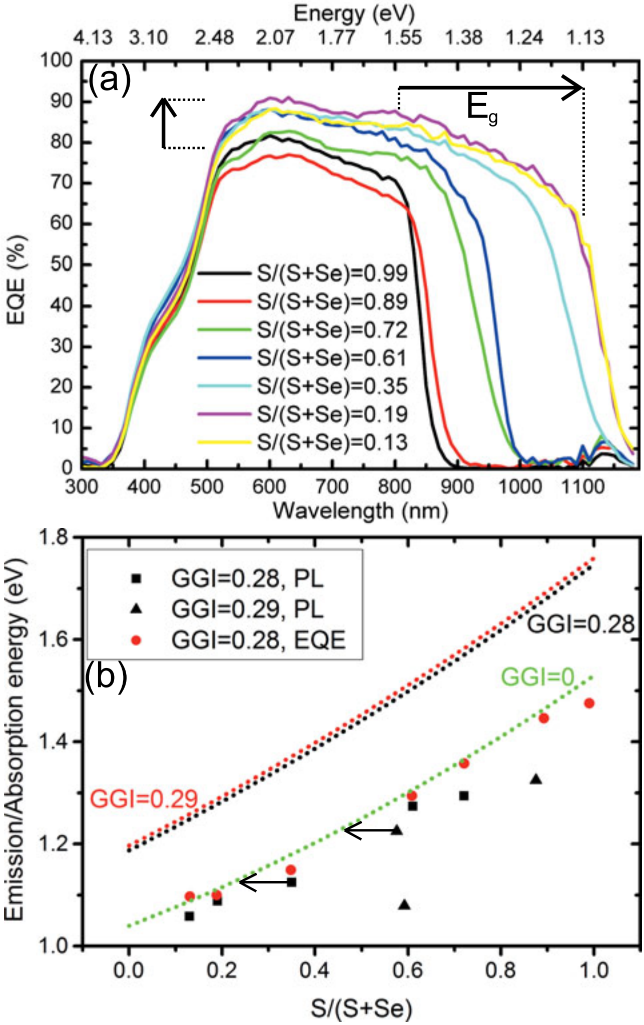

Figure 4.57: EQE measurements of CIGSSe devices showing a shifting absorption edge with different SSSe ratios in (a) according to the S influence on the E_g. The PL emission of the absorbers and the EQE absorption of the devices are illustrated for different SSSe ratios in (b) in comparison to theoretical E_g values (reproduced from [12] with permission of AIP Publishing).

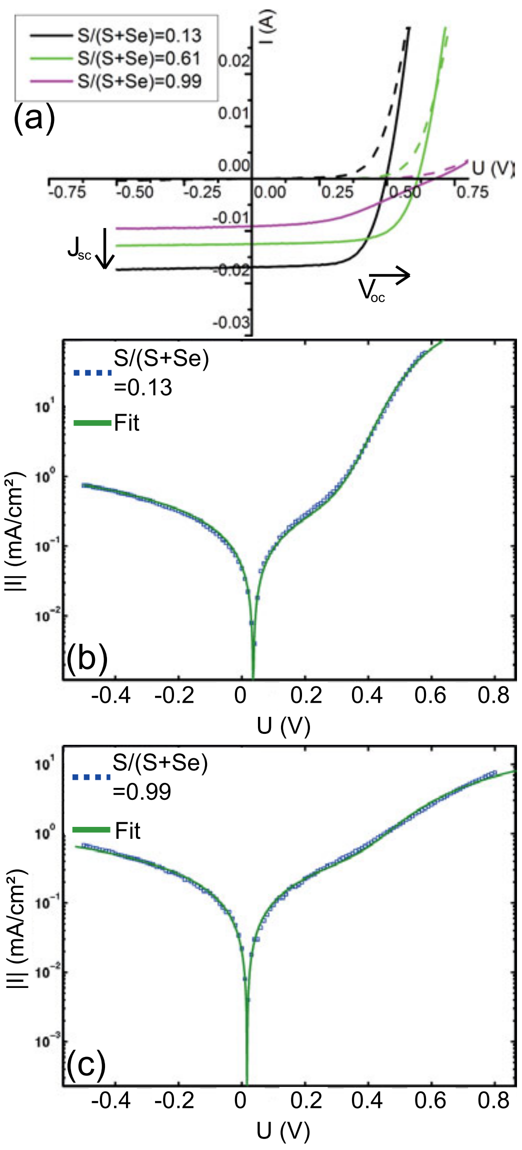

Figure 4.58: I-V curves of the solar cell devices in the dark and under AM 1.5 illumination with different SSSe ratios in (a). The increase in V_{oc} and the decrease in J_{sc} with the SSSe ratios is illustrated for $J(V = V_{oc}) = 0$ and $J_{sc}(V = 0)$. The corresponding raw I-V datas (blue dots) are plotted together with the fits according to the one diode model (green) in log scale for the different SSSe situation 0.13 in (b) and 0.99 in (c) (reproduced from [12] with permission of AIP Publishing).

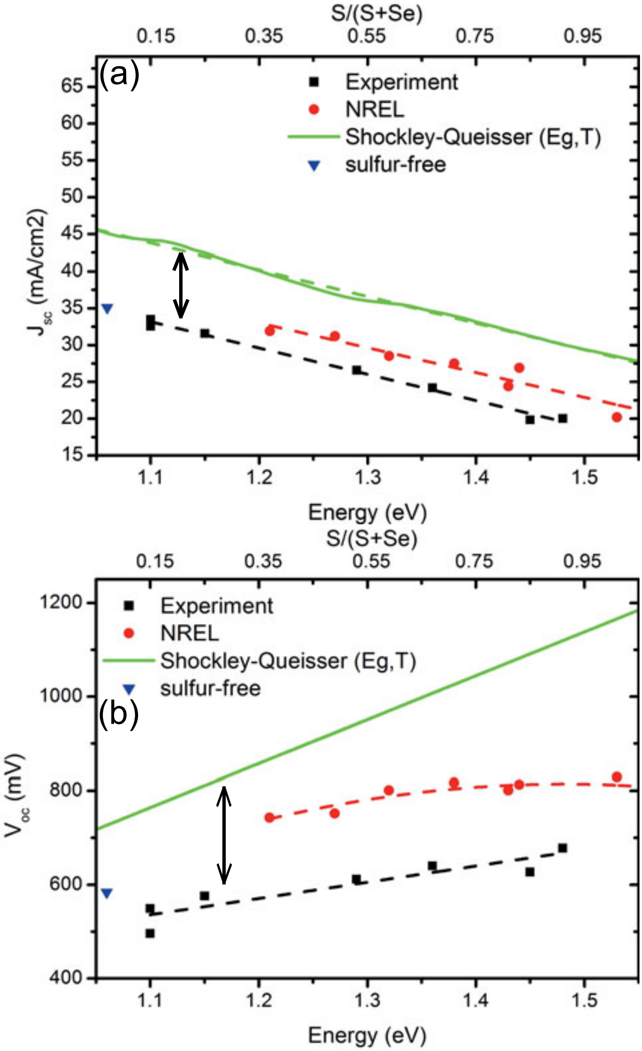

Figure 4.59: J_{sc} of the experimental cells (black squares) in comparison to the NREL cells (red circles) and the SQ calculated theory curve (green line) vs. E_g in (a). V_{oc} of the experimental cells (black squares) in (b). For comparison, the NREL cells (red circles) and the SQ calculated ideal cells (green line) are shown for different E_g values (reproduced from [12] with permission of AIP Publishing).

lower than expected from the SQ model, which is attributed to Ga-assisted defects. SSSe values greater than 0.61 lead to a pronounced reduction in FF (see figure 4.60 (a)), which may in principle result from effects at the back contact absorber interface or from changes at the p-n heterointerface. This reduction is not seen for the NREL cells in [137], where an almost linear decreasing FF with E_g is observed. In Figure 4.60 (b) the η trends of the experimental (squares), the NREL (circles) and the SQ calculated data (line) are compared with respect to their E_g dependency.

The decrease in experimental η can be understood as a consequence of the insufficient compensation of the J_{sc} losses with increasing SSSe by the moderate increase of the V_{oc}. Interestingly, the experimental η and the NREL η show similar trends. For a detailed analysis of the device physics, the one diode model has been used. The only input for the fitting algorithm is the measured I-V curves in the dark and under illumination. The rise in R_s at large SSSe values above 0.6 (see figure 4.61 (a)) may be attributed to the less metallic behavior of the $Mo(S,Se)_2$ as compared to $MoSe_2$ [151] and a changing band adjustment to the CIGSSe at the back surface as a consequence of the decrease of E_g with increasing SSSe ratio [151]. Depending on the SSSe ratio, different kinds of $Mo(S,Se)_2$ mixed crystals are formed at the back contact (see figure 4.51 (b)). But also the band adjustment towards the CdS is strongly influenced by an increasing E_g of the CIGSSe at the front surface according to figure 4.56. In the context of CIGSSe-CdS heterojunction cells the two different kinds of CB discontinuities spike and cliff are introduced to characterize the junction formation [18]. A spike-like junction formation takes place for $E_g < 1.3$ eV and a cliff-like junction formation is present for $E_g > 1.3$ eV respectively [152], which influences the FF of the heterojunction cell. Figure 4.61 (a) shows the R_s, which is connected with FF. A strong increase for SSSe ratios of 0.61 or higher has been found, which corresponds well with the reduction of FF at high SSSe ratios. Figure 4.61 (b) shows the R_p determined from the one diode model, which is connected with recombination processes at surfaces and in the bulk of the absorber. It has been found that the R_p determined from the dark I-V curves first increases with increasing SSSe ratio, but then drops significantly at the highest ratio

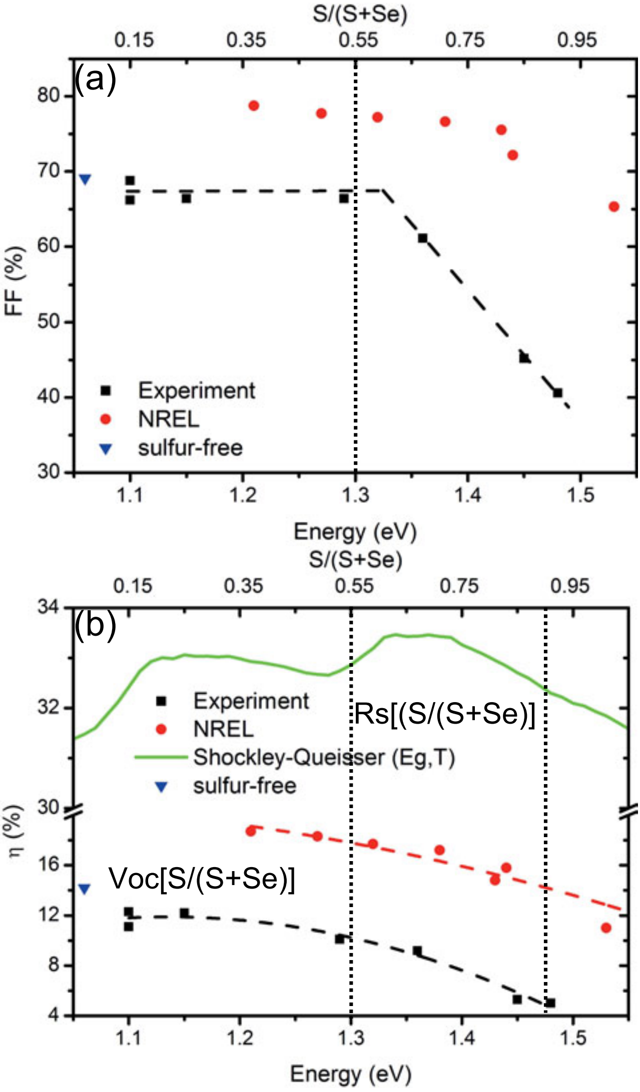

Figure 4.60: (a): The FF of the experimental cells are shown for the different E_g values (black squares) with the corresponding dashed trend lines. (b): The experimental η (black squares) values show a similar trend like the NREL ηs (red circles). The calculated SQ (green line) trend shows the maximal possible η for comparison. The S-free sample serves as reference (triangle) FF and η and for comparison also the FF and η of NREL cells are included (red circles) (reproduced from [12] with permission of AIP Publishing).

of 0.99. However, this trend cannot be observed in the I-V curves under illumination.

In order to investigate the transport and recombination properties of the p-n junction solar cell, the change in n_{id} and J_0 has been investigated. For this purpose the dark curves are used as input parameters because they directly reflect the diode characteristics without any additionally generated photocurrent. In figure 4.62 (a) n_{id} vs. SSSe (circles) is shown in comparison to the S-free cells (triangle). With respect to the error bars, no clear trend of n_{id} can be found. However, all cells show n_{id} values between 1.5 and 2 (see figure 4.62 (a)). Physically, n_{id} describes the deviation from the ideal diode behavior (in the range between 1 and 2) due to recombination processes in the QNR, SCR and IF as well as due to tunneling processes of the majority carriers through the SCR. All recombination processes can occur in parallel but typically one of them plays a dominating role for the V_{oc} limitations [153]. Bulk recombination can be divided into SCR and QNR recombination which will generate a n_{id} of approximately 2 or 1 respectively. The Ga gradient towards the back contact may also cause an increase of the n_{id} by decreasing the QNR recombination rate [153]. In the dark SRH recombinations in the SCR dominate for CIGSSe cells [18, 149, 150]. In principle, temperature-dependent I-V measurements would allow to determine the activation energy of the dominant recombination process, which is either equal (for SRH recombinations in SCR) or smaller (for IF recombinations) than E_g [149, 153, 154].

The J_0 decreases with increasing SSSe (see figure 4.62 (b)) by a factor of two indicating an improvement of junction properties [9], which correlates to the V_{oc} enhancements (see figure 4.59 (b)). The highly efficient reference cells from NREL [155] reach cell efficiencies around 19% and J_0 values in the region of 6E-8 to 4E-7 mA/cm^2 leading to V_{oc} and FF values around 700 mV and 79% respectively. J_0 is based on the minority carrier densities and dependent on the barrier height between the two semiconductor materials responsible for the charge carrier flow [24]. However, the high J_0 values found here in this work can indicate an increasing amount of leakage currents which can be explained by the film morphology; in particular small holes in the thin film may lead to current leakage and non-ideal p-n

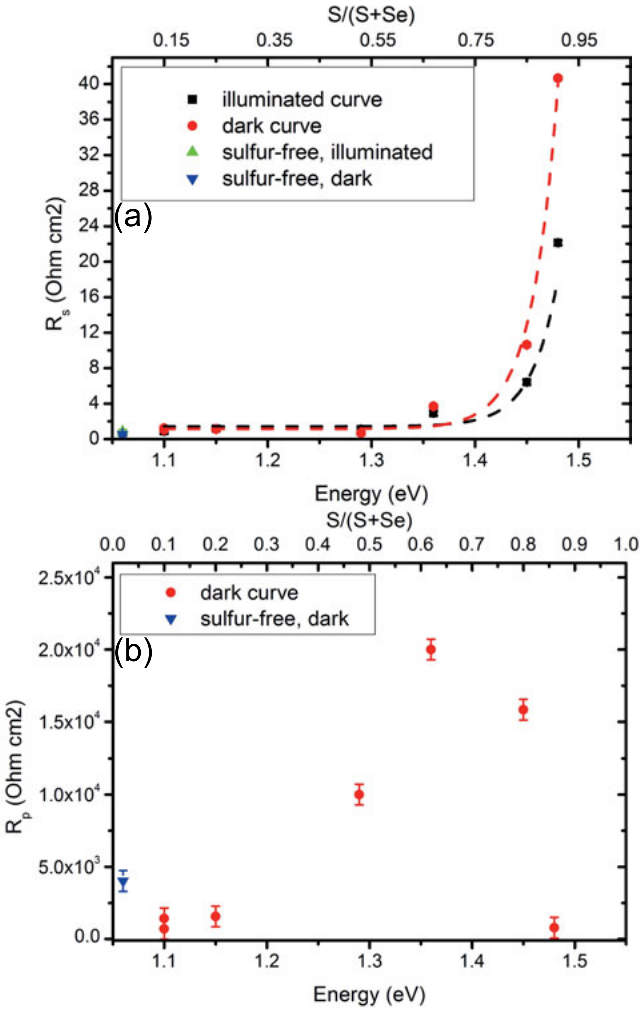

Figure 4.61: (a): The R_s values from the equivalent circuit are shown for different SSSe ratios (black squares and red circles), which were extracted from illuminated and dark curves. For comparison also the S-free values are included (blue and green triangle). (b): The R_p are plotted for different SSSe ratios, which were extracted from the dark curve - also in comparison to S-free samples (blue triangle) (reproduced from [12] with permission of AIP Publishing).

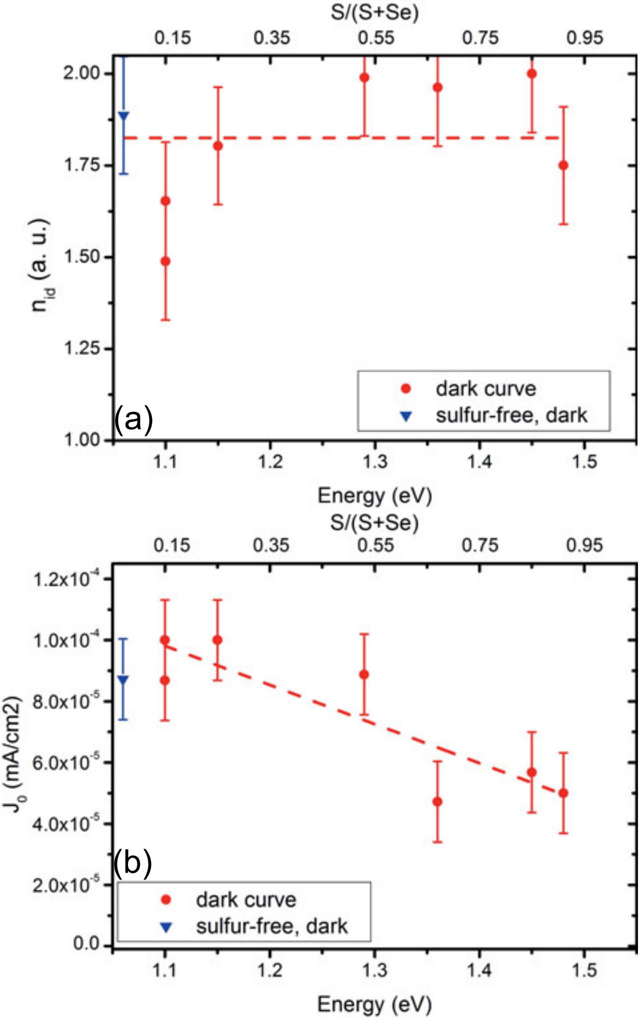

Figure 4.62: The junction properties are well visualized by a saturating $n_{id} \approx 2$ in (a) and a decreasing J_0 in (b) with increasing SSSe supply. The reduction in J_0 can be explained with an E_g dependent V_{oc} increase (reproduced from [12] with permission of AIP Publishing).

junction formation. The coupling of n_{id} and J_0 over equation 4.6 makes an independent determination of n_{id} and J_0 difficult (also indicated by the large error bars in figure 4.62). However, the trends should give an impression of the changing junction properties.

$$V_{oc} = \frac{n_{id} k_B T}{e} \ln\left(\frac{J_{sc}}{J_0} + 1\right) \tag{4.6}$$

The large difference in the V_{oc} values between the results and the best NREL cells may be attributed to a non-optimized post-processing of the absorber structure. Future work must include further optimization of the p-n junction region using optimized post-processing.

Short summary

From the experiments with different SSSe supply, it has been concluded that different degrees of S incorporation have a strong influence on the structural, optoelectronic and electronic properties of the thin films and solar cell devices respectively. The SSSe ratio can be controlled by adjusting the S/Se thickness ratio in the initial chalcogen layer. It was shown by cross sectional SEM studies that the grain morphology changes with the SSSe ratio. The overall chalcogen profile shows a homogeneous distribution in the absorber material which has been proven by structural, optoelectronic and electronic investigations. From a material science point of view, the lattice constant evolution of absorber and back contact with SSSe ratio follow a Vegard-like trend. Additionally, the linear shift of CISe A1 mode with the SSSe ratio indicates a controlled S incorporation in near-surface regions, which is the important region for the p-n junction formation. From an electronic point of view, a SSSe ratio of equal or greater than 0.61 has detrimental effects on the device performance. This is reflected in a strong FF reduction, which is mainly caused by an increasing R_s. A significant enhancement of the V_{oc} values with increasing SSSe ratio has been achieved and values close to 700 mV were observed. However, the rise in V_{oc} for higher SSSe ratios was not enough to compensate for the J_{sc} loss due to the E_g increase. In future work the interface between buffer and absorber has to be optimized for the different SSSe ratios to improve the p-n junction quality.

4.2.3 Ex- and in-situ investigation of sulfur diffusion into CIGSe

In this chapter, the incorporation of S into CIGSe thin films by controlled diffusion has been investigated. For this purpose, the conventional SEL process has been extended by a subsequent S diffusion step. The S gradient is desirable for achieving a graded E_g of the absorber layer, which allows to optimize the absorption properties. The CIGSe incorporation can be influenced by T_S, the S supply (partial pressure) and the temperature of the CIGSe pre-treatment. The presence of binary selenides and small grains enhances the speed of S incorporation. A combination of Raman scattering and in-situ as well as ex-situ XRD has been used in order to obtain detailed information about the diffusion process. The SEL process has been separated into a pure selenization step 1, where the CIGSe film is formed, and a post sulfurization step 2 in order to incorporate a specific amount of S in the CIGSe. The S incorporation occurs at T_S in the range of 575 °C in step 2. The physics of S incorporation into the quaternary material CIGSe strongly depends on microstructural features such as grain size [156], existence of secondary phases [157], CGI and GGI ratio [156,158], T_{Se}, T_S and S supply. Graded absorber films can be grown by incorporating S close to the surface [144]. In the following, results from an extended process sequence are presented which has been designed to achieve a better control of the S incorporation. The results of this chapter have already been published in [11], and are reproduced here with permission of Elsevier Publishing.

Influence of different T_S on the S incorporation into CIGSe

In order to analyze the effect of temperature on S diffusion properties, a process composed of annealing the SEL at 575 °C for 20 min in step 1 followed by S deposition and annealing for 5 min at different temperatures (200 °C, 300 °C, 400 °C, 500 °C and 575 °C) in step 2 has been used. The temperature ramp rate in both steps 1 and 2 is set at 37.7 °C/min. In figure 4.63 the A1 mode shifts of CISe and CIS for different T_S are shown on the left side. On the right side the Raman spectra for each T_S are plotted in detail. The experimental results (see figure 4.63) show that the

A1 mode does not shift with T_S. In [92], CISe crystals were grown by the gradient-freezing method and post-treated by S with the help of chemical vapor transport. The samples produced in that way have different SSSe ratios from 0 to 1 and exhibit a Raman A1 mode shift around 176 cm^{-1} for CISe and 290 cm^{-1} for CIS. If one compares the results with these findings, it can be concluded that no significant amount of S is incorporated under these conditions. However, traces of a CIS peak at 291 cm^{-1} for T_S of 575 °C with 1.5 μm thickness of S layer deposited (S++) has been found indicating a slight S incorporation [142] (see figure 4.63).

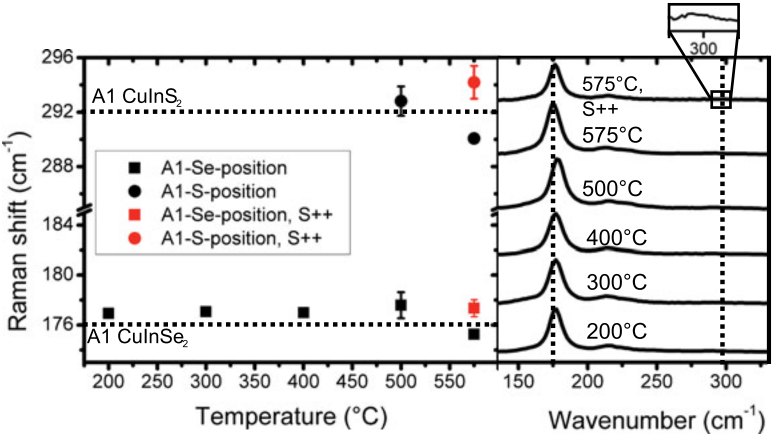

Figure 4.63: Samples annealed at different T_S in step 2 ranging from 200 °C to 575 °C (left side) and with S supply ranging from 0.22 μm to 1.5 μm (S++). The Raman shift and the intensity of the CISe A1 mode do not change significantly (right side). For T_S around 575 °C a low intense CIS A1 mode emerges (in-view image) (reproduced from [11] with permission of Elsevier Publishing).

At first the CIGSe film after step 1 has been studied in order to make sure that the same conditions are present for all the samples out of the sample set before the S treatment in step 2. Figure 4.64 illustrates the 112 reflections of the sample which show the same asymmetric shape for all the samples. The asymmetric peak shape may be separated into a high and low intensity peak with different center positions (corresponding to different lattice parameters), which stands for In- and Ga-rich phases present in the CIGSe material [98]. In-situ analysis in the T_S regime above 500 °C is

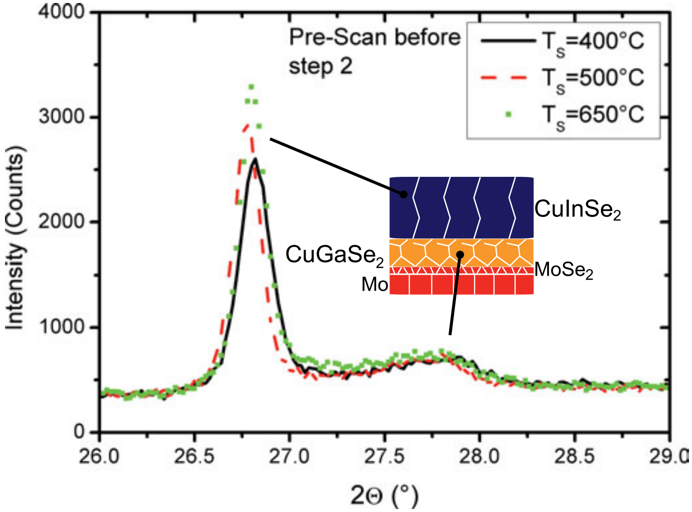

Figure 4.64: XRD peak profiles of the CIGSe 112 reflections before the sulfurization in step 2 showing a nearly identical asymmetric shape for all samples. The peaks are composed of a high and low intensity part corresponding to In and Ga rich phase, respectively (reproduced from [11] with permission of Elsevier Publishing).

performed to get an in-view into S-Se substitution reactions (see figure 4.65 (a-e)). In figure 4.65 (a) and (b), the pure effect of temperature (without S supply) on the Ga/In interdiffusion is reflected in the color maps. From (c) to (e), the effect of an increasing T_S from 500 °C to 650 °C on the 112 reflections of the CIGSSe is shown.

For the 112 reflections a shift to lower 2θ at short times (see figure 4.66 for $t < 200$ s) have been observed, which can be attributed to the thermal expansion of the thin film stack. After that time, different effects have been observed depending on T_S and S amounts supplied (3 μm S layer). As a result, S diffusion into the CIGSe thin film is found between 500 °C (red curve in figure 4.66 (d)) to 650 °C (green curve in figure 4.66 (e)) observed by a shift of the position of the 112 reflections with time. However, the effect of S incorporation is superimposed by the effect of Ga/In interdiffusion further progressing with increasing temperature and time at the annealing temperatures used (see figure 4.66). In comparison

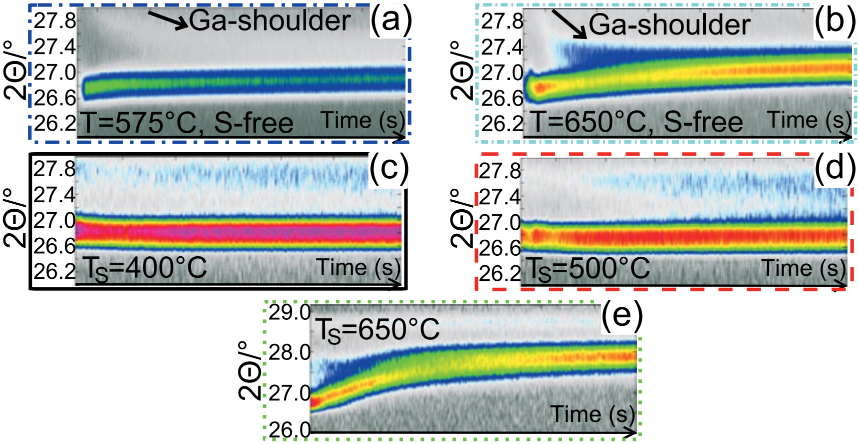

Figure 4.65: Color-coded plots of the 2θ value vs. time for S-free reference samples annealed at 575 °C and 650 °C in (a,b) and samples with 3 μm S layer sulfurized at 400 °C in (c), 500 °C in (d) and 650 °C in (e) (reproduced from [11] with permission of Elsevier Publishing).

with the S-free samples annealed at the same temperature (light blue curve in figure 4.66 (b)), the 112 peak position shifts much faster and to larger angles when S is supplied to the sample.

We conclude that the effect of S incorporation is the dominating effect in the samples with 3 μm S layers (sufficient S supply). The position of the 112 Bragg peaks of the 650 °C sample follows a $\sqrt{t}$ trend, which is interpreted as the result of diffusion-limited S incorporation. As an approximation, a reaction-diffusion layer model has been used, where the CIGSSe reaction layer grows by S in-diffusion and S-Se exchange inside the CIGSe absorber layer [39]. In the Bragg Brentano geometry used here, the whole volume of the film contributes to the 112 reflections. The shift of the 112 peak positions with time corresponds to a change of the average spacing of the 112 planes d_{112} with time due to S incorporation, which can be described by the Bragg equation [142]:

$$d_{112}(t) = \frac{n\lambda}{2\sin(\theta_{112}(t))} \tag{4.7}$$

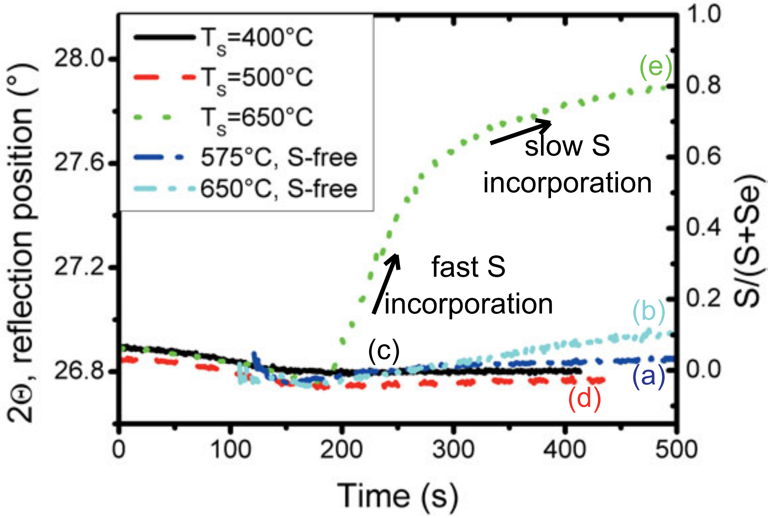

Figure 4.66: Overview of 2θ angle of the 112 reflection vs. time for different T_S and 3 μm of S supplied in step 2 in comparison to the S-free reference samples. The right y-axis shows the estimated S/(S+Se) ratio corresponding to the determined 2θ angle. The determination of the 112 reflection position is performed by a single Pseudo Voigt function fit. Color-coded plots of the 2θ value vs. time of samples with 3 μm S layer sulfurized at 400 °C (d), 500 °C (e), 650 °C (f) and the S-free reference samples annealed at 575 °C and 650 °C in (b,c) (reproduced from [11] with permission of Elsevier Publishing).

The average $d_{112}(t)$ is calculated by taking the volume-weighted average of the d_{112} values for reacted (d_{112}^{CIGS}) and the remaining unreacted (d_{112}^{CIGSe}) parts of the absorber layer in the depth $x(t)$ (see equation 4.8). In this model, the thickness of the reacted layer x can be calculated from the value of d_{112}(t) according to equation 4.9. In the first approximation, this thickness is taken as the average diffusion depth at time t, which allows us to estimate the D for S in-diffusion according to equation 4.10 (we assume that S diffusion is the rate-limiting step of the reaction) [39]. The maximal possible S diffusion length into the absorber is equal to the vertical absorber thickness $L = 1.5\ \mu m = x(t = t_{end})$.

$$d_{112}(t) = \frac{d_{112}^{CIGS} \cdot x(t) + d_{112}^{CIGSe} \cdot (L - x(t))}{L} \tag{4.8}$$

$$x(t) = \frac{L \cdot \left(d_{112}(t) - d_{112}^{CIGSe}\right)}{d_{112}^{CIGS} - d_{112}^{CIGSe}} \tag{4.9}$$

$$D = \frac{x(t)^2}{2t} \tag{4.10}$$

This leads to a calculated S penetration depth for exemplary different sulfurization times $x(\Delta t = 10\ s) = 1414$ Å, $x(\Delta t = 100\ s) = 9574$ Å and $x(\Delta t = 200\ s) = 11583$ Å. In summary it can be stated that after 200 s reaction time S has penetrated more than 83% of the thin film. The diffusion coefficient for the S diffusion into the CIGSe layer is estimated as $D^S_{CIGSe} = 2.9 \cdot 10^{-11} \frac{cm^2}{s}$ according to equation 4.10. In literature a variety of D values of S in CISe and CIGSe respectively are reported, mostly with the help of co-evaporation and subsequent H_2S treatment for slightly Cu-poor as well as Cu-rich material (see table 4.17). In [159], CISe single crystals are sulfurized in a H_2S-Ar mixture at 575 °C which leads to $D^S_{CIGSe} = 10^{-16} \frac{cm^2}{s}$. In general, single crystals display a lower limit in the case of element diffusion and therefore serve as the lowest estimation of D^S_{CIGSe}. Article [157] summarizes bulk and grain boundary diffusion coefficients (D and D_B) in the temperature regime of 450-500 °C and the annealing regime of 20-60 min resulting in D ranging from $1.2 \cdot 10^{-12} - 6 \cdot 10^{-12} \frac{cm^2}{s}$ [160] and D_B ranging from $2.5 \cdot 10^{-10} - 5 \cdot 10^{-10} \frac{cm^2}{s}$. Reference [158] presents a D of almost "single phase" crystals with $3 \cdot 10^{-13} \frac{cm^2}{s}$ for slightly Cu-poor and $1.5 \cdot 10^{-11} \frac{cm^2}{s}$ for slightly Cu-rich samples at the annealing temperature 575 °C. Slightly Cu-rich CISe material displays, based on the diffusion properties of the secondary CuSe phase, an upper boundary of D^S_{CIGSe}. Considering the fact that the absorber layers are polycrystalline, the estimated D value for the S diffusion falls well into the range of the literature data for S diffusion into polycrystalline CIGSe.

Table 4.17: Overview of a variety of experimentally determined D values for sulfurization of absorbers with different temperatures, material and process conditions.

Process	**material**	T $(^{\circ}C)$	D (cm^2/s)
H_2S [159]	single crystals	575	10^{-16}
H_2S [157]	polycrystalline	400-500	$1.2 - 6 \cdot 10^{-12}$
[158]	single crystals	575 Cu-rich	$1.5 \cdot 10^{-11}$
[158]	single crystals	575 Cu-poor	$3 \cdot 10^{-13}$

CIGSe pre-treatment

In recent articles [145, 156] it has been shown that the properties of the base material CIGSe are relevant for the diffusing species S. With the help of T_{Se} in step 1 the grain size and the amount of binary selenides are adjusted in utilizing the information about the phase formation in the SEL process [84]. The binary selenides are supplied by the growing CISe and CIGSe respectively according to equations 4.11 and 4.12 [84].

$$Cu_2Se + In_2Se_3 \rightarrow 2CuInSe_2 \tag{4.11}$$

$$Cu_2Se + Ga_2Se_3 \rightarrow 2CuGaSe_2 \tag{4.12}$$

For a further analysis of S dependent diffusion, samples with different degrees of CIGSe to binary selenide ratios are grown (T_{Se} between 300-400 °C) which are annealed at a T_S of 575 °C for 5 min in step 2. In figure 4.67 (a) the corresponding GIXRD profiles under different angles of incidence α are shown. Schematically the penetration depth x of X-rays into the CIGSSe material depending on α is presented in figure 4.67 (b).

In figure 4.68, the 2θ values of the 112 Bragg reflections vs. T_{Se} are shown for different α values. The $2\theta_{112}$ values are determined by analyzing the asymmetric measured peak profiles by a superposition of two Voigt profiles and then taking the weighted average of the individual $2\theta_{112}$ values. The right axis also shows the estimated SSSe ratio for the corresponding 2θ value according to Vegard's law. With the help of GIXRD analysis depth resolved diffraction patterns [98] can be obtained showing a decreasing 2θ

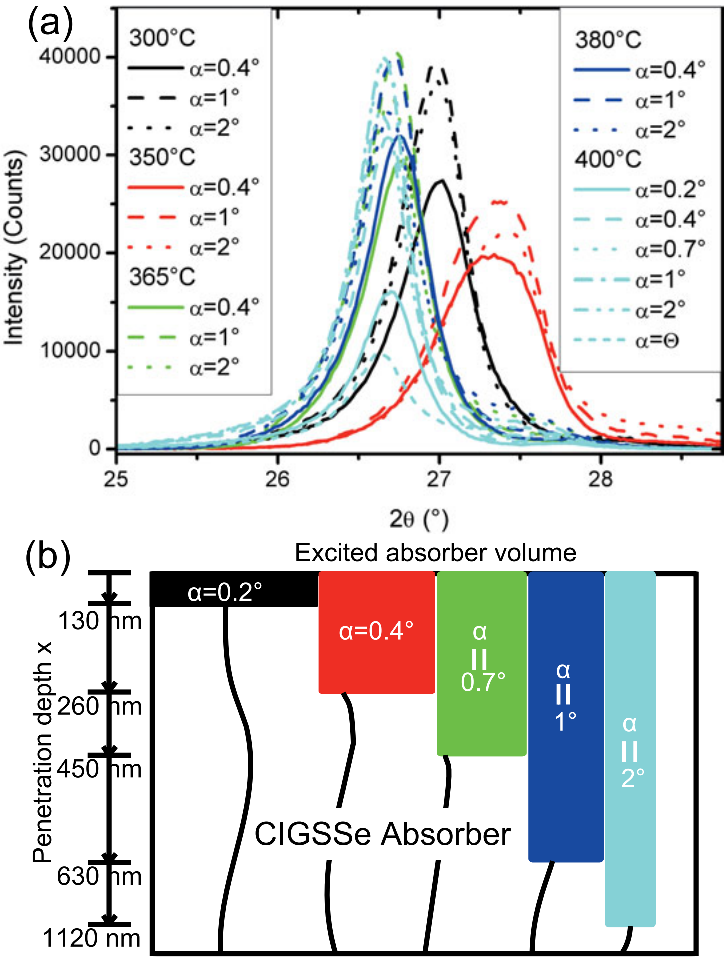

Figure 4.67: The GIXRD profiles of the 112 reflection is shown for different T_{Se} in (a) and the varying α's are expressed by lines, dashed lines and dots (reproduced from [11] with permission of Elsevier Publishing). The penetration depth of X-rays into the CIGSe material with varying α is visualized schematically by the position of the color bars, respectively in (b). The analyzed sample surface area is higher for smaller incident angles, which is related to the setting of the aperture in the GIXRD measurement.

angle of the 112 reflections with increasing T_{Se} (black to magenta data points). Additionally, the composition ratio SSSe is measured via XRF to prove that the reduced lattice constant does not arise from different initial compositions from sample to sample (see table 4.18). With the help of the XRF together with GIXRD results one can conclude that S incorporation is reduced with increasing T_{Se} (see figure 4.68, also confirmed via Raman, XRF and PL).

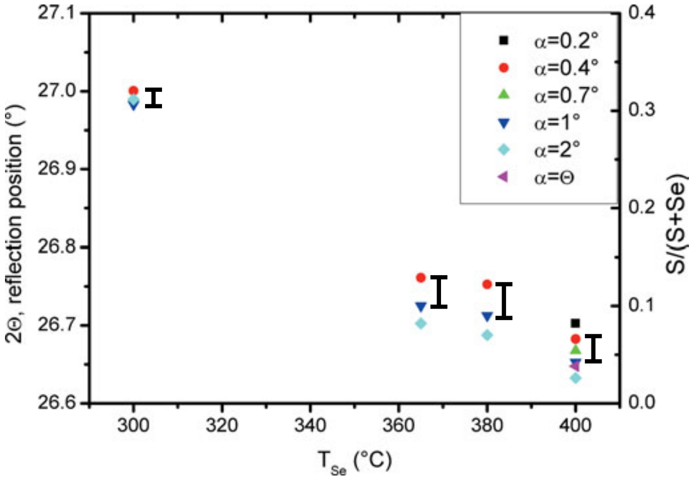

Figure 4.68: The 2θ position of the 112 reflection vs. T_{Se} for different incident angles α showing a decreasing 2θ value with T_{Se}. The data points are extracted with the help of an average function of two Voigt fits. The approximated SSSe ratio out of the 2θ position is shown on the right axis (reproduced from [11] with permission of Elsevier Publishing).

The penetration depth $x(\alpha)$ of X-rays in the GI geometry strongly depends on the incident angle α with values around $x(\alpha = 0.4\,°) \approx 0.26\ \mu$m,

Table 4.18: Overview about the elemental composition ratios GGI, CGI and SSSe for different temperatures determined via XRF.

T ($°C$)	GGI (a. u.)	CGI (a. u.)	SSSe (a. u.)
300	0.35 ± 0.004	0.97 ± 0.01	0.34 ± 0.01
365	0.31 ± 0.004	0.85 ± 0.01	0.31 ± 0.02
380	0.3 ± 0.004	0.86 ± 0.01	0.3 ± 0.01
400	0.3 ± 0.01	0.85 ± 0.02	0.27 ± 0.01

$x(\alpha = 1\,°) \approx 0.63\ \mu$m and $x(\alpha = 2\,°) \approx 1.22\ \mu$m (according to chapter 3.2.1 and table 3.1). The Ga/In interdiffusion cannot play a major role for the 112 reflection shifts because the step 2 treatment (sulfurization step with $575\,°C$ for 5 min) is identical for all samples of this series. With increasing the incident angle α from $0.2\,°$ to θ_{112} the $2\theta_{112}$ angle position decreases (see figure 4.68, black to magenta points) which qualitatively shows an increasing lattice constant in the deeper lying regions of the absorber which contribute more for larger incident angle. Additionally the difference in $2\theta_{112}$ angle position for $\alpha = 0.4\,°$ and $1\,°$ is larger for the 400 °C in comparison to 300 °C sample, which is a hint for a varying degree of S diffusion in the different CIGSe pre-treated layers. This can be attributed directly to the different amount of binary selenides left in the thin films before the start of the S post-treatment.

Special CIGSe pre-treatment temperature regime around 350 °C

The quantitative depth resolved GIXRD measurements indicate that in the temperature range $300\,°C \leq T_{Se} \leq 400\,°C$ (condition of selenization step 1) the S incorporation in step 2 is strongly influenced. With the help of in-situ XRD, the S diffusion rate for different T_S and varying S supply, either with 3 μm Se layer or S supply in excess, are analyzed in detail. For this purpose four different samples I ($T_S = 575\,°C$ and 3 μm S), II ($T_S = 575\,°C$ and 3 μm S + excess), III ($T_S = 650\,°C$ and 3 μm S) and IV ($T_S = 650\,°C$ and 3 μm S + excess) are produced (see figure 4.69).

A shift of the 112 reflection over time shows the influence of increasing T_S from 575 °C to 650 °C as well as the S excess (see figure 4.70, black to blue). The different offsets in the 112 reflection positions at the S interaction regime at 200 s arise from slight differences in height of the mounted samples during the annealing from sample to sample. The 650 °C with 3 μm S sample shows a similar 2θ trend as described before which is a sign for a diffusion controlled S incorporation (green curve in figure 4.70). However, the CIGSe thin film at 350 °C also contains binary selenide residues. In region A, the 2θ trend can be described by the phase formation of binary selenides towards sulfo-selenides, CIGSe or CIGSSe. Region

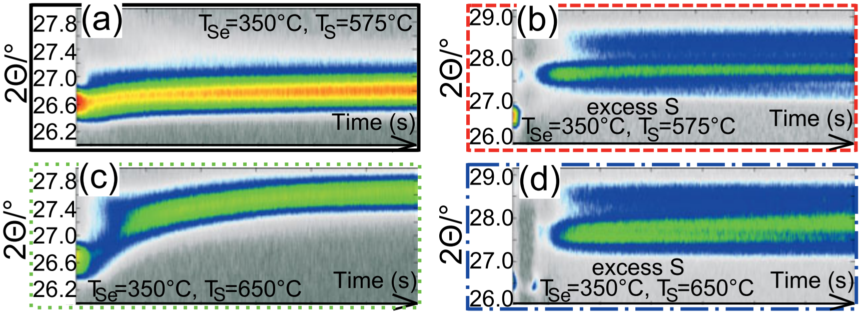

Figure 4.69: Color coded reflection maps as output data from IXRD measurements showing the 2θ angle shift vs. time. An additional reflection is determined next to the main 112 reflection due to the formation of $CuIn_5S_8$ phase in (b,d) (reproduced from [11] with permission of Elsevier Publishing).

B is characterized by the S-Se exchange reactions in the CIGSe and the remaining sulfo-selenides towards CIGSe or CIGSSe.

Region C is dominated by the Ga/In interdiffusion in CIGSSe, which is found by comparison to the 650 °C reference sample (see figure 4.70, magenta). The 575 °C, S++ and 650 °C, S++ curves follow an instantaneous S in-diffusion trend whereas no ”controlled” S-Se reaction takes place (see figure 4.70, red and blue). The 2θ angle shifts abruptly after 200 s and a diffusion controlled S incorporation such as for the 650 °C (green dotted line) sample is not observed. Via ex- and in-situ XRD measurements (see figure 4.70, 4.71) the appearance of a secondary phase (defect spinel $CuIn_5S_8$) is identified [161]. In figure 4.71 the Bragg-Brentano scans of the CIGSSe samples after the annealing step 2 are shown. The CIGSSe phase is identified by the XRD 112 reflection position of the more Se-like (black line) and S-like (green dotted) chalcopyrites. The spinel-like phase is identified by the appearance of the 1-5-8 XRD peak, which belong to the $CuIn_5S_8$ phase, and the reduced CIGSSe 112 peak intensity (FWHM is increased). In the color-coded reflection map in figure 4.69 (b) and (d) respectively (red and blue frame) the $CuIn_5S_8$ 222 reflection appears at $2\theta = 28.5\,°$ next to the main 112 CIS reflections at later annealing times because the system tries to absorb higher S amounts.

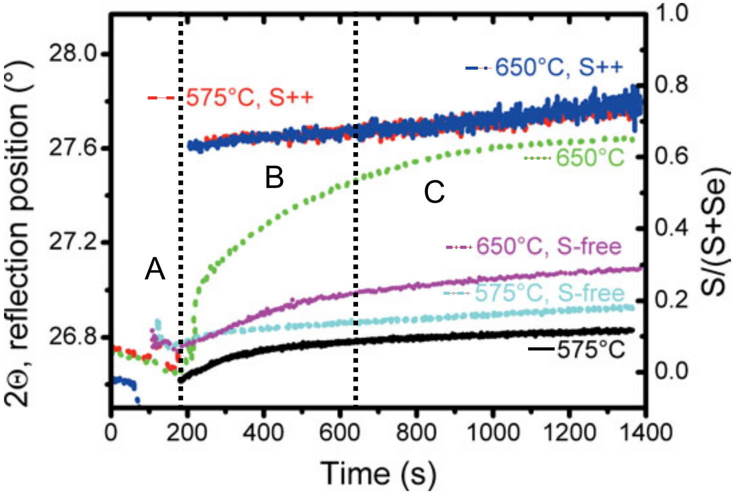

Figure 4.70: 2θ values extracted from the 112 reflection profiles of the color-coded reflection maps. The right axis shows the SSSe ratio estimated from the experimental 2θ angles. A slight 2θ shift for $T_S = 575\,^\circ\mathrm{C}$ (I, black), an instantaneous 2θ angle shift for $T_S = 575\,^\circ\mathrm{C}$ and S excess (II, red), a moderately increasing (diffusion controlled) 2θ shift for $T_S = 650\,^\circ\mathrm{C}$ (III, green) and an instantaneous 2θ shift for $T_S = 650\,^\circ\mathrm{C}$ and S excess (IV, blue) are observed (reproduced from [11] with permission of Elsevier Publishing).

With equation 4.9 the penetration depth of S in the second step is estimated as $x(\Delta t = 10\ s) = 2090$ Å, $x(\Delta t = 100\ s) = 4021$ Å and $x(\Delta t = 1000\ s) = 9461$ Å. In this case S needs 1000 s to penetrate through 63% of the thin film. Furthermore the D is estimated according to equation 4.10 as $D^S_{CIGSe} = 1.1 \cdot 10^{-11} \frac{cm^2}{s}$, which again represents an average D value of grain boundary diffusion and grain diffusion parts. Surface analysis via Raman scattering determines an A1 mode shift of CISe with T_S (values higher than 184 cm^{-1}, see figure 4.72 (a)) to higher energies due to an increased S incorporation in the anion sublattice [92]. A shoulder-mode at 318 cm^{-1} is noticed for the sample with excess S supply which corresponds to $CuIn_5S_8$ [161] (see figure 4.72 (b)).

In figure 4.73 (a)-(d) the SEM cross sections of the four samples I, II, III and IV are shown. The grain size is increased from (a) to (c) because

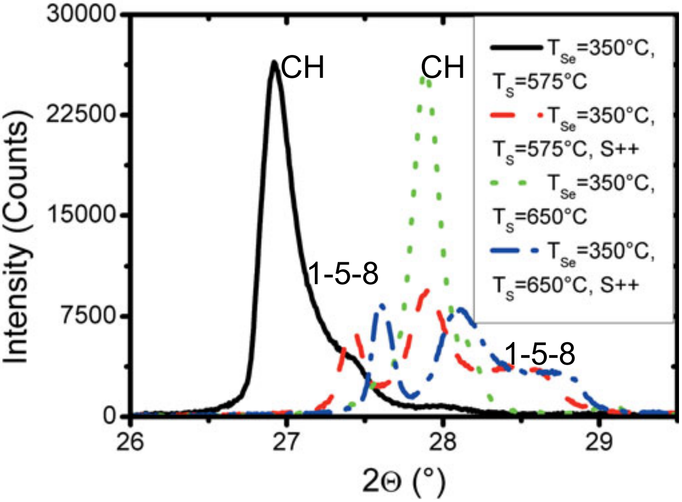

Figure 4.71: Bragg Brentano scan of the finished CIGSSe samples (after step 2) with the different sulfurization conditions 575 °C (black line), 575 °C plus S excess (red dashed), 650 °C (green dotted) and 650 °C plus S excess (blue dash dotted). CH corresponds to CIGSSe related XRD peaks (black line: more Se-like, green dotted: more S-like) and 1-5-8 represents XRD peaks (red dashed and blue dash dotted: more spinel-like) which belong to the $CuIn_5S_8$ spinel phase (reproduced from [11] with permission of Elsevier Publishing).

of the increased temperature in step 2. From a morphological viewpoint S in excess leads to small grains in SEM cross sections, which is identified by comparing (a) with (b) and (c) with (d). Additionally, one gets the impression that the layer thickness (see figure 4.73 (b,d)) of the thin film is reduced under S in excess, which can be explained by the evaporation of certain Se-species. This behavior is also described in [162] where a two-step mechanism of S incorporation is introduced in a way that at first a chalcogen exchange reaction of the solid-gas interface occurs, followed by an S diffusion in and Se diffusion out of the film.

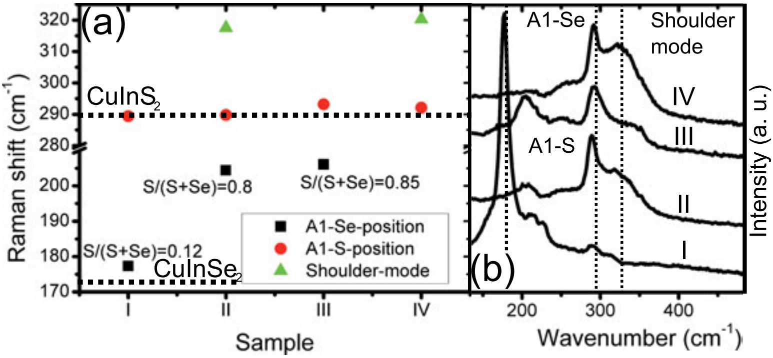

Figure 4.72: Raman analysis of the four absorber samples being post-treated at $T_S = 575\,^\circ$C (I), at $T_S = 575\,^\circ$C and S excess (II), at $T_S = 650\,^\circ$C (III) and at $T_S = 650\,^\circ$C and S excess (IV). A shoulder-mode is observed at 318 cm^{-1} when the absorber is exposed to an excess of S (II and IV) (reproduced from [11] with permission of Elsevier Publishing).

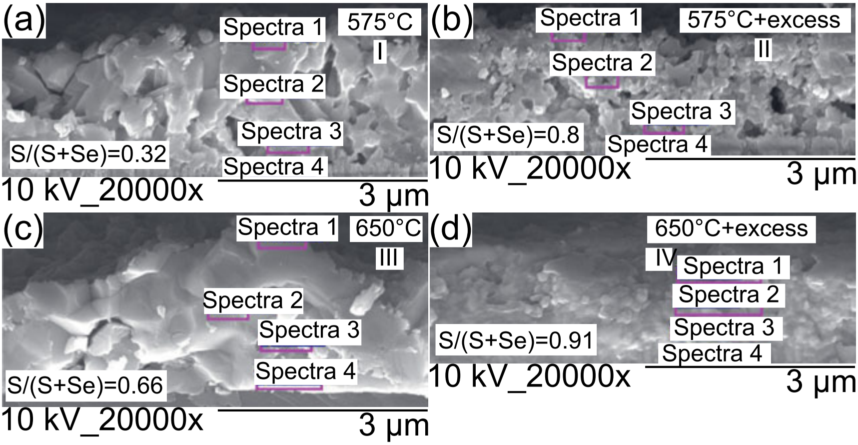

Figure 4.73: SEM cross sections of a 350 °C treated absorber sample being post-treated by $T_S = 575\,^\circ$C ((a) corresponding sample I), by $T_S = 575\,^\circ$C and additional S excess ((b) corresponding sample II), by $T_S = 650\,^\circ$C ((c) corresponding sample III) and by $T_S = 650\,^\circ$C and S excess ((d) corresponding sample IV). Strong morphological changes can be seen from (a) to (b) and (c) to (d), accompanied by a reduced grain size (reproduced from [11] with permission of Elsevier Publishing).

Short summary

The implementation of a two-step process has been shown to be a successful approach to control the incorporation of S into the CIGSe thin film. T_S in step 2 around 575 °C and S supply higher than 1.5 μm thickness of initial S layer is necessary to achieve a relevant S incorporation into a normal grained CIGSe absorber layer. For some process conditions a diffusion controlled S incorporation has been identified, which is based on a superposition of grain boundary and volume diffusion. A D value of approximately $D^S_{CIGSe} = 2.9 \cdot 10^{-11} \frac{cm^2}{s}$ was estimated for the diffusion controlled process (see section 4.2.3). The S incorporation is reduced by increasing T_{Se} in step 1 due to the increasing CIGSe to binary selenide ratio in the thin film. The S incorporation in these films with a certain amount of binary selenides is found to proceed via a two-reaction scenario which yields a D for the diffusion controlled process of $D^S_{CIGSe} = 1.1 \cdot 10^{-11} \frac{cm^2}{s}$ (see section 4.2.3). When the CIGSe thin film is exposed to a large S excess during the annealing step 2 a secondary phase, identified as the defect spinel phase $CuIn_5S_8$, is formed which results in a small grained absorber structure. These thin film structures are nearly Se-free and exhibit a reduction in layer thickness which indicates evaporation of the Se species during the sulfurization with S in excess.

CHAPTER 5

Summary and prospects

Summary

The present thesis focuses on improving η of chalcopyrite thin film solar cells produced by a fast industrial process by adjusting the optoelectronic and structural properties. Therefore a detailed time- and temperature-dependent analysis of the CIGSe and CIGSSe thin film phase formation was performed with the help of ex- and in-situ investigations. The approach used here to improve η is based on band gap (E_g) gradients and the opportunity to control them with process-related parameters like temperature (in the annealing chamber), S and Se partial pressure during the annealing, chalcogen amount (in the evaporation chamber), Na delivery (from the substrate) and modification of the process sequence (in the design of the experiment). The co-evaporation process from NREL produces record cells with V-profiles of the GGI ratio in the absorber (which directly influences the band structure), which serve as reference for the target values for given absorber composition. Therefore back contact grading as well as GGI and SSSe ratios at the absorber surface were the features to be optimized by variation of the process parameters. Under optimum process and layer design conditions efficiencies of 14.2% for CIGSe and 12.2% for CIGSSe thin film solar cells were achieved in this work.

The properties of the interface between CIGSSe and Mo have been investigated in detail for different selenization and sulfurization conditions. Preferred growth orientations of $MoSe_2$ and $MoSSe_2$ interlayers were found for the bare back contact and in the presence of metallic precursors. From an electronic viewpoint, the device performance is strongly influenced by the resistivity and the SSSe amount at the interface. For a higher SSSe ratio above 0.6 a pronounced reduction in FF has been found, and for a higher $MoSe_2$/Mo ratio a strong increase in series resistance (R_s) has been identified. Chalcogenisation of the back contact is very aggressive and involves corrosion of the Mo back contact. In order to control the back contact corrosion process a diffusion barrier layer has been introduced between the metallic precursor layers and the Mo back contact. The functional layer's task is to prevent excessive S/Se diffusion into the back contact and thereby allow to form a well-defined $Mo(S,Se)_2$ interface layer. Mo-N is introduced in this work as a potential candidate in this thin film system also because the integration into to the process is achievable without a lot of effort.

A major factor influencing the GGI profile is the Se excess during the selenization (Se amount) in the SEL process, which leads to a more homogeneous Ga/In profile of the thin film and makes a better E_g adjustment on the solar spectra possible. In this context D values of approximately $3.9 \cdot 10^{-12} \frac{cm^2}{s}$ at 575 °C for 2 μm Se supply were estimated based on a simple model of the interdiffusion process. Furthermore it is possible to achieve an appropriate Ga/In profile by setting an optimal process temperature in presence of a high temperature glass which withstands high thermal stress leading to an optimal E_g profile. By changing the glass substrates also Na delivery may also be influenced, which has a strong impact on the Ga/In interdiffusion properties. These experiments were performed in cooperation with the Schott AG as part of the public funding project comCIGS II, where the effect of high temperature glasses on the chalcopyrite structure and device performance are analyzed for special high temperature processes. Additionally, temperature-dependent diffusion coefficients were evaluated for ex- and in-situ analysis of the concentration profiles and the lattice constant change ($D \approx 4 - 7 \cdot 10^{-13} \frac{cm^2}{s}$) at 650 °C and 675 °C respectively with 1.5 μm Se supply.

Another approach followed in this work is based on S near-surface incorporation during the SEL process in order to achieve a double graded CIGSSe material, which is a big challenge in the SEL process with solid chalcogen layers. The simultaneous S/Se supply with different ratios leads to a homogeneous chalcogen profile in the absorber and therefore a constant E_g throughout the whole sample. The separation of the classical two-step process into a "three-step process" by introducing a separate selenization and sulfurization step allows better control of the S diffusion. With the help of an appropriate S-post treatment it seems to be possible to introduce an optimized front surface grading, which is found by the combination of in-situ XRD analysis and the planar diffusion model. It was possible to estimate D values for the process of S diffusion into CIGSe thin films of approximately $3 \cdot 10^{-11} \frac{cm^2}{s}$ at 650 °C with a S supply of 3 μm.

Prospects

In the thesis, it was attempted to correlate numerical calculations with the help of SCAPS with the experimental results and analyze the possible influence of a changing back surface or front surface grading as well as double graded band structures on the performance parameters (especially the V_{oc}). The evaluation can be extended to include different carrier mobilities, lifetimes, dominant recombination paths and absorber thicknesses. Additionally, the analytical approach introduced by [52, 53, 67] can be extended to more complex structures and serves an independent verification for the numerical calculations. For the absorber process technology, it is important to improve the p-n junction properties towards the buffer, as this is seen as the major limitation for V_{oc}, which strongly affects the η. After the selenization or sulfurization process an optimized post-processing is important to modify the absorber surface for the buffer deposition. Optimal storage conditions between absorber growth and post-processing steps for finished solar cell devices are necessary to protect the sensitive absorber surface against humidity.

APPENDIX A

Appendix

A.1 Introduction into SCAPS simulations

Since the working principle of a solar cell is based on charge transport ($\vec{J}$) and charge distribution ($\rho(\vec{r})$), the Poisson equation (see equation A.1), the transport equations (see equations A.2, A.3) and the continuity equation (see equations A.4, A.5) are needed. $\mu_{n,p}$ displays the mobility for e$^-$ and h$^+$ respectively. The Poisson equation (equation A.1), which is the first Maxwell equation, describes the correlation between $\rho(\vec{r})$ and the electrostatic potential $\Psi(\vec{r})$. One practical application deals with the determination of $\Psi(\vec{r})$ and the field distribution caused by $\rho(\vec{r})$ within the SCR [24]. The charge transport in a semiconductor is driven by a drift component (see equations A.2, A.3), which is caused by an electric field $\vec{\xi}$, and a diffusion component, which is influenced by the carrier concentration gradient.

$$\nabla \cdot \vec{\xi}(\vec{r}) = \frac{\rho(\vec{r})}{\varepsilon_0 \varepsilon_s},\ \vec{\xi}(\vec{r}) = -\nabla \Psi(\vec{r}) \tag{A.1}$$

$$\vec{J}_n = \underbrace{q\mu_n n \vec{\xi}}_{drift\ component} + \underbrace{qD_n \nabla n}_{diffusion\ component} \tag{A.2}$$

$$\vec{J}_p = \underbrace{q\mu_p p\vec{\xi}}_{drift\ component} - \underbrace{qD_p\nabla p}_{diffusion\ component} \tag{A.3}$$

The continuity equations describe the time dependent local e$^-$ (n) and h$^+$ (p) density variations caused by local recombination ($R(\vec{r})$) and generation ($G(\vec{r})$) rate, and by the gradient of the net current density $\vec{J}$ flowing in and out the respective volume element (see equations A.4, A.5) [24]. G_n and G_h are the e$^-$ and h$^+$ generation rate (unit: cm^{-3} s^{-1}), which are caused by absorption of photons [24]. R_n and R_h are the recombination rates, which can also be expressed in terms of carrier lifetimes τ_n and τ_p, respectively to $\frac{\Delta n}{\tau_n}$ and $\frac{\Delta p}{\tau_p}$ respectively [24]. Here, Δn (Δp) displays the excess charge carrier density and τ_n (τ_p) is the carrier lifetime.

$$\frac{\partial n}{\partial t} = G_n - R_n + \frac{1}{q}\nabla \vec{J}_n \tag{A.4}$$

$$\frac{\partial p}{\partial t} = G_h - R_h - \frac{1}{q}\nabla \vec{J}_p \tag{A.5}$$

In an idealized model solar cells can be treated as 1D structures because of their lateral homogeneity in the charge carrier transport direction, and then the five equations can also be simplified to 1D versions. The 1D simulation tool SCAPS [64] solves these five equations numerically, which for most problems requires less than 1 min of calculation time. This enables a fast correlation between experiments and simulations, which results in short feedback times. In equation A.6 the one-dimensional Poisson equation is introduced [24]. The relationship between potential and electric field can be expressed as $\xi = -\frac{\partial}{\partial x}\Psi_i$ in the 1D case. Therefore the potential can be calculated for different charge distributions. In this case N_A is the concentration of the ionized acceptors, N_D the ionized donors, p the density of h$^+$ and n the density of e$^-$. Charge neutrality must be fulfilled at all times, which means that the sum of all positive charges has to be equal to all negative charges $n + N_A = p + N_D$ [24].

$$\frac{\partial^2 \Psi_i}{\partial x^2} = -\frac{\partial \xi}{\partial x} = -\frac{\rho(x)}{\varepsilon_0 \varepsilon_s} = \frac{q(n - p + N_A - N_D)}{\varepsilon_0 \varepsilon_s} \tag{A.6}$$

J_n and J_p for e$^-$ and h$^+$ respectively in one dimension are expressed through the variation of the quasi Fermi energy levels E_{Fn} and E_{Fp} over the position x (see equations A.7, A.8). For the one-dimensional case, and with the restriction of low-level injection, which means that there are less excess carriers $\Delta p = \Delta n$ than the majority carriers, the following continuity equations can be written (see equations A.9, A.10) [24]. An n-type material is characterized by $n_n \approx N_D$ and $p_n = p_{n0} + \Delta p$, while a p-type material is described by $p_p \approx N_A$ and $n_p = n_{p0} + \Delta n$ [24]. p_{n0} (n$_{p0}$) is the concentration of h$^+$ (e$^-$) in the thermodynamical equilibrium in the n-type (p-type) material.

$$J_n = q\mu_n n\xi + qD_n\frac{dn}{dx} = q\mu_n\left(n\xi + \frac{k_BT}{q}\frac{dn}{dx}\right) = \mu_n n\frac{dE_{Fn}}{dx} \tag{A.7}$$

$$J_p = q\mu_p p\xi - qD_p\frac{dp}{dx} = q\mu_p\left(p\xi - \frac{k_BT}{q}\frac{dp}{dx}\right) = \mu_p p\frac{dE_{Fp}}{dx} \tag{A.8}$$

$$\frac{\partial n_p}{\partial t} = G_n - \frac{n_p - n_{po}}{\tau_n} + n_p\mu_n\frac{\partial\xi}{\partial x} + \mu_n\xi\frac{\partial n_p}{\partial x} + D_n\frac{\partial^2 n_p}{\partial x^2} \tag{A.9}$$

$$\frac{\partial p_n}{\partial t} = G_h - \frac{p_n - p_{n0}}{\tau_p} - p_n\mu_p\frac{\partial\xi}{\partial x} - \mu_p\xi\frac{\partial p_n}{\partial x} + D_p\frac{\partial^2 p_n}{\partial x^2} \tag{A.10}$$

These equations are solved numerically in SCAPS, which gives the basic solar cell parameters like V_{oc}, J_{sc}, FF and η as output.

A.2 Derivation of J_{grad} with the analytical approach

For the ideal case (collection efficiency equal 100%) of e$^-$/h$^+$ pair separation and generation in the solar cell, J is estimated by integrating over the energy interval $d(h\nu)$ and over g in an infinitesimal thin spatial slice dx (see equation A.11).

$$J = q \int_{0}^{+\infty} d(h\nu) \int_{0}^{d} g dx = q \int_{0}^{+\infty} d(h\nu)\phi_0 \int_{0}^{d} \alpha e^{-\alpha x} dx = q \int_{0}^{+\infty} d(h\nu)\phi_0 [1-e^{-\alpha d}] \tag{A.11}$$

The situation changes when E_g varies as function of position x (see figure 2.13 (b)), which results in an α changing with position. α can be expressed with the extinction coefficient k_e (from the complex refractive index in equation A.12) and λ according to equation A.13 [24]. Near the absorption edge, α can be approximated by equation A.14 for direct semiconductors.

$$\overline{n} = n_r - ik_e \tag{A.12}$$

$$\alpha = \frac{4\pi k_e}{\lambda} \tag{A.13}$$

$$\alpha \propto (h\nu - E_g)^{1/2} \tag{A.14}$$

Equation A.14 is extended by the linear E_g variation $E_g(x) = E_g^{max} - \beta x$ from E_g^{max} to E_g^{min} [52]. β is a positive number calculated by $\beta = \frac{E_g^{max} - E_g^{min}}{d}$, which describes the linear E_g grading degree. d is the thickness of the absorber layer and x displays the relative change of E_g as a function of the composition (Ga/(Ga+In)). This leads to the equation A.15 by replacing the value for $E_g(x)$.

$$\alpha \propto (h\nu - E_g^{max} + \beta x)^{1/2} \tag{A.15}$$

Absorption will start after a critical distance d_c inside a linear graded absorber for the different photon energies $h\nu_i$ [52]. The $\mathrm{e}^-/\mathrm{h}^+$ generation rate g can be expressed as a function, which is defined for values smaller and greater than d_c (see equations A.16, A.17).

$$g = 0,\ 0 \leq x \leq d_c \tag{A.16}$$

$$g = -\frac{d\phi}{dx} = \phi_0(h\nu - E_g^{max} + \beta x)^{1/2} e^{\left(-\frac{2}{3\beta}\left[(h\nu - E_g^{max}+\beta x)^{3/2}\right]\right)},\ x > d_c \tag{A.17}$$

J can now be calculated using the equation A.11, but according to the definition of g only values for $x > d_c$ contribute to J because below d_c g will be zero (see equation A.16). Below d_c the incoming photons with a certain energy $h\nu_i$ cannot be absorbed inside the absorber and therefore no carrier can be generated. In this way J depends on the different α_{eff} values which differ for the different grading degree (see equation A.18).

$$J = q\int_0^\infty d(h\nu)\int_{d_c}^{d} g dx = ... = q\int_0^\infty d(h\nu)\phi_0[1 - e^{-\alpha_{eff}d}] \tag{A.18}$$

α_{eff} is defined for the three different energy sections $\left[0, E_g^{min}\right]$, $\left[E_g^{min}, \frac{3}{2}\left(E_g^{max} - E_g^{min}\right) + E_g^{min}\right]$ and $\left[\frac{3}{2}\left(E_g^{max} - E_g^{min}\right) + E_g^{min}, \infty\right]$ (according to the procedure in [52]), which is divided into the following expressions A.19, A.20 and A.21. For the first energy section the case of non-absorption is described along equation A.19 because the incident photon energy is below E_g^{min}. In the second energy section the linear interpolation part from E_g^{min} towards $\frac{3}{2}\left(E_g^{max} - E_g^{min}\right) + E_g^{min}$ is described in A.20. The third energy section displays the constant absorption region in A.21.

$$\alpha_{eff} = 0,\ 0 < h\nu < E_g^{min} \tag{A.19}$$

$$\alpha_{eff} = \frac{2}{3}\alpha_g^{min}\underbrace{\left(\frac{h\nu - E_g^{min}}{E_g^{max} - E_g^{min}}\right)}_{<1},\ E_g^{min} < h\nu < \frac{3}{2}\left(E_g^{max} - E_g^{min}\right) + E_g^{min} \tag{A.20}$$

$$\alpha_{eff} = \alpha_g^{min},\ \frac{3}{2}\left(E_g^{max} - E_g^{min}\right) + E_g^{min} < h\nu \tag{A.21}$$

Bibliography

[1] A. E. Becquerel, Compt. Rend. Acad. Sci. **9**, 561 (1839).

[2] A. Goetzberger, C. Helbing, and H.-W. Schock, Materials Science and Engineering: R: Reports **40**, 1 (2003).

[3] M. A. Green, *Third generation photovoltaics: advanced solar energy conversion* (Springer, 2003).

[4] J. Nelson, *The Physics of Solar Cells (Properties of Semiconductor Materials)* (Imperial College Press, London, 2003).

[5] D. M. Bagnall and M. Boreland, Energy Policy **36**, 4390 (2008).

[6] J. Yang, J. Nam, D. Kim, D. Lee, and P. Huh, Solar Energy Materials and Solar Cells **144**, 467 (2016).

[7] P. Jackson, R. Wuerz, D. Hariskos, E. Lotter, W. Witte, and M. Powalla, Physica status solidi rapid research letters **1**, 1 (2016).

[8] P. Jackson, D. Hariskos, R. Wuerz, O. Kiowski, A. Bauer, T. M. Friedlmeier, and M. Powalla, Physica status solidi rapid research letters **1**, 28 (2015).

[9] S. Siebentritt, Solar Energy Materials and Solar Cells **95**, 1471 (2011), Special Issue : Thin film and nanostructured solar cells.

[10] W. Shockley and H. J. Queisser, Journal of Applied Physics **32**, 510 (1961).

[11] B. J. Mueller, M. Mock, V. Haug, F. Hergert, T. Koehler, S. Zweigart, and U. Herr, Thin Solid Films **582**, 284 (2015).

[12] B. J. Mueller, C. Zimmermann, V. Haug, F. Hergert, T. Koehler, S. Zweigart, and U. Herr, Journal of Applied Physics **116**, 8 (2014).

[13] B. J. Mueller, B. Opasanont, V. Haug, F. Hergert, S. Zweigart, and U. Herr, Thin Solid Films **608**, 62 (2016).

[14] B. J. Mueller, A. Fotler, V. Haug, F. Hergert, S. Zweigart, and U. Herr, Thin Solid Films **612**, 186 (2016).

[15] B. J. Mueller, T. Demes, P. C. Lill, V. Haug, F. Hergert, S. Zweigart, and U. Herr, Journal of Crystal Growth **442**, 31 (2016).

[16] B. J. Mueller, *Improvement of Cu(In,Ga)(S,Se)2 thin film solar cells with the help of Gallium and Sulfur gradients*, Ph.D. thesis, University of Ulm (2017).

[17] A. McEvoy, T. Markvart, and L. Castaner, eds., *Practical Handbook of Photovoltaics: Fundamentals and Applications* (Academic Press, 2011).

[18] R. Scheer and H.-W. Schock, *Chalcogenide Photovoltaics - Physics, Technologies, and Thin Film Devices* (WILEY-VCH Verlag, 2011).

[19] S. Wagner, J. L. Shay, P. Migliorato, and H. M. Kasper, Applied Physics Letters **25**, 434 (1974).

[20] S. Siebentritt and U. Rau, in *Wide-Gap Chalcopyrites*, edited by S. Siebentritt and U. Rau (Springer, 2006), chap. 1, pp. 1–8.

[21] D. Abou-Ras, T. Kirchartz, and U. Rau, eds., *Advanced characterisation techniques for thin film solar cells* (Wiley-VCH Verlag GmbH & Co. KGaA, 2009).

[22] U. Rau and H.-W. Schock, in *Clean electricity from photovoltaics (Series on Photoconversion of Solar Energy vol. 1)* (Imperial College Press, London, 2001).

[23] U. Rau and H.-W. Schock, in *Practical Handbook of Photovoltaics: Fundamentals and Applications*, edited by A. McEvoy, T. Markvart, and L. Castaner (Academic Press, 2011), chap. IC-3, pp. 323–395.

[24] S. M. Sze and K. N. Kwok, eds., *Physics of Semiconductor Devices* (John Wiley & Sons, Inc., 2007).

[25] D. K. Schroder, *Semiconductor Material and Device Characterization* (Wiley, 2006), 3rd edn..

[26] S. Hunklinger, *Festkoerperphysik* (Oldenbourg Verlag Muenchen Wien, 2007).

[27] H. Hahn, G. Frank, W. Klingler, A. Meyer, and G. Stoerger, Zeitschrift fuer anorganische und allgemeine Chemie **271**, 153 (1953).

[28] S. Zweigart, *Herstellung von Cu(In,Ga)Se_2 - Duennschichten durch sequentielle Prozesse - Untersuchungen zur Reaktionskinetik*, Ph.D. thesis, Universitaet Stuttgart (2000).

[29] I. M. Koetschau, *Strukturelle Untersuchungen an Cu(In,Ga)$(S,Se)_2$ Duennschichten*, Ph.D. thesis, Universitaet Stuttgart (2003).

[30] A. Jasenek, *Eigenschaften von Defekten in Cu(In,Ga)Se_2 nach Elektronen- und Protonenbestrahlung*, Ph.D. thesis, Universitaet Stuttgart (2002).

[31] F. Hergert, *Chemical formation reactions for Cu(In,Ga)Se_2 and other chalcopyrite compounds – An in-situ x-ray diffraction study and crystallographic models*, Ph.D. thesis, Friedrich-Alexander-Universitaet Erlangen-Nuernberg (2007).

[32] T. Schulmeyer, *Mechanismen der Grenzflaechenausbildung des Cu(In,Ga)Se$_2$-Systems*, Ph.D. thesis, Technische Universitaet Darmstadt (2005).

[33] P. Y. Yu and M. Cardona, eds., *Fundamentals of Semiconductor - Physics and Materials Properties* (Springer, 2010).

[34] U. Rau and H.-W. Schock, Applied Physics A: Materials Science & Processing **69**, 131 (1999).

[35] S. Chichibu, T. Mizutani, K. Murakami, T. Shioda, T. Kurafuji, H. Nakanishi, S. Niki, P. J. Fons, and A. Yamada, Journal of Applied Physics **83**, 3678 (1998).

[36] T. Goedecke, T. Haalboom, and F. Ernst, Zeitschrift fuer Metallkunde **91**, 622 (2000).

[37] T. Goedecke, T. Haalboom, and F. Ernst, Zeitschrift fuer Metallkunde **91**, 635 (2000).

[38] T. Goedecke, T. Haalboom, and F. Ernst, Zeitschrift fuer Metallkunde **91**, 651 (2000).

[39] J. Philibert, *Atom Movements - Diffusion and Mass Transport in Solids*. Hors collection (EDP Sciences, 2012).

[40] A. Fick, Annalen der Physik **170**, 59 (1855).

[41] W. Shockley, Bell System Technical Journal **28**, 435 (1949).

[42] E. Rudigier, *Phase transformations and crystalline quality of CuInS$_2$ thin films*, Ph.D. thesis, Philipps-Universitaet Marburg (2004).

[43] J. Eberhardt, *Photolumineszenz epitaktischer und polykristalliner CuInS$_2$-Schichten fuer Duennschichtsolarzellen*, Ph.D. thesis, Friedrich-Schiller-Universitaet Jena (2007).

[44] T. Kirchartz and U. Rau, physica status solidi (a) **205**, 2737 (2008).

[45] T. Kirchartz, *Generalized detailed balance theory of solar cells*, Ph.D. thesis, RWTH Aachen (2009).

[46] P. Wurfel, Journal of Physics C: Solid State Physics **15**, 3967 (1982).

[47] P. Jackson, D. Hariskos, E. Lotter, S. Paetel, R. Wuerz, R. Menner, W. Wischmann, and M. Powalla, Progress in Photovoltaics: Research and Applications **19**, 894 (2011).

[48] M. A. Green, K. Emery, Y. Hishikawa, W. Warta, and E. D. Dunlop, Progress in Photovoltaics: Research and Applications **20**, 606 (2012).

[49] J. H. Werner, J. Mattheis, and U. Rau, Thin Solid Films **480 - 481**, 399 (2005), Proceedings of Symposium O on Thin Film Chalcogenide Photovoltaic Materials, EMRS 2004 Conference, Strasbourg, France, May 24-28, 2004.

[50] T. Eisenbarth, *Identifikation von Defekten und Metastabilitaeten in Cu(In,Ga)Se$_2$-Duennschichtsolarzellen*, Ph.D. thesis, Fachbereich Physik - FU Berlin (2010).

[51] S. Dongaonkar, J. D. Servaites, G. M. Ford, S. Loser, J. Moore, R. M. Gelfand, H. Mohseni, H. W. Hillhouse, R. Agrawal, M. A. Ratner, T. J. Marks, M. S. Lundstrom, and M. A. Alam, Journal of Applied Physics **108**, 124509 (2010).

[52] A. Morales-Acevedo, Solar Energy Materials and Solar Cells **93**, 41 (2009).

[53] A. Morales-Acevedo, Energy Procedia **2**, 169 (2010).

[54] T. Dullweber, G. Hanna, U. Rau, and H. W. Schock, Solar Energy Materials and Solar Cells **67**, 145 (2001).

[55] K. Decock, J. Lauwaert, and M. Burgelman, Energy Procedia **2**, 49 (2010), Proceedings of Inorganic and Nanostructured Photovoltaics (E-MRS 2009 Symposium B).

[56] M. Gloeckler and J. R. Sites, Journal of Physics and Chemistry of Solids **66**, 1891 (2005).

[57] J. Haarstrich, H. Metzner, C. Ronning, A. Undisz, T. Rissom, C. A. Kaufmann, and H. W. Schock, Thin Solid Films **520**, 3657 (2012).

[58] M. Turcu, I. Koetschau, and U. Rau, Journal of Applied Physics **91**, 1391 (2002).

[59] A. Morales-Acevedo, N. Hernández-Como, and G. Casados-Cruz, Materials Science and Engineering: B **177**, 1430 (2012).

[60] M. Burgelman, J. Verschraegen, S. Degrave, and P. Nollet, Progress in Photovoltaics: Research and Applications **12**, 143 (2004).

[61] M. Murata, D. Hironiwa, N. Ashida, J. Chantana, K. Aoyagi, N. Kataoka, and T. Minemoto, Japanese Journal of Applied Physics **53**, 04ER14 (2014).

[62] K. Decock, J. Lauwaert, and M. Burgelman, in *International conference on Microelectronics devices and technologies, 45th, Proceedings*, edited by M. Topic, J. Krc, and I. Sorli (MIDEM - Society for Microelectronics, Electronic Components and Materials, 2009), p. 245.

[63] P. Paulson, R. Birkmire, and W. Shafarman, Journal of Applied Physics **94**, 879 (2003).

[64] M. Burgelman, P. Nollet, and S. Degrave, Thin Solid Films **361-362**, 527 (2000).

[65] C. Adel, B. M. Fethi, and B. Brahim, International Journal of Physical Sciences **9**, 250 (2014).

[66] T. Ott, T. Walter, and T. Unold, Thin Solid Films **535**, 275 (2013).

[67] A. Morales-Acevedo, Solar Energy **83**, 1466 (2009).

[68] S. Niki, M. Contreras, I. Repins, M. Powalla, K. Kushiya, S. Ishizuka, and K. Matsubara, Progress in Photovoltaics: Research and Applications **18**, 453 (2010).

[69] J. Palm, V. Probst, and F. H. Karg, Solar Energy **77**, 757 (2004).

[70] V. Probst, W. Stetter, W. Riedl, H. Vogt, M. Wendl, H. Calwer, S. Zweigart, K.-D. Ufert, B. Freienstein, H. Cerva, and F. H. Karg, Thin Solid Films **387**, 262 (2001).

[71] B. Dimmler, E. Gross, R. Menner, M. Powalla, D. Hariskos, M. Ruckh, U. Ruhle, and H. Schock, Photovoltaic Specialists Conference, 1996., Conference Record of the Twenty Fifth IEEE **1**, 757 (1996).

[72] M. Powalla, G. Voorwinden, D. Hariskos, P. Jackson, and R. Kniese, Thin Solid Films **517**, 2111 (2009), Thin Film Chalogenide Photovoltaic Materials (EMRS, Symposium L).

[73] M. Powalla and B. Dimmler, Thin Solid Films **387**, 251 (2001).

[74] R. Mickelsen and W. S. Chen, Applied Physics Letters **36**, 371 (1980).

[75] A. M. Gabor, J. R. Tuttle, D. S. Albin, M. A. Contreras, R. Noufi, and A. M. Hermann, Applied Physics Letters **65**, 198 (1994).

[76] V. Alberts, Thin Solid Films **517**, 2115 (2009), Thin Film Chalogenide Photovoltaic Materials (EMRS, Symposium L).

[77] V. Alberts, Semiconductor Science and Technology **19**, 65 (2004).

[78] H. K. Song, J. K. Jeong, H. J. Kim, S. K. Kim, and K. H. Yoon, Thin Solid Films **435**, 186 (2003).

[79] F. Karg, V. Probst, H. Harms, J. Rimmasch, W. Riedl, J. Kotschy, J. Holz, R. Treichler, O. Eibl, A. Mitwalsky, and A. Kiendl, Photovoltaic Specialists Conference, 1993., Conference Record of the Twenty Third IEEE **1**, 441 (1993).

[80] V. Probst, I. Koetschau, E. Novak, A. Jasenek, H. Eschrich, F. Hergert, T. Hahn, J. Feichtinger, M. Maier, B. Walther, and V. Nadenau, IEEE Journal of Photovoltaics **4**, 687 (2014).

[81] I. M. Koetschau, A. Kampmann, T. Hahn, J. Hinze, E. Richter, and D. Schmid, 24th European Photovoltaic Solar Energy Conference **1**, 2450 (2009).

[82] D. Wolf and G. Mueller, Japanese Journal of Applied Physics **39S1**, 173 (2000).

[83] P. Berwian, *Experimentelle Untersuchung und Modellierung der Bildungskinetik von CuInSe$_2$-basierten Halbleiter-Duennschichten fuer die Solarzellenherstellung*, Ph.D. thesis, Univ. Erlangen (2005).

[84] M. Purwins, P. Berwian, E. Fueglein, and G. Mueller, 19th European Photovoltaic Solar Energy Conference **19**, 1947 (2004).

[85] M. Purwins, *Phasenbildung und Reaktionskinetik bei der Herstellung des Chalkopyrit-Solarzellenmaterials Cu(In,Ga)(Se,S)$_2$*, Ph.D. thesis, Univ. Erlangen (2010).

[86] A. Hoelzing, R. Schurr, H. Yoo, R. Wibowo, R. Lechner, J. Palm, S. Jost, and R. Hock, Thin Solid Films **535**, 112 (2013).

[87] D. Wolf, *Technologienahe in-situ Analyse der Bildung von CuInSe$_2$ zur Anwendung in Duennschicht-Solarzellen*, Ph.D. thesis, Friedrich-Alexander-Universitaet Erlangen-Nuernberg (1998).

[88] J. Pankove, ed., *Optical processes in semiconductors* (Dover Publications, Inc., 1971).

[89] M. V. Yakushev, A. V. Mudryi, V. F. Gremenok, V. B. Zalesski, P. I. Romanov, Y. V. Feofanov, R. W. Martin, and R. D. Tomlinson, Journal of Physics and Chemistry of Solids **64**, 2005 (2003), 13th International Conference on Ternary and Multinary Compounds.

[90] W. Witte, R. Kniese, and M. Powalla, Thin Solid Films **517**, 867 (2008).

[91] C. Rincon and F. J. Ramirez, Journal of Applied Physics **72**, 4321 (1992).

[92] R. Bacewicz, W. Gebicki, and J. Filipowicz, Journal of Physics: Condensed Matter **6**, L777 (1999).

[93] V. Izquierdo, A. Pérez-Rodríguez, L. Calvo-Barrio, J. Álvarez-García, J. Morante, V. Bermudez, O. Ramdani, J. Kurdi, P. Grand, L. Parissi, et al., Thin Solid Films **516**, 7021 (2011).

[94] V. Izquierdo-Roca, R. Caballero, X. Fontane, C. A. Kaufmann, J. Alvarez-Garcia, L. Calvo-Barrio, E. Saucedo, A. Perez-Rodriguez, J. R. Morante, and H. W. Schock, Thin Solid Films **519**, 7300 (2011), Proceedings of the EMRS 2010 Spring Meeting Symposium M: Thin Film Chalcogenide Photovoltaic Materials.

[95] X. Fontane, V. Izquierdo-Roca, L. Calvo-Barrio, A. Perez-Rodriguez, J. R. Morante, D. Guettler, A. Eicke, and A. N. Tiwari, Applied Physics Letters **95**, 261912 (2009).

[96] Y.-P. Fu, R.-W. You, and K. K. Lew, Journal of The Electrochemical Society **156**, 12 (2009).

[97] D. Wang, L. Wan, Z. Bai, and Y. Cao, Applied Physics Letters **92**, 211912 (2008).

[98] I. M. Koetschau and H. W. Schock, Journal of Applied Crystallography **39**, 683 (2006).

[99] A. G173, *Standard Tables for Reference Solar Spectral Irradiance: Direct Normal and Hemispherical on 37° C Tilted Surface* (2012).

[100] M. Ganchev, J. Kois, M. Kaelin, S. Bereznev, E. Tzvetkova, O. Volobujeva, N. Stratieva, and A. Tiwari, Thin Solid Films **511-512**, 325 (2006).

[101] M. S. Kim, R. B. V. Chalapathy, J. H. Yun, K. H. Yoon, and B. T. Ahn, 22nd European Photovoltaic Solar Energy Conference **1**, 2259 (2007).

[102] O. Lundberg, M. Edoff, and L. Stolt, Thin Solid Films **480-481**, 520 (2005).

[103] M. Marudachalam, R. W. Birkmire, H. Hichri, J. M. Schultz, A. Swartzlander, and M. M. Al-Jassim, Journal of Applied Physics **82**, 2896 (1997).

[104] J. Wang, Y. Zhang, F. Dong, and J. Zhu, Applied Surface Science **258**, 8636 (2012).

[105] N. Barreau, P. Zabierowski, L. Arzel, M. Igalson, K. Macielak, A. Urbaniak, T. Lepetit, T. Painchaud, A. Doenmez, and J. Kessler, Thin Solid Films **582**, 43 (2014).

[106] H. Matsushita and T. Takizawa, Journal of Crystal Growth **191**, 455 (1998).

[107] F. Hergert, S. Jost, R. Hock, M. Purwins, and J. Palm, physica status solidi (a) **203**, 2615 (2006).

[108] A. Brummer, V. Honkimaeki, P. Berwian, V. Probst, J. Palm, and R. Hock, Thin Solid Films **437**, 297 (2003).

[109] F. Hergert, R. Hock, A. Weber, M. Purwins, J. Palm, and V. Probst, Journal of Physics and Chemistry of Solids **66**, 1903 (2005).

[110] M. Oertel, *Untersuchung zur Reaktionskinetik und Rueckkontaktmorphologie von CuInSe*$_2$*-Duennschichtsolarzellen*, Ph.D. thesis, Friedrich-Schiller-Universitaet Jena (2012).

[111] M. Marudachalam, I. Hichri, R. Birkmire, J. Schultz, A. Swartzlander, and M. Al-Jassim, Photovoltaic Specialists Conference, 1996., Conference Record of the Twenty Fifth IEEE pp. 805–807.

[112] P. Pistor, *Formation and Electronic Properties of $In_2Se_3/Cu(In,Ga)Se_2$ Junctions and Related Thin Film Solar Cells*, Ph.D. thesis, Freie Universitaet Berlin (2009).

[113] Q. Cao, O. Gunawan, M. Copel, K. B. Reuter, S. J. Chey, V. R. Deline, and D. B. Mitzi, Advanced Energy Materials **1**, 845 (2011).

[114] S.-H. Wei, S. B. Zhang, and A. Zunger, Applied Physics Letters **72**, 3199 (1998).

[115] S. Siebentritt, M. Igalson, C. Persson, and S. Lany, Progress in Photovoltaics: Research and Applications **18**, 390 (2010).

[116] D. Abou-Ras, G. Kostorz, D. Bremaud, M. Kaelin, F. V. Kurdesau, A. Tiwari, and M. Doebeli, Thin Solid Films **480-481**, 433 (2005).

[117] X. Zhu, Z. Zhou, Y. Wang, L. Zhang, A. Li, and F. Huang, Solar Energy Materials and Solar Cells **101**, 57 (2012).

[118] M. A. Nicolet, Thin Solid Films **52**, 415 (1978).

[119] M. A. Nicolet and M. Bartur, Journal of Vacuum Science and Technology **19**, 786 (1981).

[120] K. Orgassa, H. W. Schock, and J. H. Werner, Thin Solid Films **431-432**, 387 (2003), Proceedings of Symposium B, Thin Film Chalcogenide Photovoltaic Materials, E-MRS Spring Meeting.

[121] M. Pritschow, *Titannitrid- und Titan-Schichten fuer die Nano-Elektromechanik*, Ph.D. thesis, Universitaet Stuttgart (2007).

[122] D. Nachrodt, *Temperaturstabile Duennfilmwiderstaende aus Ti/TiN und Ti/NiCr mit niedrigem Temperaturkoeffizienten und ihre Integration in einen Standard-CMOS-Prozess*, Ph.D. thesis, Universitaet Duisburg-Essen (2008).

[123] B. Zhao, K. Sun, Z. Song, and J. Yang, Applied Surface Science **256**, 6003 (2010).

[124] W. Zeng, X. Wang, S. H. Meiere, and E. Eisenbraun, ECS Transactions **1**, 163 (2006).

[125] V. P. Anitha, S. Major, D. Chandrashekharam, and M. Bhatnagar, Surface and Coatings Technology **79**, 50 (1996).

[126] K. Inumaru, K. Baba, and S. Yamanaka, Physica B: Condensed Matter **383**, 84 (2006).

[127] P. Bloesch, A. Chirila, F. Pianezzi, S. Seyrling, P. Rossbach, S. Buecheler, S. Nishiwaki, and A. N. Tiwari, IEEE Journal of Photovoltaics **1**, 194 (2011).

[128] R. Usui, T. Tomizawa, T. Okato, and H. Odaka, in *Photovoltaic Specialists Conference (PVSC), 2012 38th IEEE*, IEEE (2012), p. 003108.

[129] D. Rudmann, *Effects of sodium on growth and properties of Cu(In,Ga) Se$_2$ thin films and solar cells*, Ph.D. thesis, ETH Zuerich (2004).

[130] H. Rodriguez-Alvarez, R. Mainz, R. Caballero, D. Abou-Ras, M. Klaus, S. Gledhill, A. Weber, C. Kaufmann, and H.-W. Schock, Solar Energy Materials and Solar Cells **116**, 102 (2013).

[131] A. Chirila, P. Reinhard, F. Pianezzi, P. Bloesch, A. R. Uhl, C. Fella, L. Kranz, D. Keller, C. Gretener, H. Hagendorfer, D. Jaeger, R. Erni, S. Nishiwaki, S. Buecheler, and A. N. Tiwari, Nature Materials **12**, 1107 (2013).

[132] A. Laemmle, R. Wuerz, and M. Powalla, physica status solidi (RRL) **7**, 631 (2013).

[133] J. Haarstrich, H. Metzner, M. Oertel, C. Ronning, T. Rissom, C. Kaufmann, T. Unold, H. W. Schock, J. Windeln, W. Mannstadt, and E. Rudigier-Voigt, Solar Energy Materials and Solar Cells **95**, 1028 (2011).

[134] M. Venkatachalam, M. Kannan, S. Jayakumar, R. Balasundaraprabhu, and N. Muthukumarasamy, Thin Solid Films **516**, 6848 (2008), Proceedings on Advanced Materials and Concepts for Photovoltaics EMRS 2007 Conference, Strasbourg, France.

[135] G. M. Hanket, R. Kamada, W. K. Kim, and W. N. Shafarman, in *Proceedings of the 33rd IEEE Photovoltaic Specialists Conference, San Diego* (2008).

[136] M. Marudachalam, H. Hichri, R. Klenk, R. Birkmire, W. Shafarman, and J. Schultz, Applied Physics Letters **67**, 3978 (1995).

[137] M. Contreras, L. Mansfield, B. Egaas, J. Li, M. Romero, R. Noufi, E. Rudiger-Voigt, and W. Mannstadt, in *37th IEEE Photovoltaic Specialists Conference (PVSC 37) Seattle, Washington* (2011), p. 19.

[138] D. J. L. Bremaud, *Investigation and Development of CIGS Solar Cells on Flexible Substrates and with Alternative Electrical Back Contacts*, Ph.D. thesis, ETH Zuerich (2009).

[139] M. I. Ojovan, Entropy **10**, 334 (2008).

[140] M. I. Ojovan, K. P. Travis, and R. J. Hand, Journal of Physics: Condensed Matter **19**, 415107 (2007).

[141] D. F. Dawson-Elli, C. B. Moore, R. R. Gay, and C. L. Jensen, Photovoltaic Energy Conversion, 1994., Conference Record of the Twenty Fourth. IEEE Photovoltaic Specialists Conference - 1994, 1994 IEEE First World Conference on **1**, 152 (1994).

[142] F. Yan, W. Liu, G. Jiang, X. Li, H. Xie, and C. Zhu, Journal of Materials Research **27**, 1112 (2012).

[143] S.-H. Wei and A. Zunger, Journal of Applied Physics **78**, 3846 (1995).

[144] Y. Nagoya, K. Kushiya, M. Tachiyuki, and O. Yamase, Solar Energy Materials and Solar Cells **67**, 247 (2001).

[145] T. Nakada, H. Ohbo, T. Watanabe, H. Nakazawa, M. Matsui, and A. Kunioka, Solar Energy Materials and Solar Cells **49**, 285 (1997).

[146] M. Purwins, M. Schmid, P. Berwian, G. Mueller, S. Jost, F. Hergert, and R. Hock, 21st European Photovoltaic Solar Energy Conference **1**, 2002 (2006).

[147] E. P. Zaretskaya, V. F. Gremenok, V. Zalesski, K. Bente, S. Schorr, and S. Zukotynski, Thin Solid Films **515**, 5848 (2007).

[148] H. Neff, P. Lange, M. Fearheiley, and K. Bachmann, Applied Physics Letters **47**, 1089 (1985).

[149] R. Scheer, Progress in Photovoltaics: Research and Applications **20**, 507 (2012).

[150] X. Shang, Z. Wang, M. Li, L. Zhang, J. Fang, J. Tai, and Y. He, Thin Solid Films **550**, 649 (2014).

[151] B. Ajalkar, R. Mane, B. Sarwade, and P. Bhosale, Solar energy materials and solar cells **81**, 101 (2004).

[152] R. Klenk, Thin Solid Films **387**, 135 (2001).

[153] T. Orgis, M. Maiberg, and R. Scheer, Journal of Applied Physics **114**, 214506 (2013).

[154] C. P. Thompson, S. Hegedus, W. Shafarman, and D. Desai, in *Photovoltaic Specialists Conference, 2008. PVSC'08. 33rd*, IEEE (2008), p. 1.

[155] K. Ramanathan, G. Teeter, J. Keane, and R. Noufi, Thin Solid Films **480**, 499 (2005).

[156] T. Walter, D. Braunger, H. Dittrich, C. Koeble, R. Herberholz, and H. Schock, Solar Energy Materials and Solar Cells **41/42**, 355 (1996).

[157] M. Engelmann, B. McCandless, and R. Birkmire, Thin Solid Films **387**, 14 (2001).

[158] B. Basol, A. Halani, C. Leidholm, G. Norsworthy, V. Kapur, A. Swartzlander, and R. Matson, Progress in Photovoltaics: Research and Applications **8**, 227 (2000).

[159] J. Titus, R. W. Birkmire, C. Hack, G. Muller, and P. McKeown, Journal of Applied Physics **99**, 043502 (2006).

[160] J. Titus, H.-W. Schock, R. W. Birkmire, W. N. Shafarman, and U. P. Singh, Proceedings **668**, H1.5 (2001), 2001 MRS Spring Meeting.

[161] J. Morante, L. Calvo-Barrio, R. Scheer, R. Klenk, et al., Journal of Vacuum Science & Technology A: Vacuum, Surfaces, and Films **19**, 232 (2001).

[162] R. Yoosuf and M. Jayaraj, Thin Solid Films **515**, 6188 (2007).

Author's publications

Journal Articles

- B. J. Mueller, M. Mock, V. Haug, F. Hergert, T. Koehler, S. Zweigart, and U. Herr, Ex- and in-situ investigations of sulfur diffusion into Cu(In,Ga)Se_2 thin films, Thin Solid Films 582 (2015), 284-289

- B. J. Mueller, C. Zimmermann, V. Haug, F. Hergert, T. Koehler, S. Zweigart, and U. Herr, Influence of different sulfur to selenium ratios on the structural and electronic properties of Cu(In,Ga)$(S,Se)_2$ thin films and solar cells formed by the stacked elemental layer process, Journal of Applied Physics 116, 174503 (2014)

- B. J. Mueller, T. Demes, P. C. Lill, V. Haug, F. Hergert, S. Zweigart and U. Herr, Temperature dependency of Ga/In distribution in Cu(In,Ga)Se_2 absorbers in high temperature processes, Journal of Crystal Growth 442 (2016), 31-40

- B. J. Mueller, B. Opasanont, V. Haug, F. Hergert, S. Zweigart and U. Herr, Influence of selenium amount on the structural and electronic properties of Cu(In,Ga)Se_2 thin films and solar cells formed by the stacked elemental layer process, Thin Solid Films 608 (2016), 62-70

- B. J. Mueller, A. Fotler, V. Haug, F. Hergert, S. Zweigart and U. Herr, Influence of Mo-N as diffusion barrier in Mo back contacts for Cu(In,Ga)Se_2 solar cells, Thin Solid Films 612 (2016), 186-193

Proceedings

- PVTC 2013, Influence of selenium and sulfur amount on the structural and electronic properties of $Cu(In,Ga)(Se,S)_2$ thin films and solar cells, 22.05-24.05.2013
- EMRS 2013, Influence of selenium and sulfur amount on the structural and electronic properties of $Cu(In,Ga)(Se,S)_2$ thin films and solar cells, 25.05-31.05.2013
- EMRS 2014, Controlled in-situ sulfur incorporation with different Cu(In,Ga)Se2 absorber pre-treatments for graded $Cu(In,Ga)(S,Se)_2$ solar cell applications

Oral Presentations

- EMRS 2013, Influence of selenium and sulfur amount on the structural and electronic properties of $Cu(In,Ga)(Se,S)_2$ thin films and solar cells, 30.05.2013, Session D. XIII, Strassburg
- öffentlich gefördertes Projekt comCIGS II, High temperature selenization processes on different glass substrates, 11.10.2013, Berlin

Poster Presentation

- EMRS 2014, Controlled in-situ sulfur incorporation with different $Cu(In,Ga)Se_2$ absorber pre-treatments for graded $Cu(In,Ga)(S,Se)_2$ solar cell applications, Session A. P3-43, Lille

Online-Buchshop für Ingenieure

■■ VDI nachrichten

Online-Shops

Fachliteratur und mehr - jetzt bequem online recherchieren & bestellen unter: www.vdi-nachrichten.com/ Der-Shop-im-Ueberblick

Täglich aktualisiert: Neuerscheinungen VDI-Schriftenreihen

BUCHSHOP

Im Buchshop von vdi-nachrichten.com finden Ingenieure und Techniker ein speziell auf sie zugeschnittenes, umfassendes Literaturangebot.

Mit der komfortablen Schnellsuche werden Sie in den VDI-Schriftenreihen und im Verzeichnis lieferbarer Bücher unter 1.000.000 Titeln garantiert fündig.

Im Buchshop stehen für Sie bereit:

VDI-Berichte und die Reihe **Kunststofftechnik**:

Berichte nationaler und internationaler technischer Fachtagungen der VDI-Fachgliederungen

Fortschritt-Berichte VDI:

Dissertationen, Habilitationen und Forschungsberichte aus sämtlichen ingenieurwissenschaftlichen Fachrichtungen

Newsletter „Neuerscheinungen":

Kostenfreie Infos zu aktuellen Titeln der VDI-Schriftenreihen bequem per E-Mail

Autoren-Service:

Umfassende Betreuung bei der Veröffentlichung Ihrer Arbeit in der Reihe Fortschritt-Berichte VDI

Buch- und Medien-Service:

Beschaffung aller am Markt verfügbaren Zeitschriften, Zeitungen, Fortsetzungsreihen, Handbücher, Technische Regelwerke, elektronische Medien und vieles mehr – einzeln oder im Abo und mit weltweitem Lieferservice

VDI nachrichten | **BUCHSHOP** **www.vdi-nachrichten.com/Der-Shop-im-Ueberblick**

Die Reihen der Fortschritt-Berichte VDI:

1 Konstruktionstechnik/Maschinenelemente
2 Fertigungstechnik
3 Verfahrenstechnik
4 Bauingenieurwesen
5 Grund- und Werkstoffe/Kunststoffe
6 Energietechnik
7 Strömungstechnik
8 Mess-, Steuerungs- und Regelungstechnik
9 Elektronik/Mikro- und Nanotechnik
10 Informatik/Kommunikation
11 Schwingungstechnik
12 Verkehrstechnik/Fahrzeugtechnik
13 Fördertechnik/Logistik
14 Landtechnik/Lebensmitteltechnik
15 Umwelttechnik
16 Technik und Wirtschaft
17 Biotechnik/Medizintechnik
18 Mechanik/Bruchmechanik
19 Wärmetechnik/Kältetechnik
20 Rechnerunterstützte Verfahren (CAD, CAM, CAE CAQ, CIM ...)
21 Elektrotechnik
22 Mensch-Maschine-Systeme
23 Technische Gebäudeausrüstung

ISBN 978-3-18-3**39609**-2